Scientific Documentation of the Multiscale Model System M-SYS

(METRAS, MITRAS, MECTM, MICTM, MESIM)

K. Heinke Schlünzen [1,2], Marita Boettcher [1,2], Björn H. Fock [1,3], Andrea Gierisch [1,4], David Grawe [2,1], Mohamed Salim [1,5,6] (edts.) [7]

MEMI Technical Report 4

2018-07-06

Meteorologisches Institut,
Centrum für Erdsystemforschung und Nachhaltigkeit, CEN
Universität Hamburg

---

1. Meteorologisches Institut, Universität Hamburg, Bundesstr. 55, D-20146 Hamburg, Germany
2. Centrum für Erdsystemforschung und Nachhaltigkeit, Universität Hamburg, Germany
3. Now: Met Office, United Kingdom.
4. Now: Finnish Meteorological Institute, Marine Research, Helsinki, Finland.
5. Faculty of Energy Engineering, Aswan University, Egypt.
6. Now: Department of Geography, Humboldt-Universität zu Berlin, Germany
7. Contact for the model: metras@uni-hamburg.de

K. Heinke Schlünzen, Meteorological Institute, Universität Hamburg, Bundesstrasse 55, 20146 Hamburg, Germany.

Table of Contents

List of Figures

Preface

This documentation is based on earlier versions and is edited by the above authors. The previous version by Schlünzen et al. (2012) was used as basis, but that version is already based on earlier versions of the model documentation with many authors contributing different parts. All contributors are gratefully acknowledged:

Bigalke, Klaus
Boettcher, Marita
Flagg, David D.
Fock, Björn H.
Gierisch, Andrea
Grawe, David
Lenz, Claus-Jürgen
Lüpkes, Christof
Niemeier, Ulrike
Reinhardt, Volker
Salim, Mohamed
Schlünzen, K. Heinke
Spensberger, Clemens
Von Salzen, Knut

1 MeMi Models in Short

The model concept of the Mesoscale and Microscale Model Family METRAS, MITRAS, MECTM and MICTM is based on the primitive equations, ensuring the conservation of mass, momentum and energy. The equations are solved three dimensional in a terrain-following coordinate system. The approximations applied ensure a wide range of model applications. The simplifications used are the anelastic assumption and the Boussinesq approximation. Additionally, the Coriolis parameter may either be constant in the model area, or depend on each grid point's latitude. There are no principal restrictions to the time and spatial variability of the synoptic fields. The use of a non-uniform grid allows a higher resolution in interesting model areas. Wind, temperature, humidity, cloud- and rain-water-content as well as concentrations are derived from prognostic equations, whereas density and pressure are calculated from diagnostic equations (Schlünzen, 1988, 1990).

The models have successfully been applied in the mesoscale-, and microscale-β-ranges; to estimate atmospheric trans-coastal fluxes of pollutants; to study transports of air pollution with passive tracers and of reactive tracers.

Sub-grid scale turbulent fluxes are parameterized by first order closure theory, using different formulations for the exchange coefficients. For the calculation of surface fluxes a blending height concept can be applied or mean parameters are calculated. Both schemes allow takeing into account sub-grid scale surface characteristics. The roughness length z_0 over water depends on the wind velocity using Charnock's formula. A Kessler type of cloud microphysics allows the formation of clouds and rain. The radiation balance in the atmosphere is calculated by a two-stream approximation that takes into account transmission and refraction by water vapor and hydrometeors. Pollutant dispersion is calculated with inclusion of dry and wet deposition processes as well as with consideration of chemical transformations. METRAS/MECTM fulfils all demands on an '"up-to-date"' mesoscale meteorology, chemistry and dispersion model.

In Chapter 2 and 3 of this model description the basic ideas of the model, including all equations and parameterizations, are described. Chapter 4 focuses on pollutant processes, including chemical transformations and deposition. In Chapter 5 the used discretization and the numerical schemes and in Chapter 6 the boundary conditions used in the model are presented. In Chapter 8 the initialization of the model is described. Appendix A includes some details on the coordinate transformation and model physics. The discrete form of the model equations is given in Appendix B. The implemented parameter values of surface characteristics and deposition modelling, a symbol table and hints for model users

including the modelling system, processing of data, details on the model use and its realization etc. are given in Schlünzen et al. (2018).

The current model description corresponds mainly to the mesoscale model METRAS Version 5.0 and the microscale model MITRAS Version 2.0, as well as the LES version of METRAS.

2 Derivation of Model Equations

This chapter contains a derivation of the basic equations and the used approximations.

2.1 Basic Equations

The basic prognostic equations of the model are given by the equation of motion (2.1), the conservation of heat, water or other materials (2.2) and the continuity equation (2.3).

They are completed by the ideal gas law (2.4) and the definition of potential temperature (*2.5*) as diagnostic equations. The basic equations within a coordinate system rotating with the earth can be written (e.g. Dutton, 1976):

$$\frac{\partial \mathbf{v}}{\partial t} + (\mathbf{v} \cdot \nabla)\mathbf{v} = -\frac{1}{\rho}\nabla p - 2[\Omega \times \mathbf{v}] - \nabla\Phi + \mathbf{F} \tag{2.1}$$

$$\frac{\partial \chi}{\partial t} + \mathbf{v} \cdot \nabla\chi = Q_\chi \tag{2.2}$$

$$\frac{\partial \rho}{\partial t} + \nabla \cdot (\rho \mathbf{v}) = 0 \tag{2.3}$$

$$v_i = \frac{R_i T}{p} \tag{2.4}$$

$$\theta = T\left(\frac{1000 \cdot 10^2 \text{ Pa}}{p}\right)^{R_0/c_p} \tag{2.5}$$

The three-dimensional velocity vector is described as v, the Nabla operator as ∇, density as ρ, pressure as p and time as t. Ω is the earth's angular velocity, Φ the geopotential and F are molecular forces, which are neglected within the model. χ stands for any scalar quantity including potential temperature θ, concentration C_j of a pollutant j or concentration of atmospheric water q_1^k, where k = 1, 2, 3 means vapor, liquid and solid phases. Sources and sinks of a scalar quantity χ are described by Q_χ, e.g. the processes of condensation and evaporation for water vapor. The specific volume v_j stands for dry air $(i = 0)$ and water $(i = 1)$ and R_i for the individual gas constant. c_p is the specific heat at constant pressure and T the real temperature.

The equations above are not solved in the Cartesian but a terrain-following coordinate system. Thus the lower boundary conditions can be calculated easier for model applications over complex terrain.

2.2 Transformation to Terrain-following Coordinates

The transformation of the model equations from a Cartesian system to a non-orthogonal coordinate system is described in Appendix A.1 in detail. Within this coordinate system

the vertical coordinate η becomes zero at the ground $z = z_s(x,y)$ and $\eta = z_t$ at the top of the model $z = z_t$:

$$\eta = z_t \frac{z - z_s(x,y)}{z_t - z_s(x,y)} \tag{2.6}$$

η -coordinates of this or a similar type are often used in mesoscale models (Pielke, 1984; Schlünzen and Schatzmann, 1984). Figure 2.1 schematically illustrates the location of coordinate surfaces η = constant for a horizontal uniform grid. Included are the basis vectors i,k of a Cartesian system X and the covariant $(\dot{q}_i)$ and contravariant (q^i) basis vectors of a terrain-following system $\dot{x}$.

The model METRAS can be used for simulations of wind, temperature and concentration fields over areas of up to 2000 x 2000 km^2. Processes limited to relatively small areas (e.g. sea-land breezes) are not parameterized but solved explicitly by the model. In some cases it is necessary to resolve the interesting areas by a fine grid. However, even with today's computer resources it is impossible to obtain high grid resolutions for the entire model area. In METRAS this problem is avoided by use of a non-uniform but horizontal orthogonal grid with minimum grid increments of about 10 m and maximum increments of about 5 km. The restrictions are caused by the numerics and parameterizations used (see below).

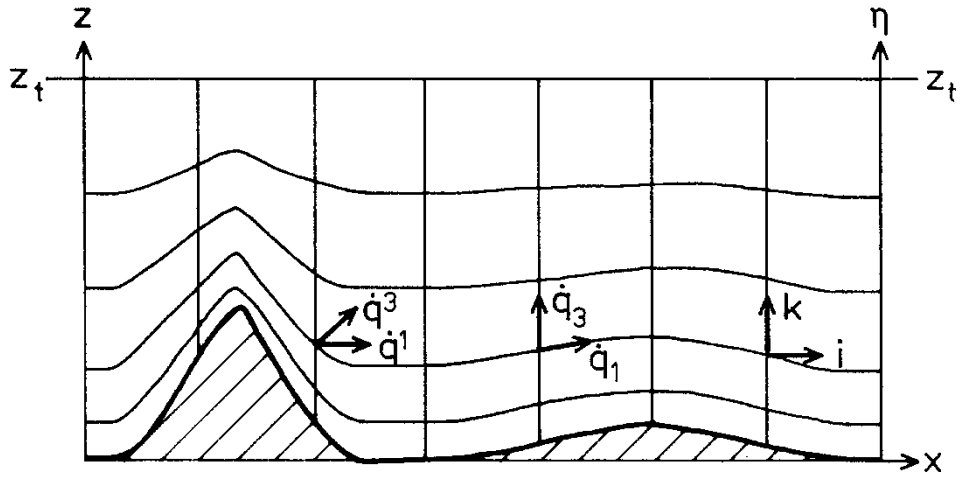

Figure 2.1: Schematic illustration of mountains, coordinate surfaces of η -coordinates, basis *vectors* i, k *of a Cartesian coordinate system* X *and* $\dot{q}_1$, $\dot{q}_3$, $\dot{q}^1$, $\dot{q}^3$ *of a terrain-following system.*

To reduce the number of grid-points, the coordinate system can be rotated against North in any desired angle (Niemeier, 1992). This rotation, as well as the varying north direction within the model domain has to be taken into account when calculating the Coriolis force (Appendix A.3).

As mentioned above, the model equations are not only transformed to a terrain-following but also from a uniform to a non-uniform grid (Appendix A.2). Figure 2.2 schematically illustrates a possible grid structure for the area of the German Bight.

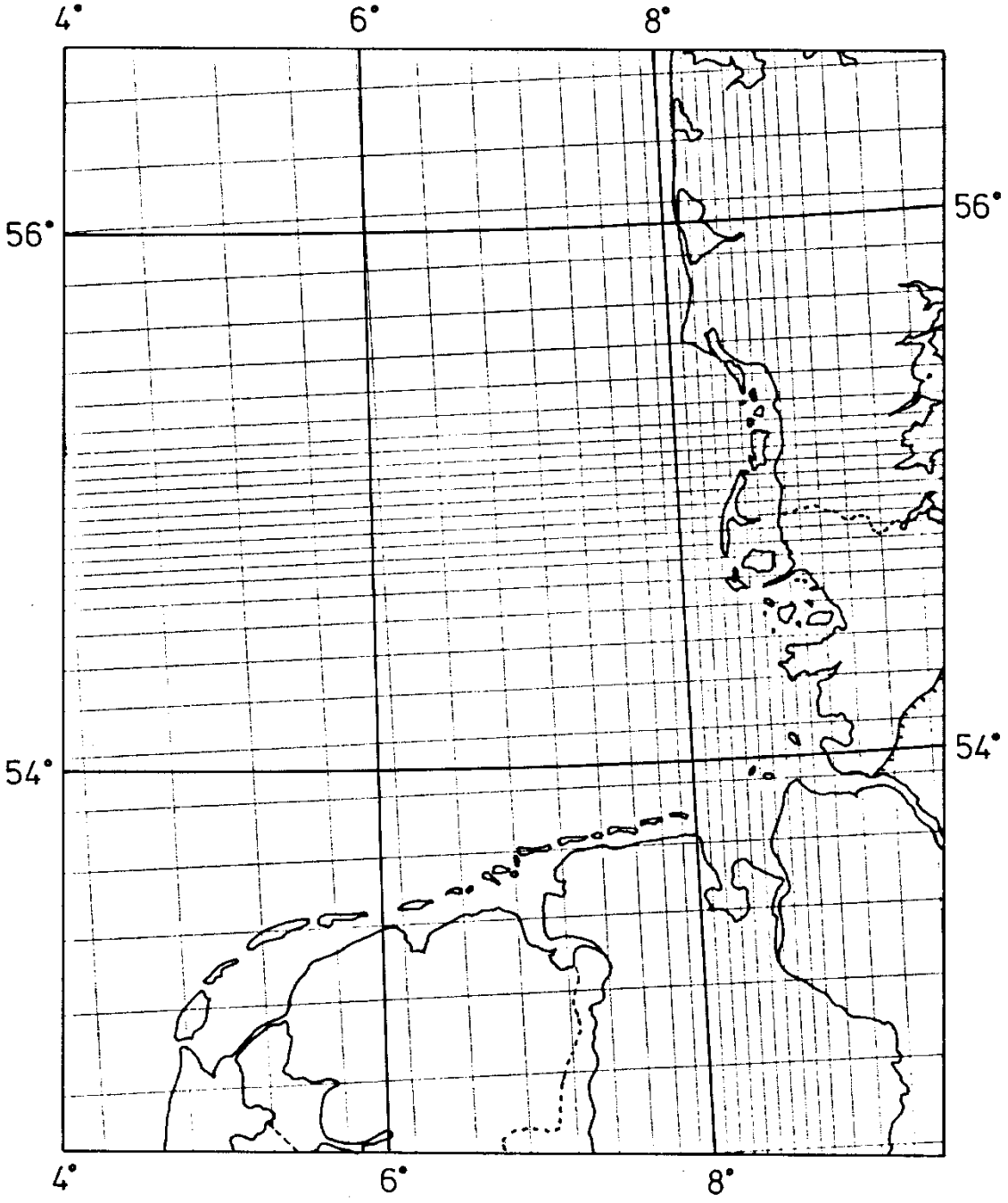

Figure 2.2: Schematic illustration of a Cartesian grid fitted to a coastline.

The prognostic model equations (2.1) - (2.3) are transformed to the described coordinate system $\dot{x}$ (Appendix A.2). The equations of momentum are given by

$$\frac{\partial \rho \alpha^* u}{\partial t} = -\frac{\partial}{\partial \dot{x}^1}\left\{u\frac{\partial \dot{x}^1}{\partial x}\rho\alpha^* u\right\} - \frac{\partial}{\partial \dot{x}^2}\left\{v\frac{\partial \dot{x}^2}{\partial y}\rho\ \alpha^* u\right\} - \frac{\partial}{\partial \dot{x}^3}\left\{\dot{u}^3\rho_o\alpha^* u\right\}$$

$$-\alpha^*\frac{\partial \dot{x}^1}{\partial x}\frac{\partial p}{\partial \dot{x}^1} - \alpha^*\frac{\partial \dot{x}^3}{\partial x}\frac{\partial p}{\partial \dot{x}^3} + f\rho\alpha^* v - f' d'\rho\alpha^*\omega$$

$$\frac{\partial \rho \alpha^* v}{\partial t} = -\frac{\partial}{\partial \dot{x}^1}\left\{u\frac{\partial \dot{x}^1}{\partial x}\rho\alpha^* v\right\} - \frac{\partial}{\partial \dot{x}^2}\left\{v\frac{\partial \dot{x}^2}{\partial y}\rho\alpha^* v\right\} - \frac{\partial}{\partial \dot{x}^3}\left\{\dot{u}^3\rho_o\alpha^* v\right\} \tag{2.7}$$

$$-\alpha^*\frac{\partial \dot{x}^2}{\partial y}\frac{\partial p}{\partial \dot{x}^2} - \alpha^*\frac{\partial \dot{x}^3}{\partial y}\frac{\partial p}{\partial \dot{x}^3} - f\rho\alpha^* u + f' d'\rho\alpha^*\omega$$

$$\frac{\partial \rho \alpha^* \omega}{\partial t} = -\frac{\partial}{\partial \dot{x}^1}\left\{u\frac{\partial \dot{x}^1}{\partial x}\rho\alpha^*\omega\right\} - \frac{\partial}{\partial \dot{x}^2}\left\{v\frac{\partial \dot{x}^2}{\partial y}\rho\alpha^*\omega\right\} - \frac{\partial}{\partial \dot{x}^3}\left\{\dot{u}^3\rho\alpha^*\omega\right\}$$

$$-\alpha^*\frac{\partial \dot{x}^3}{\partial z}\frac{\partial p}{\partial \dot{x}^3} + f'\rho\alpha^*(ud' - vd) - \rho\alpha^* g$$

The components of the wind vector **v** in Cartesian coordinates are named u, v, w corresponding to the $x-, y-, z-$direction. The variables $d = \sin\xi$ and $d' = \cos\xi$ characterize the influence of a rotation of the coordinate system by an angle ξ against North. In the non-rotated case $(\xi = 0)$ the components of the wind vector characterize the west-east, south-north and vertical winds. α^* denotes the grid volume. $\dot{x}^1, \dot{x}^2, \dot{x}^3$ and x, y, z are the coordinates of the used coordinate system $\dot{x}$ and the Cartesian system X, respectively. The Coriolis parameters $f = 2\Omega\sin\varphi$ and $f' = 2\Omega\cos\varphi$ are calculated for the geographic latitude φ of either a reference point or the local grid point, and g is the acceleration of gravity.

The surface-boundary normal wind component $\dot{u}^3$ can be calculated from u, v, w by:

$$\dot{u}^3 = u\frac{\partial \dot{x}^3}{\partial x} + v\frac{\partial \dot{x}^3}{\partial y} + w\frac{\partial \dot{x}^3}{\partial z} \tag{2.8}$$

The transformed continuity equation is given by:

$$\frac{\partial \rho\alpha^*}{\partial t} + \frac{\partial}{\partial \dot{x}^1}\left\{\rho\alpha^* u\frac{\partial \dot{x}^1}{\partial x}\right\} + \frac{\partial}{\partial \dot{x}^2}\left\{\rho\alpha^* v\frac{\partial \dot{x}^2}{\partial y}\right\} + \frac{\partial}{\partial \dot{x}^3}\left\{\rho\alpha^*\dot{u}^3\right\} = 0 \tag{2.9}$$

The conservation of a scalar quantity χ can be written as:

$$\frac{\partial \rho \alpha^* \chi}{\partial t} = -\frac{\partial}{\partial \dot{x}^1}\left\{u \frac{\partial \dot{x}^1}{\partial x} \rho \alpha^* \chi\right\} - \frac{\partial}{\partial \dot{x}^2}\left\{v \frac{\partial \dot{x}^2}{\partial y} \rho \alpha^* \chi\right\} - \frac{\partial}{\partial \dot{x}^3}\left\{(u \frac{\partial \dot{x}^3}{\partial x} + v \frac{\partial \dot{x}^3}{\partial y} + w \frac{\partial \dot{x}^3}{\partial z}) \rho \alpha^* \chi\right\} - Q_\chi \tag{2.10}$$

where Q_χ is the production term of χ.

2.3 Filtering the Basic Equations and Introduction of Basic State

The system of equations (2.7) - (2.10) can be solved directly, as long as the spatial derivatives $\partial\psi/\partial\dot{x}^i$ of a variable ψ can be assumed as being constant over a spatial scale $\delta\dot{x}^i$ and a time scale δt. In the atmosphere this assumption is valid for spatial scales of about 1 cm and time scales of about 1 sec (Pielke, 1984). If one tries to solve the system (2.7) - (2.10) for typical mesoscale or microscale phenomena of a horizontal scale of about 100 km or 1 km and a vertical extension of about 10 km or at least 1 km, it would be necessary to calculate solutions at about 10^{19}-10^{20} grid points. Since this exceeds the capacity of existing computers by far, the equations have to be averaged (filtered), i.e. they are integrated in time and space.

Each dependent variable ψ is decomposed into an average $\overline{\psi}$ and a deviation ψ' from the average. $\overline{\psi}$ represents the average of ψ over the finite time increment Δt and a surrounding volume $\Delta x \cdot \Delta y \cdot \Delta z$ (Pielke, 1984):

$$\overline{\psi} := \frac{\int_t^{t+\Delta t}\int_{z_a}^{z_a+\Delta z}\int_{y_a}^{y_a+\Delta y}\int_{x_a}^{x_a+\Delta x} \psi \, dx \, dy \, dz \, dt}{\Delta t \cdot \Delta x \cdot \Delta y \cdot \Delta z} \tag{2.11}$$

Replacing ψ by $\overline{\psi} + \psi'$ and integrating the model equations over the grid volume $\Delta x \cdot \Delta y \cdot \Delta z$ and time interval Δt corresponding to (2.11), the filtered model equations result.

The averaging is done by assuming that $\overline{\overline{\psi}} = \overline{\psi}$, $\overline{\psi'} = 0$, $\overline{\partial\psi/\partial t} = \partial\overline{\psi}/\partial t$, $\overline{\partial\psi/\partial\dot{x}^i} = \partial\overline{\psi}/\partial\dot{x}^i$ etc. Additionally, for the metric tensor and the Christoffel symbol $\dot{g}^{ij} = \overline{\dot{g}^{ij}}$ and $\dot{\Gamma}^i_{jk} = \overline{\dot{\Gamma}^i_{jk}}$ is assumed. Because of these assumptions the surface heights have to be considered as linear within the averaging interval. Microscale pressure and density variations are neglected due to the Markovian hypothesis (Rotta, 1972). In other words, it is assumed that small turbulent pressure fluctuations p' cause only small density variations ρ'.

In the filtered equations the averages $\overline{\psi}$ of temperature, humidity, concentrations, pressure and density are further decomposed into a deviation part $\tilde{\psi}$ and a large-scale part ψ_o. The large-scale part represents the basic state in an area $\Delta x \cdot \Delta y$ larger than the phenomena of interest. In the MeMi models always the model area is used here, thus ψ_o

represents a domain average value which is only height dependent and not time dependent.

$$\psi_0 = \frac{\int_{y_a}^{y_a+\Delta y}\int_{x_a}^{x_a+\Delta x} \overline{\psi}\, dx\, dy}{\Delta x \cdot \Delta y} \tag{2.12}$$

For numerical reasons the deviation pressure $\tilde{p}$ is additionally decomposed into p_1 and $p_2 = \tilde{p} - p_1$. Their definition and calculation is described in Sections 2.4 and 2.5. In summary the meteorological variables are composed by:

$$\begin{aligned}
u &= \overline{u} + u' && (a)\\
v &= \overline{v} + v' && (b)\\
w &= \overline{w} + w' && (c)\\
\rho &= \rho_0 + \tilde{\rho} \quad (assumption: \rho' << \tilde{\rho}) && (d)\\
p &= p_0 + p_1 + p_2 \quad (assumption: p' << \tilde{p}) && (e)\\
\chi &= \chi_o + \tilde{\chi} + \chi' && (f)
\end{aligned} \tag{2.13}$$

In the next section the approximations applied to the model equations are described.

2.4 Approximations

The model may be applied to large areas with higher resolution in subareas of special interest. To calculate pollutant concentrations with respect to the existing meteorological conditions, the model has to take into account the phenomena of the so-called mesoscales γ and β (METRAS) or of the microscale (MITRAS). The chosen approximations should not restrict the applicability of the model within these scales. The scales typically simulated by the models are sketched in Figure 2.3. The hatched areas in Figure 2.4 illustrate the scales of validity of approximations typically applied in atmospheric models. They are based on scale analysis of the individual terms in the equation of motion and continuity equation, published by Businger (1982), Martin and Pielke (1983), Schlünzen and Schatzmann (1984) and Wippermann (1981).

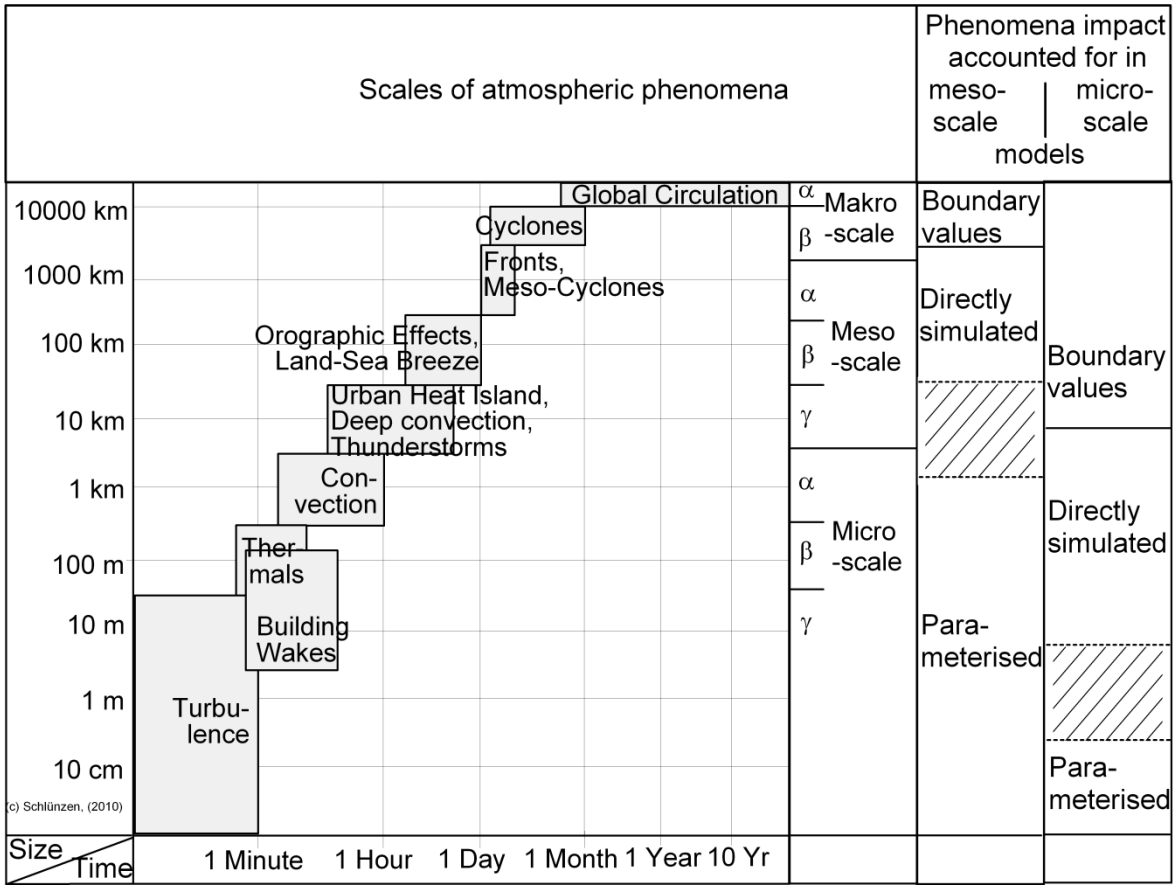

Figure 2.3: Scales of atmospheric phenomena (left) and phenomena simulated, parameterised or to be prescribed by mesoscale and microscale models (from Schlünzen et al., 2011).

The hydrostatic approximation $(\partial p/\partial z = -g\rho)$ can be applied to phenomena of more than 10 km characteristic horizontal scale L_s. The anelastic approximation

$$\nabla \cdot (\rho_o v) = 0 \tag{2.14}$$

is valid within the entire mesoscale and microscale, while the incompressibility assumption can only be applied to horizontal scales smaler than 20 km. The validity of the geostrophic approximation $(v = V_g)$ can be assumed only in the macroscale. For phenomena with horizontal scales up to L_s = 1500 km it is allowed to take the Coriolis parameter f constant. For smaller scales (up to about 20 km) the Coriolis force can be totally neglected. This is, however, not true in the vertical, where Coriolis force effects need to be considered above the surface layer.

	Scale L_s (km)	Micro <2.5	Meso γ 2.5	Meso β 25	Meso α 250	Macro … >2500
	Approximation					
	vertical wind eq. / **continuity equation**					
I	$\frac{\partial \bar{p}}{\partial z} = -g\bar{\rho}$ / $\nabla \cdot \mathbf{v} = 0$					
II	/ $\nabla \cdot \rho\mathbf{v} = 0$					
III						
IV	/ $\nabla \cdot \mathbf{v} = 0$					
V	/ $\nabla \cdot \rho\mathbf{v} = 0$					
VI						

Figure 2.4: Validity range (grey areas) of approximations (Schlünzen et al., 2010)

Due to the described validity of approximations and the intended application of METRAS to maximum areas of about 2000 km x 2000 km, and of MITRAS with horizontal grid increments of about meters, the models use the anelastic approximation. The Coriolis parameter may be held constant in smaller domains (MITRAS, small mesoscale domains) but can also vary with each grid point's latitude (large mesoscale domains). The hydrostatic and geostrophic approximations as well as the incompressibility assumption are not valid for this range of application.

The anelastic approximated continuity equation is given in our coordinate system as:

$$\frac{\partial}{\partial \dot{x}^1}\left\{\rho_o \alpha^* \bar{u} \frac{\partial \dot{x}^1}{\partial x}\right\} + \frac{\partial}{\partial \dot{x}^2}\left\{\rho_o \alpha^* \bar{v} \frac{\partial \dot{x}^2}{\partial y}\right\} + \frac{\partial}{\partial \dot{x}^3}\left\{\rho_o \alpha^* \overline{\dot{u}^3}\right\} = 0 \tag{2.15}$$

Assuming the validity of the Boussinesq approximation; deviations from the density ρ_0 are neglected except in the buoyancy term. Elsewhere the density is replaced by the basic state density.

$$\rho = \rho_0\left(1 + \frac{\tilde{\rho}}{\rho_0}\right) \cong \rho_o \tag{2.16}$$

Corresponding to equation (2.13) the pressure is decomposed into a large-scale and two deviation parts. The large-scale basic state pressure p_0 is assumed to fulfil the hydrostatic approximation:

$$\frac{\partial p_o}{\partial \dot{x}^3} = -g\rho_o \frac{\partial z}{\partial \dot{x}^3} \tag{2.17}$$

The large-scale basic pressure gradients are shortened in the equations by using the geostrophic approximation. This improves the accuracy and reduced the computing time of the model. With respect to the used coordinate system $\dot{x}$ the horizontal basic state pressure gradients are prescribed as:

$$U_g := -\frac{1}{\rho_o f}\left\{\frac{\partial \dot{x}^2}{\partial y}\frac{\partial p_o}{\partial \dot{x}^2}+\frac{\partial \dot{x}^3}{\partial y}\frac{\partial p_o}{\partial \dot{x}^3}\right\} \quad \text{(a)}$$

$$V_g := +\frac{1}{\rho_o f}\left\{\frac{\partial \dot{x}^1}{\partial x}\frac{\partial p_o}{\partial \dot{x}^1}+\frac{\partial \dot{x}^3}{\partial x}\frac{\partial p_o}{\partial \dot{x}^3}\right\} \quad \text{(b)} \qquad (2.18)$$

The pressure p_1 is calculated by assuming p_1 is in hydrostatic balance with the average density deviation:

$$\frac{\partial p_1}{\partial \dot{x}^3} := -g\rho_o\frac{\tilde{\rho}}{\rho_0}\frac{\partial z}{\partial \dot{x}^3} \qquad (2.19)$$

Thus, p_1 can be interpreted as the hydrostatic component of the pressure deviation $\tilde{p}$. The density deviation $\tilde{\rho}$ for a humid atmosphere can be derived from the linearized gas law (2.20). It depends on the potential temperature deviation $\tilde{q}_1^1 = q_1^1 - q_{o\,1}^{\;1}$, and liquid water deviations $\tilde{q}_1^2 = \bar{q}_1^2 - q_{o\,1}^{\;2}$ (Schröder, 1987):

$$\frac{\tilde{\rho}}{\rho_o} = -\frac{\tilde{\theta}}{\theta_o}+\frac{c_v}{c_p}\frac{p_1+p_2}{p_o}-\left(\frac{R_1^1}{R_o}-1\right)\cdot\tilde{q}_1^1+\tilde{q}_1^2 \qquad (2.20)$$

c_v and c_p denote the specific heat of dry air at constant volume and at constant pressure, respectively. The large-scale potential temperature θ_o is calculated from

$$\theta_o = T_o\left(\frac{100000}{p_o}\right)^{R/c_p} \qquad (2.21)$$

The temperature deviation $\tilde{\theta}$ is calculated from the temperature deviation $\tilde{T}$ and includes influences of the pressure deviation $\tilde{p}$:

$$\tilde{\theta} = \tilde{T}\left(\frac{100000}{p_o+p_1+p_2}\right)^{R/c_p} \qquad (2.22)$$

R_1^1 and R_o are the gas constants of water vapour and dry air.

Note that in a neutral case, $\tilde{\rho}$ is zero since there are no temperature deviations and from (2.19) it can be derived that p_1 remains constant. Furthermore, be aware that the formulation used makes the model results dependent on the chosen basic state. If this is not somewhat representative for the situation simulated, the density deviation abs($\tilde{\rho}$) might be very large and thus the Boussinesq approximation no longer fulfilled. If this is the case it might be worthwhile to recalculate the basic state from horizontally averaged basic profiles.

2.5 Filtered Model Equations

Using the approximations mentioned in the previous section and the transformation rules of Appendices A.1 and A.2, the filtered model equations read as follows.

2.5.1 Momentum Equations

$$\frac{\partial \rho_o \alpha^* \bar{u}}{\partial t} = -\frac{\partial}{\partial \dot{x}^1}\left\{\bar{u}\frac{\partial \dot{x}^1}{\partial x}\rho_o\alpha^*\bar{u}\right\} - \frac{\partial}{\partial \dot{x}^2}\left\{\bar{v}\frac{\partial \dot{x}^2}{\partial y}\rho_o\alpha^*\bar{u}\right\} - \frac{\partial}{\partial \dot{x}^3}\left\{\overline{\dot{u}^3}\rho_o\alpha^*\bar{u}\right\}$$

$$-\alpha^*\frac{\partial \dot{x}^1}{\partial x}\left\{\frac{\partial p_1}{\partial \dot{x}^1} + \frac{\partial p_2}{\partial \dot{x}^1}\right\} - \alpha^*\frac{\partial \dot{x}^3}{\partial x}\frac{\partial p_2}{\partial \dot{x}^3} + \tilde{\rho}\alpha^* g\frac{\partial \dot{x}^3}{\partial x}\frac{\partial z}{\partial \dot{x}^3}$$

$$+ f\left\{\rho_o\alpha^*\bar{v} - \rho_o\alpha^* V_g\right\} - f'd'\rho_o\alpha^*\bar{\omega} - \bar{F}_1 \qquad \text{(a)}$$

$$\frac{\partial \rho_o \alpha^* \bar{v}}{\partial t} = -\frac{\partial}{\partial \dot{x}^1}\left\{\bar{u}\frac{\partial \dot{x}^1}{\partial x}\rho_o\alpha^*\bar{v}\right\} - \frac{\partial}{\partial \dot{x}^2}\left\{\bar{v}\frac{\partial \dot{x}^2}{\partial y}\rho_o\alpha^*\bar{v}\right\} - \frac{\partial}{\partial \dot{x}^3}\left\{\overline{\dot{u}^3}\rho_o\alpha^*\bar{v}\right\}$$

$$-\alpha^*\frac{\partial \dot{x}^2}{\partial y}\left\{\frac{\partial p_1}{\partial \dot{x}^2} + \frac{\partial p_2}{\partial \dot{x}^2}\right\} - \alpha^*\frac{\partial \dot{x}^3}{\partial y}\frac{\partial p_2}{\partial \dot{x}^3} + \tilde{\rho}\alpha^* g\frac{\partial \dot{x}^3}{\partial y}\frac{\partial z}{\partial \dot{x}^3} \qquad (2.23)$$

$$-f\left\{\rho_o\alpha^*\bar{u} - \rho_o\alpha^* U_g\right\} + f'\,d\,\rho_o\alpha^*\bar{\omega} - \bar{F}_2 \qquad \text{(b)}$$

$$\frac{\partial \rho_o \alpha^* \bar{w}}{\partial t} = -\frac{\partial}{\partial \dot{x}^1}\left\{\bar{u}\frac{\partial \dot{x}^1}{\partial x}\rho_o\alpha^*\bar{w}\right\} - \frac{\partial}{\partial \dot{x}^2}\left\{\bar{v}\frac{\partial \dot{x}^2}{\partial y}\rho_o\alpha^*\bar{w}\right\} - \frac{\partial}{\partial \dot{x}^3}\left\{\overline{\dot{u}^3}\rho_o\alpha^*\bar{w}\right\}$$

$$-\alpha^*\frac{\partial \dot{x}^3}{\partial z}\frac{\partial p_2}{\partial \dot{x}^3} + f'\rho_o\alpha^*\left(\bar{u}d' - \bar{v}d\right) - \bar{F}_3 \qquad \text{(c)}$$

The terms $\bar{F}_1$, $\bar{F}_2$, $\bar{F}_3$ are obtained from averaging the equations and describe the sub-grid scale turbulent momentum fluxes. In Chapter 3 their parameterization is given for the Reynolds averaged and the Large-Eddy simulation versions of the MeMi models. The pressure p_1 is computed from (2.19), the density $\tilde{\rho}$ from (2.20).

2.5.2 Dynamic Pressure

An equation for the *dynamic* pressure p_2 can be derived which is based on the following ideas:

- The anelastic approximation (2.15) has to be fulfilled at every time step.

- The complete equations of motion (2.23) can be integrated forward in time by using the pressure values at the previous time step. This results in so named preliminary velocities $\hat{u}, \hat{v}, \hat{w},$ which do not fulfil the anelastic approximation (2.15). The numerical schemes as described in Chapter 5 need to be used for this integration.
- The final velocities $\bar{u}^{t+\Delta t}, \bar{v}^{t+\Delta t}, \overline{\dot{u}^3}^{t+\Delta t}$ at time step n+1 can then be described dependent on the preliminary velocities and the temoral changes in the pressure gradient of $\hat{p}_2$. Here it is used that $p_2^{t+\Delta t} = p_2^t + \hat{p}_2$

$$
\begin{aligned}
\bar{u}^{t+\Delta t} &= \hat{u} - \frac{1}{\rho_o}\left[\frac{\partial \dot{x}^1}{\partial x}\frac{\partial \hat{p}_2}{\partial \dot{x}^1} + \frac{\partial \dot{x}^3}{\partial x}\frac{\partial \hat{p}_2}{\partial \dot{x}^3}\right]^{t+\Delta t}\cdot \Delta t \qquad \text{(a)}\\
\bar{v}^{t+\Delta t} &= \hat{v} - \frac{1}{\rho_o}\left[\frac{\partial \dot{x}^2}{\partial y}\frac{\partial \hat{p}_2}{\partial \dot{x}^2} + \frac{\partial \dot{x}^3}{\partial y}\frac{\partial \hat{p}_2}{\partial \dot{x}^3}\right]^{t+\Delta t}\cdot \Delta t \qquad \text{(b)}\\
\overline{\dot{u}^3}^{t+\Delta t} &= \hat{u}^3 - \frac{1}{\rho_o}\left[\frac{\partial \dot{x}^1}{\partial x}\frac{\partial \dot{x}^3}{\partial x}\frac{\partial \hat{p}_2}{\partial \dot{x}^1} + \frac{\partial \dot{x}^2}{\partial y}\frac{\partial \dot{x}^3}{\partial y}\frac{\partial \hat{p}_2}{\partial \dot{x}^2}\right.\\
&\quad \left. + \left(\left(\frac{\partial \dot{x}^3}{\partial x}\right)^2 + \left(\frac{\partial \dot{x}^3}{\partial y}\right)^2 + \left(\frac{\partial \dot{x}^3}{\partial z}\right)^2\right)\frac{\partial \hat{p}_2}{\partial \dot{x}^3}\right]^{t+\Delta t}\cdot \Delta t \qquad \text{(c)}
\end{aligned}
\tag{2.24}
$$

Using equation (2.24) in the anelastic approximation (2.15) results in a diagnostic elliptic equation for the pressure deviation $\hat{p}_2$ dependent on the preliminary velocities $\hat{u}, \hat{v}, \hat{u}^3$, where $\hat{p}_2$ denotes the pressure change within the time step Δt:

$$
\begin{aligned}
\nabla \alpha^* \nabla \hat{p}_2 &= \frac{\partial}{\partial \dot{x}^1}\left\{\alpha^*\left(\frac{\partial \dot{x}^1}{\partial x}\right)^2\frac{\partial \hat{p}_2}{\partial \dot{x}^1} + \alpha^*\frac{\partial \dot{x}^1}{\partial x}\frac{\partial \dot{x}^3}{\partial x}\frac{\partial \hat{p}_2}{\partial \dot{x}^3}\right\}\\
&\quad + \frac{\partial}{\partial \dot{x}^2}\left\{\alpha^*\left(\frac{\partial \dot{x}^2}{\partial y}\right)^2\frac{\partial \hat{p}_2}{\partial \dot{x}^2} + \alpha^*\frac{\partial \dot{x}^2}{\partial y}\frac{\partial \dot{x}^3}{\partial y}\frac{\partial \hat{p}_2}{\partial \dot{x}^3}\right\}\\
&\quad + \frac{\partial}{\partial \dot{x}^3}\left\{\alpha^*\left(\left(\frac{\partial \dot{x}^3}{\partial x}\right)^2 + \left(\frac{\partial \dot{x}^3}{\partial y}\right)^2 + \left(\frac{\partial \dot{x}^3}{\partial z}\right)^2\right)\frac{\partial \hat{p}_2}{\partial \dot{x}^3}\right.\\
&\quad \left. + \alpha^*\left(\frac{\partial \dot{x}^1}{\partial x}\frac{\partial \dot{x}^2}{\partial x}\frac{\partial \hat{p}_2}{\partial \dot{x}^1} + \frac{\partial \dot{x}^2}{\partial y}\frac{\partial \dot{x}^3}{\partial y}\frac{\partial \hat{p}_2}{\partial \dot{x}^2}\right)\right\}\\
&= \frac{1}{\Delta t}\left[\frac{\partial}{\partial \dot{x}^1}\left\{\rho_0 \alpha^* \hat{u}\frac{\partial \dot{x}^1}{\partial x}\right\} + \frac{\partial}{\partial \dot{x}^2}\left\{\rho_0 \alpha^* \hat{v}\frac{\partial \dot{x}^2}{\partial y}\right\} + \frac{\partial}{\partial \dot{x}^3}\left\{\rho_0 \alpha^* \hat{u}^3\right\}\right]\\
&= \frac{1}{\Delta t}\nabla\left(\rho_o \alpha^* \hat{\mathbf{v}}\right)
\end{aligned}
\tag{2.25}
$$

Following equation (2.8), the vertical velocity $\overline{w}$ can be calculated from $\overline{u},\overline{v},\overline{u}^3$:

$$\overline{w} = \left(\overline{u}^3 - \overline{u}\frac{\partial \dot{x}^3}{\partial x} - \overline{v}\frac{\partial \dot{x}^3}{\partial y} \right) \Bigg/ \frac{\partial \dot{x}^3}{\partial z} \tag{2.26}$$

Since p_2 can be different from zero even in a dry atmosphere without temperature deviations, it is often called the *dynamic* pressure.

2.5.3 Prognostic equations for scalar quantities

In the coordinate system $\dot{x}$ the prognostic equation of the potential temperature $\overline{\theta}$ can be written as:

$$\begin{aligned} \frac{\partial \rho_o \alpha^* \overline{\theta}}{\partial t} = & -\frac{\partial}{\partial \dot{x}^1}\left\{ \overline{u}\frac{\partial \dot{x}^1}{\partial x}\rho_o \alpha^* \widetilde{\theta} \right\} - \frac{\partial}{\partial \dot{x}^2}\left\{ \overline{v}\frac{\partial \dot{x}^2}{\partial y}\rho_o \alpha^* \widetilde{\theta} \right\} \\ & - \frac{\partial}{\partial \dot{x}^3}\left\{ \left(\overline{u}\frac{\partial \dot{x}^3}{\partial x} + \overline{v}\frac{\partial \dot{x}^3}{\partial y} + \overline{\omega}\frac{\partial \dot{x}^3}{\partial z} \right) \rho_o \alpha^* \overline{\theta} \right\} \\ & - \overline{F}_{\overline{\theta}} + \rho_o \alpha^* \overline{Q}_{\overline{\theta}} \end{aligned} \tag{2.27}$$

Simulations of a humid atmosphere require additional prognostic equations for water in the different phases. The balance equation of specific humidity $\widetilde{q}_1^1$ can be written as:

$$\begin{aligned} \frac{\partial \rho_o \alpha^* \overline{q}_1^1}{\partial t} = & -\frac{\partial}{\partial \dot{x}^1}\left\{ \overline{u}\frac{\partial \dot{x}^1}{\partial x}\rho_o \alpha^* \overline{q}_1^1 \right\} - \frac{\partial}{\partial \dot{x}^2}\left\{ \overline{v}\frac{\partial \dot{x}^2}{\partial y}\rho_o \alpha^* \overline{q}_1^1 \right\} \\ & - \frac{\partial}{\partial \dot{x}^3}\left\{ \left(\overline{u}\frac{\partial \dot{x}^3}{\partial x} + \overline{v}\frac{\partial \dot{x}^3}{\partial y} + \overline{\omega}\frac{\partial \dot{x}^3}{\partial z} \right) \rho_o \alpha^* \overline{q}_1^1 \right\} \\ & - \overline{F}_{\overline{q}_1^1} + \rho_o \alpha^* \overline{Q}_{\overline{q}_1^1} \end{aligned} \tag{2.28}$$

Replacing $\overline{q}_1^1$ by $\overline{q}_1^2$ yields the balance equation of liquid water

$$\begin{aligned} \frac{\partial \rho_o \alpha^* \overline{q}_1^2}{\partial t} = & -\frac{\partial}{\partial \dot{x}^1}\left\{ \overline{u}\frac{\partial \dot{x}^1}{\partial x}\rho_o \alpha^* \overline{q}_1^2 \right\} - \frac{\partial}{\partial \dot{x}^2}\left\{ \overline{v}\frac{\partial \dot{x}^2}{\partial y}\rho_o \alpha^* \overline{q}_1^2 \right\} \\ & - \frac{\partial}{\partial \dot{x}^3}\left\{ \left(\overline{u}\frac{\partial \dot{x}^3}{\partial x} + \overline{v}\frac{\partial \dot{x}^3}{\partial y} + \overline{\omega}\frac{\partial \dot{x}^3}{\partial z} \right) \rho_o \alpha^* \overline{q}_1^2 \right\} \\ & - \overline{F}_{\overline{q}_1^2} + \rho_o \alpha^* \overline{Q}_{\overline{q}_1^2} \end{aligned} \tag{2.29}$$

where $\overline{q}_1^2$ can be cloud water as well as rain water (see Section 3.4 for details on the parameterization of cloud microphysics).

An analogous equation describes the balance of pollutant concentrations $\overline{c}_j$:

$$\frac{\partial \rho_o \alpha^* \overline{C}_j}{\partial t} = -\frac{\partial}{\partial \dot{x}^1}\left\{\overline{u}\,\frac{\partial \dot{x}^1}{\partial x}\rho_o \alpha^* \overline{C}_j\right\} - \frac{\partial}{\partial \dot{x}^2}\left\{\overline{v}\,\frac{\partial \dot{x}^2}{\partial y}\rho_o \alpha^* \overline{C}_j\right\}$$
$$-\frac{\partial}{\partial \dot{x}^3}\left\{\left(\overline{u}\,\frac{\partial \dot{x}^3}{\partial x} + \overline{v}\,\frac{\partial \dot{x}^3}{\partial y} + \overline{\omega}\,\frac{\partial \dot{x}^3}{\partial z}\right)\rho_o \alpha^* \overline{C}_j\right\} \qquad (2.30)$$
$$-\overline{F}_{\overline{C}_j} + \rho_o \alpha^* \overline{Q}_{\overline{C}_j}$$

The terms $\overline{Q}_\chi$ contain the specific sources and sinks for temperature, humidity, liquid water and pollutant concentration as well as their large-scale tendencies compiled in (2.23)-(2.25). The turbulent flux divergences of $\overline{\chi}$ are summarized in the terms $\overline{F}_\chi$ (Chapter 3). In METRAS/MITRAS the sub-grid scale fluxes that include χ' are derived from the filtered values $\overline{\chi}$.

3 Parameterization of sub-grid scale processes

In this chapter the parameterization of meteorological sub-grid scale processes including turbulent fluxes, cloud microphysics and radiation is described. Parameterizations applied only to pollutants are described in Chapter 4.

3.1 Sub-grid scale fluxes of momentum

Most sub-grid scale turbulent transport terms in the model equations are parameterized by a first order closures. Additionally closures based on one or two additional transport equations so called 1.5 order closures are available. It is possible to choose between different approaches to determine the exchange coefficients above the Prandtl-layer.

The diffusion terms $\overline{F}_i$ in the prognostic equations for momentum can be written as:

$$\begin{aligned}
\overline{F}_1 &= \frac{\partial}{\partial \dot{x}^1}\left\{\rho_0 \alpha^* \overline{u'u'}\frac{\partial \dot{x}^1}{\partial x}\right\} + \frac{\partial}{\partial \dot{x}^2}\left\{\rho_0 \alpha^* \overline{v'u'}\frac{\partial \dot{x}^2}{\partial y}\right\} \\
&\quad + \frac{\partial}{\partial \dot{x}^3}\left\{\rho_0 \alpha^* \overline{u'u'}\frac{\partial \dot{x}^3}{\partial x} + \rho_0 \alpha^* \overline{v'u'}\frac{\partial \dot{x}^3}{\partial y} + \rho_0 \alpha^* \overline{w'u'}\frac{\partial \dot{x}^3}{\partial z}\right\} \qquad (a) \\
\overline{F}_2 &= \frac{\partial}{\partial \dot{x}^1}\left\{\rho_0 \alpha^* \overline{u'v'}\frac{\partial \dot{x}^1}{\partial x}\right\} + \frac{\partial}{\partial \dot{x}^2}\left\{\rho_0 \alpha^* \overline{v'v'}\frac{\partial \dot{x}^2}{\partial y}\right\} \\
&\quad + \frac{\partial}{\partial \dot{x}^3}\left\{\rho_0 \alpha^* \overline{u'v'}\frac{\partial \dot{x}^3}{\partial x} + \rho_0 \alpha^* \overline{v'v'}\frac{\partial \dot{x}^3}{\partial y} + \rho_0 \alpha^* \overline{w'v'}\frac{\partial \dot{x}^3}{\partial z}\right\} \qquad (b) \\
\overline{F}_3 &= \frac{\partial}{\partial \dot{x}^1}\left\{\rho_0 \alpha^* \overline{u'w'}\frac{\partial \dot{x}^1}{\partial x}\right\} + \frac{\partial}{\partial \dot{x}^2}\left\{\rho_0 \alpha^* \overline{v'w'}\frac{\partial \dot{x}^2}{\partial y}\right\} \\
&\quad + \frac{\partial}{\partial \dot{x}^3}\left\{\rho_0 \alpha^* \overline{u'w'}\frac{\partial \dot{x}^3}{\partial x} + \rho_0 \alpha^* \overline{v'w'}\frac{\partial \dot{x}^3}{\partial y} + \rho_0 \alpha^* \overline{w'w'}\frac{\partial \dot{x}^3}{\partial z}\right\} \qquad (c)
\end{aligned} \qquad (3.1)$$

The sub-grid scale turbulent fluxes, which include u', v', w', can be obtained either by formulating prognostic equations (second order closure) or by deducing them by using the filtered velocities. In order to minimize the integration time the turbulent fluxes in METRAS are derived from a first order closure (e.g. Etling, 1987, Detering, 1985):

$$\tau_{ij} = -\rho_0 \overline{u'_i u'_j} = \rho_0 K_{ij}\left\{\frac{\partial \bar{u}_i}{\partial x^j} + \frac{\partial \bar{u}_j}{\partial x^i}\right\} \qquad (3.2)$$

It should be noted that the reduction of the diagonal fluxes due to pressure (turbulent kinetic energy term) is neglected in METRAS at present. The wind components u, v, w in

the Cartesian coordinate system X are indicated by u_i. In the terrain-following coordinate system $\dot{x}$, equation 3.2 can be written as

$$\tau_{ij} = \rho_0 K_{ij} \left\{ \frac{\partial \overline{u}_i}{\partial \dot{x}^k} \frac{\partial \dot{x}^k}{\partial x^j} + \frac{\partial \overline{u}_j}{\partial \dot{x}^k} \frac{\partial \dot{x}^k}{\partial x^i} \right\} \tag{3.3}$$

Here the Einstein summation is used for $k\,(k=1,2,3)$, but not for i and j. It can be assumed that the fluxes τ_{ij} and the exchange coefficient tensor K_{ij} are symmetric, hence that $\tau_{12} = \tau_{21}$, $K_{12} = K_{21}$ etc. Besides, identities are assumed for all horizontal and all vertical exchange coefficients:

$$\begin{aligned} &K_{11} = K_{12} = K_{21} = K_{22} = K_{hor} && \text{(a)} \\ &K_{13} = K_{23} = K_{31} = K_{32} = K_{33} = K_{vert} && \text{(b)} \end{aligned} \tag{3.4}$$

This reduces the number of exchange coefficients to be calculated to two values. Therefore, the components τ_{ij} of the turbulent stress tensor can be derived from the gradients of the average variables as follows:

$$\begin{aligned} {}_{11} &= -\rho_0 \overline{u'u'} = 2\rho_0 K_{hor} \left\{ \frac{\partial \overline{u}}{\partial \dot{x}^1} \frac{\partial \dot{x}^1}{\partial x} + \frac{\partial \overline{u}}{\partial \dot{x}^3} \frac{\partial \dot{x}^3}{\partial x} \right\} && \text{(a)} \\ \tau_{12} = \tau_{21} &= -\rho_0 \overline{u'v'} = \rho_0 K_{hor} \left\{ \frac{\partial \overline{u}}{\partial \dot{x}^2} \frac{\partial \dot{x}^2}{\partial y} + \frac{\partial \overline{u}}{\partial \dot{x}^3} \frac{\partial \dot{x}^3}{\partial y} + \frac{\partial \overline{v}}{\partial \dot{x}^1} \frac{\partial \dot{x}^1}{\partial x} + \frac{\partial \overline{v}}{\partial \dot{x}^3} \frac{\partial \dot{x}^3}{\partial x} \right\} && \text{(b)} \\ \tau_{13} = \tau_{31} &= -\rho_0 \overline{u'w'} = \rho_0 K_{vert} \left\{ \frac{\partial \overline{u}}{\partial \dot{x}^3} \frac{\partial \dot{x}^3}{\partial z} + \frac{\partial \overline{w}}{\partial \dot{x}^1} \frac{\partial \dot{x}^1}{\partial x} + \frac{\partial \overline{w}}{\partial \dot{x}^3} \frac{\partial \dot{x}^3}{\partial x} \right\} && \text{(c)} \\ \tau_{22} &= -\rho_0 \overline{v'v'} = 2\rho_0 K_{hor} \left\{ \frac{\partial \overline{v}}{\partial \dot{x}^2} \frac{\partial \dot{x}^2}{\partial y} + \frac{\partial \overline{v}}{\partial \dot{x}^3} \frac{\partial \dot{x}^3}{\partial y} \right\} && \text{(d)} \\ \tau_{23} = \tau_{32} &= -\rho_0 \overline{v'w'} = \rho_0 K_{vert} \left\{ \frac{\partial \overline{v}}{\partial \dot{x}^3} \frac{\partial \dot{x}^3}{\partial z} + \frac{\partial \overline{w}}{\partial \dot{x}^2} \frac{\partial \dot{x}^2}{\partial y} + \frac{\partial \overline{w}}{\partial \dot{x}^3} \frac{\partial \dot{x}^3}{\partial y} \right\} && \text{(e)} \\ \tau_{33} &= -\rho_0 \overline{w'w'} = 2\rho_0 K_{vert} \left\{ \frac{\partial \overline{w}}{\partial \dot{x}^3} \frac{\partial \dot{x}^3}{\partial z} \right\} && \text{(f)} \end{aligned} \tag{3.5}$$

Note that $\frac{\partial \dot{x}^1}{\partial y}, \frac{\partial \dot{x}^2}{\partial x}$ etc. are zero, equation (A.7). These formulations are used in both types of turbulence parameterizations.

3.2 Sub-grid scale fluxes for scalar quantities

The sub-grid scale turbulent transport terms of any scalar variable χ (e.g. potential temperature θ in the coordinate system $\dot{x}$ can be written as

$$\begin{aligned} F_\chi = &\frac{\partial}{\partial \dot{x}^1} \left\{ \rho_0 \overset{*}{\alpha} \overline{u'\chi'} \frac{\partial \dot{x}^1}{\partial x} \right\} + \frac{\partial}{\partial \dot{x}^2} \left\{ \rho_0 \overset{*}{\alpha} \overline{v'\chi'} \frac{\partial \dot{x}^2}{\partial y} \right\} \\ &+ \frac{\partial}{\partial \dot{x}^3} \left\{ \rho_0 \overset{*}{\alpha} \overline{u'\chi'} \frac{\partial \dot{x}^3}{\partial x} + \rho_0 \overset{*}{\alpha} \overline{v'\chi'} \frac{\partial \dot{x}^3}{\partial y} + \rho_0 \overset{*}{\alpha} \overline{w'\chi'} \frac{\partial \dot{x}^3}{\partial z} \right\} \end{aligned} \tag{3.6}$$

The sub-grid scale turbulent fluxes $\overline{u_i' \chi'}$ are also parameterized by use of a first order closure:

$$-\rho_0 \overline{u_i' \chi'} = \rho_0 K_{i,\chi} \left(\frac{\partial \bar{\chi}}{\partial \dot{x}^k} \frac{\partial \dot{x}^k}{\partial x^i} - \delta_{i3} \Gamma_\chi \right) \tag{3.7}$$

The countergradient term Γ_χ is only considered in the vertical flux and if selected for a convective situation.

Similar assumptions as already described for the exchange coefficients of momentum yield:

$$\begin{aligned} -\rho_0 \overline{u' \chi'} &= \rho_0 K_{hor,\chi} \left\{ \frac{\partial \bar{\chi}}{\partial \dot{x}^1} \frac{\partial \dot{x}^1}{\partial x} + \frac{\partial \bar{\chi}}{\partial \dot{x}^3} \frac{\partial \dot{x}^3}{\partial x} \right\} \quad \text{(a)} \\ -\rho_0 \overline{v' \chi'} &= \rho_0 K_{hor,\chi} \left\{ \frac{\partial \bar{\chi}}{\partial \dot{x}^2} \frac{\partial \dot{x}^2}{\partial y} + \frac{\partial \bar{\chi}}{\partial \dot{x}^3} \frac{\partial \dot{x}^3}{\partial y} \right\} \quad \text{(b)} \\ -\rho_0 \overline{w' \chi'} &= \rho_0 K_{vert,\chi} \left\{ \frac{\partial \bar{\chi}}{\partial \dot{x}^3} \frac{\partial \dot{x}^3}{\partial z} - \Gamma_\chi \right\} \quad \text{(c)} \end{aligned} \tag{3.8}$$

In case of using the non-local scheme equation (3.8c) results in

$$-\rho_0 \overline{w' \theta'} = \rho_0 K_{vert,\theta} \left\{ \frac{\partial \bar{\theta}}{\partial \dot{x}^3} \frac{\partial \dot{x}^3}{\partial z} - \Gamma_\theta \right\} \tag{3.9}$$

$$-\rho_0 \overline{w' q'} = \rho_0 K_{vert,q} \left\{ \frac{\partial \bar{q}}{\partial \dot{x}^3} \frac{\partial \dot{x}^3}{\partial z} - \Gamma_q \right\}, \tag{3.10}$$

where Γ_θ and Γ_q are the corresponding countergradient transport terms. The determination of exchange coefficients and countergradient terms is described in Section 3.4.

3.3 Surface fluxes

To calculate sub-grid scale turbulent fluxes below the first scalar grid level (usually set to $z_{k=1} = 10$ m in METRAS and to 2-5 m in MITRAS), the validity of surface layer similarity theory is assumed. The grid box averaged values of u_*, θ_* and q_* can be calculated with two different methods.

It should be noted here that the turbulent fluxes of momentum, heat and humidity are not pre-defined by the model-users, but diagnostically derived from prognostic model variables. Therefore the friction velocity u_* given by METRAS can be used as input data for oceanographic simulations.

3.3.1 Parameter averaging

The parameter averaging method assumes grid box averaged roughness lengths z_0:

$$z_0 = \sum_j f_j z_0^j \tag{3.11}$$

f_j is the fraction of the sub-grid scale surface class j within the surface grid box and z_0^j the roughness length of the sub-grid scale surface class j.

u_* results from the following equation:

$$u_* = \frac{\kappa V(z_{k=1})}{ln(z_{k=1}/z_o) - \psi_m(z_{k=1}/L)} \tag{3.12}$$

where $z_{k=1}$ is the height of the lowest model level above the ground. The velocity is the surface parallel component of the wind velocity vector. For the calculation of u_* a minimum value of 0.1 m is assumed for $V(z_{k=1})$. The integral stability function for momentum $\psi_m(z/L)$ is calculated according to Dyer (1974) as

$$\psi_m(z/L) = \begin{cases} 2\ln[(1+\phi_m^{-1})/2] + \ln[(1+\phi_m^{-2})/2] - 2\arctan(\phi_m^{-1}) + \pi/2 & for \quad z/L \le 0 \\ -5.0 z/L & for \quad z/L > 0 \end{cases} \tag{3.13}$$

with $\kappa = 0.4$. The stability function for heat is given by

$$\phi_m = \begin{cases} (1-16\ z/L)^{-1/4} & \text{for} \quad z/L \le 0 \quad \text{unstable} \\ 1+5z/L & \text{for} \quad z/L > 0 \quad \text{stable} \end{cases} \tag{3.14}$$

The similarity function of heat is assumed as

$$\begin{aligned} \phi_h &= \phi_m^{\,2} \quad \text{for} \quad z/L \le 0 \\ \phi_h &= \phi_m \quad \text{for} \quad z/L > 0. \end{aligned} \tag{3.15}$$

In the model code the similarity functions are sometimes given as functions of *Ri* using the relation

$$Ri = \frac{\phi_h}{\phi_m^2}\frac{z}{L} \tag{3.16}$$

together with the assumption (3.15) for the stability function the relation is:

$$\begin{aligned} Ri &= z/L \qquad \text{for } z/L \le 0 \quad \text{unstable} \\ Ri &= z/L \cdot \phi_m^{-1} \quad \text{for } z/L > 0 \quad \text{stable} \end{aligned} \tag{3.17}$$

The stability function ψ_h for heat is calculated as:

$$\psi_h(z/L) = \begin{cases} 2ln\left[\dfrac{1+(1-16.0(z/L))^{0.5}}{2}\right] & \text{for } z/L < 0 \\ -5.0 z/L & \text{for } z/L > 0 \end{cases} \tag{3.18}$$

Equations 3.13 to 3.20 are assumed to be valid in the stability range $-2 \le z/L \le 1$ for the Dunst (1982) scheme described in Section 3.4.1.

The Monin-Obukhov-Length L is defined by equation (3.19). The values are limited to $\pm$ 200 m, resulting in $\left|z/L \le 3 \cdot 10^{-3}\right|$ to be treated as neutral.

$$L = \frac{\bar{\theta}\, u_*^2}{g\kappa\left[\theta_*\left(1+\bar{q}_v\right)+\left(\frac{R_1}{R_2}-1\right)\bar{\theta}q_*\right]} \tag{3.19}$$

The scaling value for temperature is calculated (e.g. Pielke, 1984) as

$$\theta_* = \kappa \frac{\bar{\theta}(z_{k=1}) - \bar{\theta}(z_o)}{\ln(z_{k=1}/z_{o,\chi}) - \psi_h(z_{k=1}/L)} \tag{3.20}$$

For the calculation of surface fluxes of other scalar quantities χ the similarity functions of heat are used and the scaling values are given by

$$\chi_* = \kappa \frac{\bar{\chi}(z_{k=1}) - \bar{\chi}(z_o)}{\ln(z_{k=1}/z_{o,\chi}) - \psi_h(z_{k=1}/L)} \tag{3.21}$$

3.3.2 Flux averaging

The second method for the calculation of the near-surface turbulent fluxes is the so-called flux averaging method, which is implemented in METRAS according to Claussen (1991), Herrmann (1994) and von Salzen et al. (1996) using the concept of blending heigth. As a first step, sub-grid scale surface fluxes of momentum ($\sim(u_{*,j})^2$), heat ($\sim(u_{*,j}\cdot\theta_{*,j})$) and moisture ($\sim(u_{*,j}\cdot q_{*,j})$) are calculated for each surface class j. Second, the total flux results as an average of these individual fluxes, weigthed by the respective surface fraction f_j. Thus the mean scaling values u_*, θ_* and q_* follow as:

$$u_* = \sqrt{\sum_j f_j \cdot (u_{*,j})^2} \tag{3.22}$$

$$\chi_* = \frac{1}{u_*}\sum_j \left(f_j \cdot u_{*,j} \cdot \chi_{*,j}\right) \tag{3.23}$$

The scaling values $u_{*,j}$ and $\chi_{*,j}$ of the sub-grid scale surface fluxes are defined as:

$$u_{*,j} = \sqrt{\hat{C}_{m,j}} \cdot V(z_{k=1}) \tag{3.24}$$

$$\chi_{*,j} = \frac{\hat{C}_{h,j}}{\sqrt{\hat{C}_{m,j}}} \cdot \left(\bar{\chi}(z_{k=1}) - \bar{\chi}_j(z_{0,j})\right) \tag{3.25}$$

C_h and C_m are the near-surface transfer coefficients of momentum and heat, respectively. The temperature $\bar{\theta}_j(z_{0,j})$ of the sub-grid scale surface class j is calculated from a surface energy budget equation (Section 7.1.2).

The transfer coefficients are determined as a function of the blending height l_b, which is defined as the height in which the flow is assumed to become homogeneous within a grid

cell with nonhomogeneous surface. l_b depends on the effective roughness z_0 and the degree of sub-grid scale heterogeneity of the terrain. The effective transfer coefficients $\hat{C}_{m,j}$ and $\hat{C}_{h,j}$ are approximated as:

$$\hat{C}_{m,j} = \frac{\kappa^2}{\left[\ln\frac{l_b}{z_{0,j}} \cdot \frac{\ln(z_{k=1}/z_0)}{\ln(l_b/z_0)} - \psi_m\left(\frac{z_{k=1}}{L_j}\right)\right]^2} \tag{3.26}$$

$$\hat{C}_{h,j} = \frac{\kappa^2}{\left[\ln\frac{l_b}{z_{0,j}}\frac{\ln(z_{k=1}/z_0)}{\ln(l_b/z_0)} - \psi_m\left(\frac{z_{k=1}}{L_j}\right)\right]\left[\ln\frac{l_b}{z_{0t,j}}\frac{\ln(z_{k=1}/z_{0t})}{\ln(l_b/z_{0t})} - \psi_h\left(\frac{z_{k=1}}{L_j}\right)\right]} \tag{3.27}$$

In contrast to the definition of z_0 as an average of the roughness lengths $z_{0,j}$ of the sub-grid scale surface classes (3.11), the effective roughness length z_0 is now obtained by solving the equations

$$\frac{1}{\left(\ln\frac{l_b}{z_0}\right)^2} = \sum_j \frac{f_j}{\left(\ln\frac{l_b}{z_{0,j}}\right)^2} \tag{3.28}$$

and

$$\frac{l_b}{l_*}\left(\ln\frac{l_b}{z_0}\right) = c_1\kappa \quad \text{with} c_1 = 1.75 \tag{3.29}$$

by iteration. l_* is the characteristic length of sub-grid scale surface elements of even roughness.

The roughness length $z_{0,\theta,j}$ for heat of the sub-grid scale surface class j and the effective roughness length $z_{0,\theta}$ for heat are calculated from equation-**Fehler! Verweisquelle konnte nicht gefunden werden.**, the Monin-Obukhov-Length L_j of class j from equation (3.19).

3.3.3 Roughness length adjustment for special surface types

Several surface types (‘ice’, ‘urban’ and ‘water’) require specific adjustments to the parameterizations to best represent certain physical processes. These special surface types are defined below. Here, we introduce adjustments made to roughness lengths (both momentum and scalar) as a function of surface type. For all surface classes not designated as a ‘water’ surface type, the momentum roughness length, $z_{0,j}$, is set to a constant value according to Section 3.2.3 of Schlünzen et al. (2018).

To take into account the difference in exchange processes of momentum and scalar quantities χ (e.g., moisture and heat), the scalar roughness lengths of all surface classes not assigned to any special surface type are calculated according to Hicks (1985):

$$\frac{z_0}{z_{0\chi}} = 10. \tag{3.30}$$

Equation (3.30) assumes a surface consisting of dense, permeable roughness elements (vegetation).

Over **water**, the momentum roughness length depends on the wind velocity. The relation by Charnock (1955) is used. For small friction velocities ($u_* < 0.146$) the calculation followsClarke (1970); for large friction velocities ($u_* > 0.190$) the calculation follows Wu (1980); in between $7 \cdot 10^{-5}$ is used.:

$$z_{0,j}(x,y) = \max\left(\min\left(\max\left(0.032 \cdot u_*^2 / g\ , 1.5 \cdot 10^{-5}\ m\right), 7 \cdot 10^{-5}\ m\right), 0.0185 \cdot u_*^2 / g\right) \tag{3.31}$$

For scalar roughness length, water is assumed to be a hydrodynamically rough surface (a.k.a bluff-body), whose roughness elements have a width normal to the mean flow that exceeds their height. For water, the scalar roughness length is calculated according to Brutsaert (1975; 1982) as:

$$\frac{z_0}{z_{0\theta}} = \max\left[z_0/442413\ , (z_0/\exp(\kappa(7.3 Re_*^{1/4}\sqrt{0.71} - 5))\right] \tag{3.32}$$

$$\frac{z_0}{z_{0q}} = \max\left[z_0/442413\ , (z_0/\exp(\kappa(7.3 Re_*^{1/4}\sqrt{0.6} - 5))\right] \tag{3.33}$$

where $Re_* = u_* z_0/\nu$ is the roughness Reynoldsnumber.

Urban surfaces are also treated as hydrodynamically rough surfaces. For all urban surface types, the model follows the approach of Kanda et al. (2007) for scalar roughness lengths

$$\frac{z_0}{z_{0\theta}} = \max\left[z_0/442413\ , (z_0/\exp(\kappa(3.83 Re_*^{1/4}\sqrt{0.71} - 5))\right] \tag{3.34}$$

$$\frac{z_0}{z_{0\chi}} = \max\left[z_0/442413\ , (z_0/\exp(\kappa(3.83 Re_*^{1/4}\sqrt{0.6} - 5))\right] \tag{3.35}$$

which is fitted for urban canopies (combined buildings and street canyons) devoid of vegetation. Here, the surface type ‘urban’ refers to any surface consisting only of structures and their adjacent sealed surfaces (devoid of vegetation).

In grid cells containing a mixture of sea ice and water an additional form drag term (10.12) contributes to the momentum flux, whereas no (special) modifications of the roughness lengths are done.

3.4 Exchange coefficients

The exchange coefficients below $z_a \leq 10\,\mathrm{m}$ are always calculated from surface layer similarity theory by using the following equations, with Φ_m and Φ_h given in equation (3.13) and (3.14):

$$K_{vert} = \kappa u_* z/\Phi_m \tag{3.36}$$

$$K_{vert,\theta} = K_{vert,q} = \kappa u_* z/\Phi_h \tag{3.37}$$

The determination of exchange coefficients above $z_a = 10$ m depends on the type of parameterization used. METRAS uses alternatively a local mixing length scheme (Section 3.4.2), a scheme similar to that given by Dunst (1982) (Section 3.4.1), a non-local scheme given by Troen and Mahrt (1986) (Section 3.4.3) and a non-local scheme given by Lüpkes and Schlünzen (1996) (Section 3.4.4).

3.4.1 Scheme based on Dunst (1982)

The exchange coefficient determined after Dunst (1982) is similar to that used by Dunst and Rhodin (1990), with some modifications concerning the determination of the parameters β and A (Schlünzen, 1990). K_{vert} reads:

$$K_{vert} = \kappa u_* z_a \exp\left\{-\frac{3\pi}{\sqrt{15}}\frac{(z-z_a)}{H_S}\right\}\cdot\frac{\sin(\pi z/H_s)}{\sin(\pi z_a/H_n)} \cdot\left\{1-A\left[\left(\frac{\sqrt{15}H_s}{2\pi z}\right)^{0.134}\mathrm{Ri}-\left(\frac{\sqrt{15}H_s}{2\pi z}\right)^{0.268}\frac{\mathrm{Ri}^2}{2}\right]\right\} \tag{3.38}$$

The local gradient Richardson number Ri is calculated as follows:

$$Ri = \frac{g}{\bar{\theta}}\frac{\left(\frac{\partial\bar{\theta}}{\partial z}+0.61\,\bar{\theta}\cdot\frac{\partial\bar{q}}{\partial z}\right)}{\left(\left(\frac{\partial\bar{u}}{\partial z}\right)^2+\left(\frac{\partial\bar{v}}{\partial z}\right)^2+\zeta\right)} \tag{3.39}$$

The value $\zeta(\approx 10^{-8}/\Delta z^2)$ is added to ensure a nonzero denominator. The height H_s of the planetary boundary layer (PBL) is calculated depending on stability: $H_s = H_n(1-\beta\mathrm{Ri})$ with $H_n = 1000\,\mathrm{m}$. This value corresponds with the characteristic scale height of the PBL defined as $H_n = \kappa u_*/|f|$ (e.g. Etling, 1987).

To calculate H_s, $\beta = 5.1$ is used for stable stratification, whereas $\beta = 1.5$ is used for unstable stratification. These values have been estimated for typical atmospheric conditions and ensure PBL heights between 150 m and 2500 m. With these values for β the free constant A is estimated. It is determined to ensure the equality of the K_{vert}-values at height z_a for values calculated from equation (3.38) and derived from the surface layer similarity theory equation (3.36). Additionally it is ensured that the derivatives of functions (3.36), (3.38)with respect to stability result in similar values. For stable stratification, this results in $A = 2.7058 + 9.319\,Ri$ and for unstable stratification $A = 0.79 + 0.4\,Ri$ is used.

The exchange coefficient $K_{vert,\chi}$ for scalar quantities (e.g. temperature, water vapour, pollution concentrations) is calculated from the relation:

$$\frac{K_{vert,\chi}}{K_{vert}} = \frac{\Phi_m}{\Phi_h} \tag{3.40}$$

3.4.2 Mixing length scheme

The mixing length scheme used in METRAS is based on Herbert and Kramm (1985). The surface layer functions proposed by Dyer (1974) are used in the whole boundary layer while *z/L* is replaced by the local Richardson nuber using equation (3.16). This results in:

$$K_{vert} = \begin{cases} l_n^2 \left|\frac{\partial V}{\partial z}\right| (1-5Ri)^2 & 0 \le Ri \le 0.1\overline{6} \\ l_n^2 \left|\frac{\partial V}{\partial z}\right| (1-16Ri)^{1/2} & -2 \le Ri \le 0 \end{cases} \tag{3.41}$$

and

$$K_{vert,\chi} = \begin{cases} K_{vert} & 0 \le Ri \le 0.1\overline{6} \\ K_{vert}\,(1-16Ri)^{1/4} & -2 \le Ri \le 0 \end{cases}, \tag{3.42}$$

l_n is the mixing length for neutral stratification, which is specified according to Blackadar (1962) as

$$l_n = \frac{\kappa z}{1 + \frac{\kappa z}{0.007 u_* / f}}. \tag{3.43}$$

3.4.3 Countergradient scheme of Troen and Mahrt (1986)

Lüpkes and Schlünzen (1996) showed that for stable stratification the local mixing length scheme gives reasonable results. However, for unstable situations the eddy diffusivities are considerably underestimated. Higher values of K_{vert} are achieved by the scheme of Troen and Mahrt (1986), where the eddy diffusivities are independent of local properties of

the atmosphere. Instead of eq. (3.44) eq. (31) of Lüpkes and Schlünzen (1996) is used. In the AWI version of METRAS, eq. (32) of Lüpkes and Schlünzen (1996) is implemented to ensure continuous vertical fluxes at z = z(jk=1), as found out by Luepkes and Schluenzen (1996). For unstable stratification the exchange coefficients are given by

$$K_{vert} = u_* \kappa z (1 - \frac{z}{z_i})^2 (\Phi_m(z_{jk=1}))^{-1} \tag{3.44}$$

And

$$K_{vert,\chi} = (\frac{\Phi_h(z_p)}{\Phi_m(z_p)} + \kappa \frac{z_{jk=1}}{z_i} 6.5)^{-1} K_{vert} \tag{3.45}$$

The countergradient transport term (equations(3.9), (3.10)) for heat is parameterized by

$$\Gamma_\theta = 6.5 \frac{\overline{w'\Theta'}|_S}{w_S z_i} \tag{3.46}$$

Herein $\overline{w'\Theta'}|_S$ is the turbulent heat flux in the surface-layer. w_S is a convective velocity scale, defined by

$$w_s = u_* \Phi_m^{-1} = (u_*^3 + 7 \frac{z_{jk=1}}{z_i} \kappa w_f^3)^{1/3} \tag{3.47}$$

$z_{jk=1}$ denotes the surface-layer height, z_i is the height of the convective boundary-layer and w_f another convective velocity scale given by

$$w_f = (\frac{g}{\Theta_S} z_i \overline{w'\Theta'}|_S + \overline{w'q'}|_S)^{1/3} \tag{3.48}$$

The parameterization for Γ_q can be derived as

$$\Gamma_q = \Gamma_\theta \frac{q_*}{\theta_*} \tag{3.49}$$

The mixing layer height z_i is determined as the level, where the heat flux attains a minimum.

3.4.4 Countergradient scheme of Lüpkes and Schlünzen (1996)

The nonlocal closure for unstable stratification proposed by Lüpkes and Schlünzen (1996) is partly based on the scheme given in the previous section. Troen and Mahrt (1986) use more or less empirical formulations for the countergradient terms and the diffusivities. In contrast, the following scheme includes parameterizations, which are based on the prognostic equation of heat flux and on large-eddy simulations of Holtslag and Moeng (1991). These parameterizations have been modified to ensure continuity of the turbulent fluxes with respect to height and stratification at the first grid level. This requirement results in the following parameterization:

$$K_{vert,\chi} = \frac{\kappa u_* z_p}{(\Phi_h - \frac{\kappa z_p}{\Theta_*}\Gamma|_{z_p})}(\frac{z_i - z}{z_i - z_p})^2 \frac{u_*\kappa z + w_f z_i (z/z_i)^{4/3}}{u_*\kappa z_p + w_f z_i (z_p/z_i)^{4/3}}, \quad (z_i \geq z \geq z_p) \tag{3.50}$$

z_p is the height of the first grid level.

$$K_{vert} = \left[\frac{\Phi_h|_{z_p}}{\Phi_m|_{z_p}} + 3\frac{w_f u_* \kappa z_p}{\Phi_m|_{z_p}\,\overline{w'^2}|_{z_p}\,z_i}\right] K_{vert,\chi} \tag{3.51}$$

$$\Gamma_\theta = 3\frac{w_f^2 \Theta_f}{\overline{w'^2} z_i} \tag{3.52}$$

Herein the characteristic convective temperature scale is defined by

$$\Theta_f = \frac{\overline{w'\Theta'}\big|_s}{w_f}. \tag{3.53}$$

The variance of the vertical velocity $\overline{w'^2}$ is parameterized by

$$(\overline{w'^2})^{3/2} = [1.6\,u_*^2(1-\frac{z}{z_i})]^{3/2} + 1.2 w_f^3 (\frac{z}{z_i})(1-0.9\frac{z}{z_i})^{3/2} \tag{3.54}$$

This formulation is also based on large-eddy simulations for convective flow. The second term describes the effect of convection and the first one includes mechanical shear turbulence induced by the surface. Γ_q is again given by eq. (3.49) The mixing length scheme is taken for stable stratification. z_i is determined as described in Section (3.4.3).

The application of this scheme results in higher values of the mixed layer height, because the eddy diffusivities are even higher than those resulting from the scheme of Troen and Mahrt (1986). However, the values for Γ_θ calculated from eq. (3.52) are lower than those of the Troen and Mahrt scheme.

3.4.5 Prandtl-Kolmogorov-closure (TKE)

This closure solves a prognostic equation for the sub-grid scale turbulent kinetic energy $\overline{e}$. Local gradients are considered in local Richardson numbers Ri, non local transports are represented by countergradient terms. The exchange coefficients are calculated as

$$\begin{aligned} K_{vert} &= c_1 \cdot l \cdot (1 - 5Ri) \cdot \overline{e}^{1/2} \quad \text{for} \quad Ri > 0 \\ K_{vert} &= c_1 \cdot l \cdot (1 - 16Ri)^{1/4} \cdot \overline{e}^{1/2} \quad \text{for} \quad Ri \leq 0 \\ \\ K_{vert,\chi} &= c_1 \cdot l \cdot (1 - 5Ri) \cdot \overline{e}^{1/2} \quad \text{for} \quad Ri > 0 \\ K_{vert,\chi} &= c_1 \cdot l \cdot (1 - 16Ri)^{1/2} \cdot \overline{e}^{1/2} \quad \text{for} \quad Ri \leq 0 \end{aligned} \tag{3.55}$$

The proportionality constant c_1 is set to 0.5 and the mixing length (Blackadar, 1962) is calculated similar to (3.43) as

$$l = \frac{\kappa z}{1 + \kappa \dfrac{z - z_p}{\lambda}} \tag{3.56}$$

The z_p (height of the first grid level) term is needed to assure a steady flux at the lowest atmospheric model level (Prandtl-Layer). The eddy size λ is set to $\lambda = 0.022 \cdot u_* / f$ for stable and to $\lambda = 0.08 \cdot z_j$ for unstable stratification. Further modifications of the diffusion coefficients are caused by the Ri-Terms which can be interpreted as an adjustment of the mixing length to the atmospheric stability. With (3.16) it can be seen that the Ri terms are the same as the stability functions (3.14) - (3.15).The Richardson number is approximated as:

$$Ri \approx \frac{\dfrac{g}{\theta} \cdot \left(\dfrac{\partial \theta}{\partial z} + 0.61 \cdot \theta \dfrac{\partial q}{\partial z} \right)}{\left(\dfrac{\partial u}{\partial z} \right)^2 + \left(\dfrac{\partial v}{\partial z} \right)^2} \tag{3.57}$$

Some further remarks on limitations of this approximation can be found in Fock (2007). Molecular and pressure diffusion terms are neglected in the prognostic equation for the sub-grid scale turbulent kinetic energy. Counter gradient fluxes can modify the local buoyancy production term:

$$\begin{aligned} \frac{\partial \rho_0 \alpha^* \overline{e}}{\partial t} = {} & \frac{\partial \overline{u}_j \rho_0 \alpha^* \overline{e}}{\partial x_j} + \rho_0 \alpha^* \left(k_{ij} 2 S_{ij} - \frac{2}{3} \delta_{ij} \overline{e} \right) \frac{\partial \overline{u}_j}{\partial x_j} - \rho_0 \alpha^* \frac{g}{\theta_0} K_{vert,\chi} \left(\frac{\partial \overline{\theta}}{\partial z} - \Gamma_\theta \right) \\ & - \rho_0 \alpha^* g \cdot 0.61 \cdot K_{vert,\chi} \left(\frac{\partial q}{\partial z} - \Gamma_q \right) - \frac{\partial}{\partial x_j} \left(\rho_0 \alpha^* \overline{K_x \frac{\partial e}{\partial x_j}} \right) - \rho_0 \alpha^* \varepsilon \end{aligned} \tag{3.58}$$

The dissipation ε is calculated as

$$\varepsilon = 3/2 \cdot \frac{\overline{e}^{\,3/2}}{l_\varepsilon} \tag{3.59}$$

The characteristic dissipative length scale l_ε is calculated according Therry and Lacarrère (1983) in dependence of the atmospheric stability.

At the first atmospheric model level (e.g. at the height z_p) the turbulent kinetic energy is calculated as

$$\overline{e}_p = \frac{u_*^2}{c_1^2} \tag{3.60}$$

to guarantee a matching of the turbulent fluxes. This means that if the fluxes at z_p were calculated with the diffusion coefficients (3.36) - (3.37) they need to be the same as if they result from the diffusion coefficients (3.55). The absence of any stability term in equation

(3.60) is not a limitation to neutral stratification. Instead it is the result of using the stability functions (3.14) - (3.15) for the definition of equations (3.55).

3.4.6 TKE-Epislon-closure

The TKE-Epsilon closure is similar to the Prandtl-Kolmogorov-Closure but an additional prognostic equation for the dissipation ε is solved.

3.4.7 LES subgrid scale model

The model METRAS-LES is suitable for large eddy simulation and includes a special closure for subgrid scale turbulence. Due to the conceptual difference between RANS and LES applications of the model METRAS this closure needs to be different from the RANS closures as only a part of the turbulent exchange is treated as a subgrid scale process. The implemented closure is the Deardorff (1980) closure, which shows some formal similaties with the Prandtl-Kolmogorov-closure (Section 3.4.5) as it also applies a prognostic equation for subgrid scale turbulent kinetic energy. One of the main difference is in the used length scale, which is the characteristic grid length scale $\Delta = (\Delta x \cdot \Delta y \cdot \Delta z)^{1/3}$ in the LES model. Further details can be found in Fock (2007).

3.4.8 Horizontal exchange coefficients

The horizontal exchange coefficient K_{hor} can be derived from the vertical exchange coefficient dependent on the grid increment (Dunst, 1980):

$$K_{hor} = r\frac{\sqrt{\Delta x^2 + \Delta y^2}}{\Delta z} K_{vert} \tag{3.61}$$

The parameter r can be chosen between 0.4 and 0.8. In METRAS r = 0.71 is used, resulting in $K_{hor} \cong 50\,m^2 s^{-1}$ for a typical $K_{vert} \cong 10^2 s^{-1}$, horizontal grid intervals of $\Delta x = \Delta y = 500\,m$ and a vertical grid interval of $\Delta z = 100\,m$ equation (3.61) is based on the assumption that the ratio of horizontal and vertical exchange coefficients is independent from the stability but proportional to the ratio of the horizontal $(\Delta x, \Delta y)$ and vertical (Δz) scales of the smallest eddies resolved by the grid. It is only applied in METRAS for grid sizes below 1000 m.

3.5 Parameterization of cloud microphysics

Microphysical processes of cloud and rain formation are parameterized in METRAS by following the suggestion first presented by Kessler (1969). The Kessler scheme is based on the idea that the liquid water in the atmosphere can be classified in cloud water with a mean droplet radius of about 10 μm and rain water with a mean droplet radius of about

$100\,\mu m$. Both classes are separated by $r \cong 40\,\mu m$. The size distribution of the rain water can be described by the Marshall-Palmer distribution (Marshall and Palmer, 1948).

The parameterization scheme includes

- condensation of water vapor to cloud water
- evaporation of cloud water to water vapor
- auto conversion of cloud water to rain water by collision of cloud droplets
- conversion of cloud water to rain water by collection of cloud droplets (accretion)
- sedimentation of rain water
- evaporation of falling rain drops in sub-saturated layers below clouds

Since rain-drop-growth by condensation and sedimentation of cloud droplets is of minor importance, these processes are neglected in the parameterization scheme. With this parameterization it is only necessary to solve two additional prognostic equations of the type (2.29), one for cloud water and one for rain water. Both equations and the prognostic equations for specific humidity and potential temperature are coupled by source/sink terms that include the processes listed above.

Due to the restriction to only two additional prognostic equations and the comparatively simple representation of cloud microphysics this parameterization requires an acceptable amount of computer resources, which still is a limitation factor in high-resolution modelling. Nevertheless, it describes the most important processes of cloud and rain formation in a satisfactory way. It is well known, however, that the Kessler scheme tends to overestimate the auto conversion and accretion processes in the early stage of cloud formation resulting in overestimated initial rain rates (e.g. Lüpkes, 1991).

The phase changes of water vapor to cloud droplets and reverse due to condensation and evaporation are calculated by the method of saturation adjustment (Asai, 1965). The values of a variable $\bar{\chi}$ at the next time step $n+1$ are obtained by $\bar{\chi}^{n+1} = \hat{\chi}^{n+1} + \Delta\chi$, where $\hat{\chi}^{n+1}$ denotes a `preliminary' value between time step n and $n+1$ due to advection and diffusion only. The temporal changes of specific humidity Δq_1^1, cloud water content Δq_1^{2c} and potential temperature $\Delta\theta$ are given by

$$\Delta q_1^1 = \begin{cases} 0 & \text{for } \hat{q}_1^1 < \hat{q}_1^{1sat}(\hat{\theta}) \text{ and } \hat{q}_1^{2c} = 0 \\ min\left\{ -\frac{1}{\beta}(\hat{q}_1^1 - \hat{q}_1^{1sat}(\hat{\theta})), \hat{q}_1^{2c} \right\} & \text{else} \end{cases} \tag{3.62}$$

$$\Delta q_1^{2c} = -\Delta q_1^1 \tag{3.63}$$

$$\Delta\theta = -\frac{l_{21}\cdot\Delta q_1^1}{c_p\cdot\Pi_o} \tag{3.64}$$

The auto conversion of cloud droplets to rain drops starts when the cloud water content exceeds the critical value $q_{1cri}^{2c} = 10^{-3}\ \mathrm{kg\,m^{-3}}$. For larger values the auto conversion rate rises linear with the cloud water content:

$$\left.\frac{\partial \bar{q}_1^{2r}}{\partial t}\right|_{Au} = \begin{cases} k\cdot(\hat{q}_1^{2c} - q_{1cri}^{2c}) & \text{for } \bar{q}_1^{2c} > q_{1cri}^{2c} \\ 0 & \text{else} \end{cases} \tag{3.65}$$

$$\Delta q_1^{2c} = -\Delta q_1^{2r} \tag{3.66}$$

The time constant in (3.65) is set up to $k = 10^{-3}\,\mathrm{s^{-1}}$

The accretion rate depends on the probability that rain drops `catch' cloud droplets during their fall through cloud layers. This probability can be expressed by the so-called collection efficiency. Within the considered concept of warm rain, the assumption of a constant collection efficiency $E = 1$ is justified (Doms and Herbert, 1985). The changes in rain and cloud water content per time step can then be written

$$\left.\frac{\partial q_1^{2r}}{\partial t}\right|_{Ak} = \sqrt{\frac{\rho_s}{\rho_o}}\cdot 934.63\cdot\hat{q}_1^{2c}\cdot(10^{-3}\cdot\rho_o\cdot\hat{q}_1^{2r})^{0.875} \tag{3.67}$$

$$\Delta q_1^{2c} = -\Delta q_1^{2r} \tag{3.68}$$

where the term $\sqrt{\rho_s/\rho_o}$ with a reference density $\rho_s = 1.29\ \mathrm{kg\,m^{-3}}$ ensures the applicability of equation (3.67) also to deep convection.

With the assumption of a Marshall-Palmer rain drop size distribution the sedimentation flux of rain is taken into account by

$$\Delta q_1^{2r} = \frac{\Delta t}{\rho_o}\cdot\frac{\partial}{\partial z}(V_{TR}\cdot\rho_o\cdot\hat{q}_1^{2r}) \tag{3.69}$$

where

$$V_{TR} = \sqrt{\frac{\rho_s}{\rho_o}}\cdot 29.13(10^{-3}\cdot\rho_o\cdot\hat{q}_1^{2r})^{0.125} \tag{3.70}$$

denotes the terminal velocity of rain drops. In equation (3.70) $\sqrt{\rho_s/\rho_o}$ represents the height dependence of V_{TR} due to density changes with height.

When rain drops fall through subsaturated layers below clouds they may evaporate again. This process depends on the subsaturation as well as on the rain drop size distribution and their terminal velocity, expressed in the term A_t and a ventilation factor F_v, respectively:

$$\Delta q_1^{2r} = - \max \left\{ \hat{q}_1^{2r} \frac{10^3 \cdot \Delta t}{\rho_o} \cdot A_t \cdot \sqrt{10^{-3} \rho_o \hat{q}_1^{2r}} \cdot F_v \cdot S \right\} \tag{3.71}$$

$$\Delta q_1^1 = -\Delta q_1^{2r} \tag{3.72}$$

$$\Delta \theta = -\frac{l_{21}}{c_p \cdot \Pi_o} \cdot \hat{q}_1^{2r} \tag{3.73}$$

with

$$A_t = \frac{2.623 \cdot 10^{-3} (10^{-3} \cdot \rho_o \cdot \hat{q}_1^{1sat}(\hat{\theta}))}{1 + 1.282 \cdot 10^{10} (10^{-3} \cdot \rho_o \cdot \hat{q}_1^{1sat}(\hat{\theta})) \cdot \hat{T}^{-2}} \tag{3.74}$$

characterizing the rain drop spectra and

$$F_v = 0.78 + 80.73 \cdot (10^{-3} \cdot \rho_o \cdot \hat{q}_1^{2r})^{0.225} \tag{3.75}$$

The subsaturation is given by

$$S = \frac{\hat{q}_1^{1sat}(\hat{\theta}) - \hat{q}_1^1}{\hat{q}_1^{1sat}(\hat{\theta})} \cdot 100 \tag{3.76}$$

It should be pointed out that, unlike to this chapter, most literature on cloud physics give the formulas in cgs-units. For clarity, all equations listed above refer to SI-units, resulting in a number of additional factors 10^{-3}. Further details on the parameterization of cloud microphysics in METRAS are given by Köhler (1990).

3.6 Parameterization of radiation

Two different parameterizations for radiative fluxes are implemented in METRAS to take into account the heating and cooling of the surface and atmosphere due to the net radiation. If a simulation without microphysics is performed, only the longwave and shortwave radiation balance at the earth's surface is computed. This computation is carried out with respect to the geographical position, date and time, rotation of the used coordinate system against North, inclined surfaces and shading of areas due to neighboring hills. Details on this parameterization are given in Section 7.1.2 and Appendix A.5.

In case of model calculations with the formation of clouds, the radiation fluxes at the earth's surface and in the atmosphere are parameterized by use of a two-stream approximation scheme. This scheme takes into account absorption and reflection of longwave and shortwave radiation by water vapor and liquid water and leads to cooling or heating not only at the surface but also at each grid point above. Here only the basic ideas of the scheme are described, details are given by Bakan (1994).

The cooling rate at a grid point k (counting in vertical direction) due to longwave radiation flux divergences is given by

$$\left.\frac{\partial \bar{T}}{\partial t}\right|_k^{rad} = -\frac{1}{\rho_0 c_p}\left.\frac{dF_N}{dz}\right|_k \tag{3.77}$$

with the radiation flux

$$F_N|_k = F_\uparrow^+ - F_\uparrow^- + F_\downarrow^- - F_\downarrow^+ \tag{3.78}$$

where "+" and "-" denote locations at the upper and lower boundary of the grid volume k respectively. With B the Planck function, σ a volume absorption coefficient and β=1.66 a diffusivity parameter, the up- and downward fluxes can be written as

$$\begin{aligned} F_\uparrow^+ &= F_\uparrow^- \cdot e^{-\beta\sigma\Delta z} + B^+ - B^- \cdot e^{-\beta\sigma\Delta z} - \frac{B_z}{\beta\sigma}(1-e^{-\beta\sigma\Delta z}) \qquad \text{(a)} \\ F_\downarrow^- &= F_\downarrow^+ \cdot e^{-\beta\sigma\Delta z} + B^- - B^+ \cdot e^{-\beta\sigma\Delta z} - \frac{B_z}{\beta\sigma}(1-e^{-\beta\sigma\Delta z}) \qquad \text{(b)} \end{aligned} \tag{3.79}$$

For shortness B_z means the vertical gradient of B equations (3.79) are separately solved for different spectral ranges.

Within the atmospheric window $(8.33 - 11.11\,\mu m)$ absorption by liquid water is the dominant process. The absorption coefficient for liquid water is taken following Buykov and Khvorostyanov (1977)

$$\sigma_l = 50 \cdot \rho_0 (\bar{q}_1^{2c} + \bar{q}_1^{2r}) \tag{3.80}$$

and for water vapour

$$\sigma_v = 1.38 \cdot \rho_0 \cdot (\bar{q}_1^{1})^2 \cdot \frac{\bar{p}}{p_o} \cdot e^{\left(\frac{1800}{\bar{T}} - 6.08\right)} \tag{3.81}$$

where p/p_o takes into account the pressure dependency of the absorption. The Planck function can be written as

$$B_{win} = \pi[88.75 - 0.9706 \cdot \bar{T} \cdot (1 - 0.002851 \cdot \bar{T})] \tag{3.82}$$

Instead of a detailed description of CO_2 absorption between 13 and 18 μ m the black body irradiance of CO_2 is parameterized by

$$B_{CO_2} = \pi[10.63 - 0.1679 \cdot \bar{T} \cdot (1 - 0.004025 \cdot \bar{T})] \tag{3.83}$$

Outside of the 8.33 – 11.11 μ m and 13-18 μ m range, spectral absorption by water vapour is dominant. Since it strongly depends on the wavelength, the transmission function is expanded into a sum of exponential functions with separate absorption coefficients of different weights

$$\sigma_v^i = 10^3 \cdot \rho_0 \cdot \bar{q}_1^{1} \cdot \frac{\bar{p}}{p_o} \cdot \tilde{\sigma}_v^i \qquad i = 1,8 \tag{3.84}$$

Where $\tilde{\sigma}_v$ denotes the volume absorption coefficient of water vapor as given in Table 3.1.

i	$\tilde{\sigma}_v^i$ [m²/kg]
1	$4.285 \cdot 10^{+1}$
2	$6.053 \cdot 10^{\pm 0}$
3	$8.550 \cdot 10^{-1}$
4	$1.208 \cdot 10^{-1}$
5	$1.706 \cdot 10^{-2}$
6	$2.410 \cdot 10^{-3}$
7	$3.404 \cdot 10^{-4}$
8	$4.808 \cdot 10^{-5}$

Table 1: Volume absorption coefficients of water vapour.

In practice the range $i = 8$ can be neglected due to its minor weight.

Subtracting the Planck function for the atmospheric window and the CO_2 range yields

$$B_{out} = \sigma T^4 - B_{win} - B_{CO_2} \tag{3.85}$$

where $\sigma = 5.67032 \cdot 10^{-8}$ $Wm^{-2}K^{-4}$ is the Stefan-Boltzmann constant.

The downward solar radiation flux can be written as a product of several transmission factors:

$$E = E_0 \cdot \mu \cdot T_E \cdot T_V \cdot T_D \cdot T_L \cdot f_A \tag{3.86}$$

where E_0 denotes the solar constant, $\mu = cos\,Z(t)$ with $Z(t)$ the zenith angle (Appendix A.5), f_A is a function of albedo and T are transmission factors due to Rayleigh scattering (T_E), absorption by water vapor (T_V), absorption and scattering by aerosols (T_D) and liquid water (T_L). (3.86) is separately calculated for the visible range 1 ($\lambda < 0.75\mu m$) and a near infrared range 2 ($\lambda > 0.75\mu m$). Within the radiation module of METRAS $T_{E2} = T_{V1} = T_{D1} = f_{A1} = f_{A2} = 1$ is assumed. The solar constants of both ranges are taken as E_{o1}= 707 W/m² and E_{o2}=660 W/m².

The transmission factor for Rayleigh scattering is derived from a suggestion of Atwater and Brown (1974) (Bakan, 1994)

$$T_{E1} = 1.041 - 0.16\sqrt{\frac{0.962 \cdot \bar{p}/p_o + 0.051}{\mu}} \tag{3.87}$$

and scattering by liquid water is parameterized following Stephans et al. (1984)

$$T_{L1} = \frac{1}{1+\beta_1 \tau_{N1}/\mu} \tag{3.88}$$

where $\beta_1 = 0.08\sqrt{\mu}$ is the backscattering fraction, $\tau_{N1} = 1.8336\,(\log_{10} W_L)^{3.963}$ the optical thickness of a cloud, and $W_L = 10^3 \int_z^\infty \rho_0 (\bar{q}_1^{2c} + \bar{q}_1^{2r}) dz [g/m^2]$ the liquid water mass above the location under consideration.

In the near infrared, absorption by water vapor is given by

$$T_{V2} = 1 - 0.193 (W_V/\mu)^{0.37} \tag{3.89}$$

with

$$W_V = 10^{-1} \int_z^\infty \frac{\bar{p}}{p_0} \cdot \rho_0 \cdot \bar{q}_1^1 dz [g/m^2] \tag{3.90}$$

the mass of water vapor analogous to W_L. As in (3.81) and (3.84) the factor $\bar{p}/p_o$ takes the pressure dependency of the absorption into account. The transmission factor for liquid water is formulated following Stephans et al. (1984):

$$T_{L2} = 4 \cdot \mu / R \tag{3.91}$$

with

$$R = (u+1)^2 \cdot e^{\tau eff} - (u-1)^2 e^{-\tau eff}$$

$$\tau_{eff} = \frac{\tau_{N2}}{\mu} \sqrt{(1-\omega)(1-\omega+2\beta_2\omega)}$$

$$u^2 = \frac{1-\omega+2\beta_2\omega}{1-\omega}$$

$$\tau_{N2} = 2.2346\,(\log_{10} W_L)^{3.8034}$$

$$\omega = 1 - 0.004 \cdot \mu^2 \cdot \ln(500/\tau_N)$$

$$\beta_2 = 0.12 \cdot \sqrt{\mu} / \ln(3 + \tau_N/10)$$

$$\tau_N = \tau_{N2}(W_L(z=0))$$

The corresponding reflectivity is calculated from

$$R_{L2} = (e^{\tau_{eff}} - e^{-\tau_{eff}}) \frac{u^2 - 1}{R} \tag{3.92}$$

For further details especially on the vertical integration of the radiation fluxes, their transmission and reflectivity Bakan (1994).

4 Pollutant processes

4.1 Chemical transformations

4.1.1 Gas-phase-reactions systems

Besides calculating passive tracer transport, chemical reactions can also be calculated with M-SYS. Both, transport and reactions-, are included in the model system. Thus at each timestep the new wind, temperature, and humidity fields are available for the transport and also for the calculation of the reaction rates.

The photolytic reactions are solved with

$$k_{hv} = D_1 \cdot \exp\left(\frac{-D_2}{\cos Z(t)}\right) \tag{4.1}$$

where D_1 and D_2 are constant values given in Chapter 6 of Schlünzen et al. (2018) and $cos\,Z(t)$ is the cosine of the zenith angle of the sun. The changing of the photolytic rate with height or due to clouds are not considered.

All non-photolytic reaction constants are solved with

$$k = D_3 \cdot \exp\left(\frac{-D_4}{R} T\right) \tag{4.2}$$

D_3 is a factor depending on the reaction, D_4 the activation energy and R the gas constant. The values for D_3 and $D_5 = D_4/R$ are given in Chapter 6 of Schlünzen et al. (2018). The rate constants have to be in mol, m^3, s units to be consistent with the reaction scheme.

4.1.2 Formation of ammonium aerosols

The formation of ammonium aerosols can be added to the gas phase reactions. The two reactions are gas-to-particle reactions, where ammonium nitrate and ammonium sulfate is formed. These reactions cannot be solved in the same way as the gas phase reaction with the QSSA-algorithm. In a very fast reaction ammonium sulfate is formed from sulfate and ammonium (Seinfeld (1986))

$$3NH_3 + 2SO_4^{2-} \rightarrow (NH_4)_2 SO_4 \tag{4.3}$$

The rest of ammonia reacts with nitric acid (HNO_3) to ammonium nitrate

$$NH_3 + HNO_3 \rightarrow NH_4NO_3 \tag{4.4}$$

This reaction depends on the dissociation constant K, which is for the solid ammonium nitrate only a function of temperature.

$$\ln K = 84.6 - \frac{24220}{T} - 6.1\ln\left(\frac{T}{293}\right) \quad \left[\text{ppb}^2\right] \tag{4.5}$$

For a humidity above the of deliquescence value, ammonium nitrate will be in the aqueous state. A dissociation constant comparable to equation (4.5) but involving aqueous ammonium nitrate can be found. It is a function of temperature and relative humidity (Seinfeld, 1986). As simplification of the equations described in Seinfeld (1986) a formula of the EMEP-model is used (Thehos, 1991; Sandnes and Styve, 1993).

$$\ln K = \ln K_s - \frac{20.75 + \ln K_s}{101 - r} - \left(\frac{r - r_d}{101 - r_d}\right) \tag{4.6}$$

with r = relative humidity and r_d = relative humidity at deliquescence

$$\ln r_d = \frac{723.7}{T} - 1.7037 \tag{4.7}$$

The concentration of ammonium nitrate can be determined by the use two of conservation equations

$$\begin{aligned} [NH_3]_{(eq)} + [NH_4NO_3]_{(eq)} &= [NH_3]_{(neq)} + [NH_4NO_3]_{(neq)} \\ [HNO_3]_{(eq)} + [NH_4NO_3]_{(eq)} &= [HNO_3]_{(neq)} + [NH_4NO_3]_{(neq)} \\ [NH_3]_{(eq)} \cdot [HNO_3]_{(eq)} &= K \end{aligned} \tag{4.8}$$

where (eq) means the equilibrium concentration and (neq) the non-equilibrium concentration. Now the equilibrium concentrations can be calculated as

$$\begin{aligned} [NH_3]_{(eq)} &= \frac{[NH_3]_{(neq)} - [HNO_3]_{(neq)}}{2} + \sqrt{\left(\frac{[NH_3]_{(neq)} - [HNO_3]_{(neq)}}{2}\right)^2 + K} \\ [HNO_3]_{(eq)} &= \frac{K}{[NH_3]_{(eq)}} \\ [NO_3]_{(eq)} &= [NH_4NO_3]_{(eq)} + [NH_3]_{(neq)} - [NH_3]_{(eq)} \end{aligned} \tag{4.9}$$

Ammonium nitrate is formed for

$$[NH_3]_{(neq)} \cdot [HNO_3]_{(neq)} > K \tag{4.10}$$

and decomposed for

$$[NH_3]_{(neq)} \cdot [HNO_3]_{(neq)} < K \tag{4.11}$$

The calculation of ammonium nitrate and -sulfate depends on the gas-phase reaction system. It can be used with both EMEP and CHEMSAN provided that NH_3 is emitted.

4.2 Parameterization of dry deposition

In METRAS the dry deposition flux F of a species towards a unit surface area is computed by multiplication of the deposition velocity V_D with the pollutant concentration $C(z_1)$ at a reference height z_1 (=10 m) close to the ground (Chamberlain, 1975):

$$F = V_D \cdot \bar{C}(z_1) \tag{4.12}$$

The calculation of the deposition velocity V_D is based on a resistance model, which means that V_D is calculated as a reciprocal value of the sum of three characteristic resistances (e.g. Chang et al., 1987):

$$V_D = (r_a + r_m + r_s)^{-1} \tag{4.13}$$

The intensity of turbulent mixing in the surface layer controls the aerodynamic resistance r_a. The following parameterization, used for instance also by Sheih et al. (1979), has been employed:

$$r_a = \frac{ln(z_1 / z_0) - \psi_h}{u_* \kappa} \tag{4.14}$$

Here it is assumed that the turbulent transport of pollutants is similar to the transport of heat in the surface layer (e.g. Pielke, 1984) and the stability function ψ_h is calculated according to Dyer (1974) as given in Section 3.3, but taken as ψ_h for $-0.01 \le z/L \le 0.01$.

For parameterization of the sublayer resistance r_m different formulas are used for the 10 different land-use types considered in the model. Over a water surface the formula discussed by Brutsaert (1975) and Garrat and Hicks (1973) are used:

$$r_m = \begin{cases} (u_*)^{-1} \cdot (13.6 \cdot Sc^{2/3} - 13.5) & \text{for} \quad Re < 1 \qquad \text{(a)} \\ (u_* \cdot \kappa)^{-1} \cdot \ln\left[\dfrac{u_* \kappa z_0}{D_c}\right] & \text{for} \quad Re \ge 1 \qquad \text{(b)} \end{cases} \tag{4.15}$$

with D_c the molecular diffusivity of the trace gas in air, $Sc = \nu / D_c$ the Schmidt number and Re the turbulent Reynolds number. Due to investigations performed by Garrat and Hicks (1973) r_m is calculated over vegetation by (Wesely and Hicks, 1977):

$$r_m = (u_* \kappa)^{-1} \cdot 2 \cdot Sc^{2/3} \tag{4.16}$$

Over urban land types (bluff bodies) the formula pointed out by Brutsaert (1975) is applied:

$$r_m = u_*^{-1} \cdot (7.3 \cdot Re^{1/4} \cdot Sc^{1/2} - 5) \tag{4.17}$$

The surface resistance r_s depends on the stomata, cuticular and mesophyll resistances, and on the solubility or reactivity of a given trace gas (Walcek et al., 1986). For surfaces covered by vegetation the surface resistance is a function of season and insulation, and their influence on the stomata activity of the vegetation. Following Arritt et al. (1988), r_s is assumed to depend on the land-use type. The influence of insulation and relative humidity at the surface q_{rs} on the surface resistance r_s is included in the following way:

$$r_s = \begin{cases} r_{s,wet} & \text{for } q_{rs} > 99.9\% & & & \text{(a)} \\ r_{s,max} & \text{for } q_{rs} < 99.9\% & \text{and} & R_{SW} = 0\ \mathrm{Wm}^{-2} & \text{(b)} \\ r_{s,min} + (r_{s,max} - r_{s,min}) \cdot [1-(R_{SW}/400)^{1/3}] & \text{for } q_{rs} < 99.9\% & \text{and} & 0 < R_{SW} < 400\ \mathrm{Wm}^{-2} & \text{(c)} \\ r_{s,min} & \text{for } q_{rs} < 99.9\% & \text{and} & R_{SW} \geq 400\ \mathrm{Wm}^{-2} & \text{(d)} \end{cases} \quad (4.18$$

The solar irradiation R_{SW} is calculated in the model METRAS as described in Section 3.6. For the values of $r_{s,wet}, r_{s,min}$, and $r_{s,max}$ used in METRAS see Section 7.1 in Schlünzen et al. (2018).

In METRAS the concept of the resistance model is also applied to some aerosols (SO_4^{2-}, NO_3^-, Pb). The surface resistance r_s for aerosols smaller than $10\,\mu m$ is about zero, the deposition only depends on the molecular resistance and the size of the aerosols. For aerosols larger than 0.2 μm the deposition velocity increases with increasing diameter of the particle.

SO_4^{2-} and NO_3^- ions are transported on other larger particles. The mass size of the particles bearing SO_4^{2-} or NO_3^- varies with source, season, region and humidity. In general, SO_4^{2-} is dispersed in the $0.1-1.0\,\mu m$ diameter range and nitrates are bimodally dispersed with one mode in the $0.1-1.0\,\mu m$ range and the other in the $2.0-10.0\,\mu m$ range (Voldner et al., 1986). Since large particles have higher deposition velocities, r_b for NO_3^- is more or less arbitrarily chosen as 50% of that for SO_4^{2-}. The time dependency of r_b for aerosols is solved in the same way as r_s for gaseous substances. Further details on the dry deposition module of METRAS are given in Pahl (1990), Pahl and Schlünzen (1990) and Schlünzen and Pahl (1992).

4.3 Parameterization of wet deposition

In METRAS the rate of removal of gases and particles by wet deposition is represented as a first order process and can be parameterized, therefore, by $\Lambda_p(d_p,x,y,z,t)\cdot\overline{C}(x,y,z,t)$ and $\Lambda_p(d_p,x,y,z,t)\cdot n(d_p,x,y,z,t)$ (e.g. Seinfeld, 1986). $\overline{C}$ is the gaseous concentration in air, n the particle size distribution function and Λ and Λ_p the gaseous and particulate washout coefficients, respectively, each one dependent on location and time. The assumption of a first order process is valid if the scavenging is more or less irreversible. In contrast to particle scavenging this assumption fails for some gases with reversible solubility. In METRAS, however, only the scavenging and wet deposition of irreversible soluble gases is implemented.

With the further assumption that all scavenged material reaches the surface, the wet flux to the surface can be written

$$D^{wet}(x,y,t) = \int_o^{z_t} \Lambda(x,y,z,t) \cdot \overline{C}(x,y,z,t) dz \tag{4.19}$$

$$D_p^{wet}(d_p,x,y,t) = \int_0^{z_t} \Lambda_p(d_p,x,y,z,t) \cdot n(d_p,x,y,z,t)\, dz \tag{4.20}$$

It should be stressed here that the concept of a washout coefficient $\Lambda(x,y,z,t)$ differs from the often used concept of a washout ratio

$$W_r = \frac{\text{concentration in precipitation}}{\text{concentration in air near surface}}$$

which ignores vertical inhomogeneities in concentration and precipitation. Although the relations (4.19) and (4.20) are a considerable progress in taking into account vertical inhomogeneities, their weakness lies in the fact that all once scavenged material is deposed at the surface immediately. The release of scavenged material by evaporation of rain drops in subsaturated layers is ignored. The difference form of (4.19) in the model METRAS is given by

$$\Delta D_{i,j}^{wet} = \sum_{k=1}^{NX3} \Lambda_{i,j,k} \cdot \rho_{0_{i,j,k}} \cdot \overline{C}_{i,j,k} \cdot \Delta z_{i,j,k} \cdot \Delta t \tag{4.21}$$

where $\Delta D_{i,j}^{wet}$ denotes the flux of wet deposition [kg m^{-2} s^{-1}] to the surface during one time step of length Δt. Indices i, j, k denote grid points in x-, y- and z-direction, respectively. In (4.21) compared with (4.19) the density ρ_0 has been added due to the fact that in METRAS concentration units are given in [kg/kg]. Since scavenging removes material from the gaseous phase the change in concentration per time step is computed by

$$\Delta C_{i,j,k} = -\Lambda_{i,j,k} \cdot \overline{C}_{i,j,k} \cdot \Delta t \tag{4.22}$$

According to Tremblay and Leighton (1986) the washout coefficients depend on the local rainfall rate $R_{i,j,k}$ by

$$\Lambda_{i,j,k}^{s} = a_s + b_s \cdot (R_{i,j,k})^{c_s} \tag{4.23}$$

where s refers to the pollutant species under consideration. The values of a_s, b_s and c_s implemented in METRAS for several species are listed in Section 7.2 of Schlünzen et al. (2018). The local rainfall rate is a function of rain water content and terminal velocity and has to be given in [mm·h^{-1}] :

$$R_{i,j,k} = 3600 \cdot 10^3 \cdot [(\rho(\rho_w) \cdot q_1^{2r} \cdot V_{TR}]_{i,j,k} \tag{4.24}$$

With V_{TR} from equation (3.70).

4.4 Parameterization of ship emissions

Ship emissions are parameterized in METRAS depending on ship type and engine type. Fuel consumption is estimated by Trozzi and Vaccaro (1998) for several ship types depending on their net tonnage using linear regressions. Trozzi and Vaccaro (1998) also

give emission factors for nitrous oxides NO_X, carbon monoxide CO, volatile organic compounds VOC and particulate matter PM_{10} depending on the engine type. For the mapping of these species groups to METRAS-known species a volume fraction NO_2/NO_X of 5% is assumed, which corresponds of a mass fraction of 7.47%. For VOCs no mapping to METRAS species is known, for PM_{10} Bond et al. (2004) uses a mass fraction soot/PM_{10} of 56.7% to estimate the global soot emissions from ships. Further details on the implementation are given by Spensberger (2010).

4.5 Parameterization of aircraft emissions

Similar to ships, emissions by aircraft are calculated from the fuel consumption of an aircraft type and the emission factors for several species dependent on the engine used. Following the ICAO touch-down to take-off cycle which defines the flight states (1) approach flight and take-down, (2) taxiing, (3) take-off and (4) climb-out Uphoff (2008) collected these data for several aircraft and several engines. The fuel flow during the flight states is assumed to be 30%, 7%, 100% and 85% of its maximum (Uphoff, 2008). The time spans that an aircraft typically spends in each flight state are also calculated by Uphoff (2008) from its aerodynamical properties. The maximum height to which aircraft emissions are calculated is 915 m (3000 ft).

5 Treatment of obstcales

5.1 Buildings

For treating buildings in the obstacle resolving model MITRAS in the 3-D model, the concept of the mask method (Briscolini and Santangelo, 1989) is employed in MITRAS. This method is based on the immersed boundary method (e.g., Mittal and Iaccarino 2005), which allows flow simulation in the vicinity of complex geometries that do not conform on Cartesian grids. Impermeable grid cells are defined at the buildings positions using 3-D fields of weighting factors, *vol(x,y,z)*, that are defined at each grid cell. The weighting factors include the information whether a grid cell is in the atmosphere cell or in a building. The last can be completely or mostly inside a building. Any faces of a grid volume that include a building and are a wall or roof are marked using additional arrays denoting the different faces. This means that the grid cells in a domain are divided into three groups: grid cells in the free atmosphere that are surrounded by atmosphere and have no adjacent building, grid cells next to building surfaces, and grid cells within buildings (Figure 5.1). This destinction of the different grid cell qualities is used in the model coding. The mask method economizes the computation, since the equations can be timedependently solved throughout the whole 3D arrays. The masking data are prepared by the preprocessor GRIMASK (Section 3.2.6 of Schlünzen et al., 2018). In the model, e.g. the wind velocity components vanish at the building boundaries by multiplying the fluxes at the grid volume faces with the face markers (impermeable walls). Wall functions are additionally included to address friction effects properly.

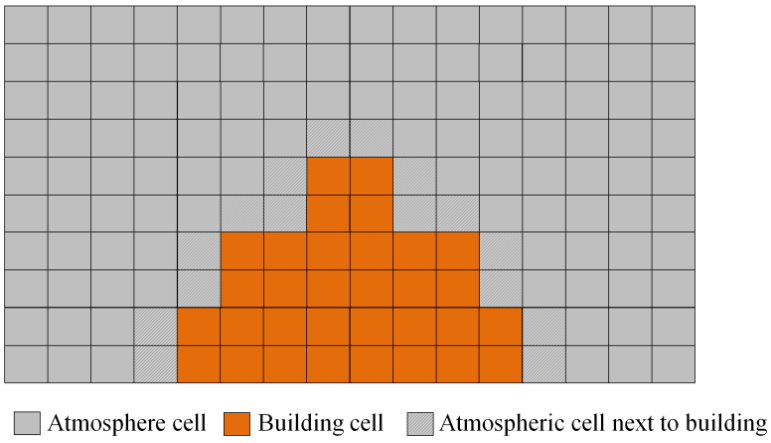

Figure 5.1: Masking concept in MITRAS.

The aair temperature is influenced by changes of the surface temperature at building surfaces. Their effect is taken into account by simulating the sensible heat flux. In grid cells

that are adjacent to building surfaces, the term Q_θ is added to the turbulent fluxes of heat (Eq. (*5.3*)).

$$Q_\theta = -u_{b^*}\theta_{b^*} \tag{5.1}$$

Q_θ represents the sensible heat flux, which is calculated from the friction velocity at buildings, u_{b^*}, and the scaling value for potential temperature, θ_{b^*}. u_{b^*} is calculated following the approach of Lopez (2002) as

$$u_{b^*} = \kappa \frac{|\vec{v}_b|}{ln\left(\frac{d_b}{z_{b,0}}\right)} \tag{5.2}$$

A logarithmic wind profile with neutral stratification is assumed normal to each of the building surfaces. $|\vec{v}_b|$ is the wind speed parallel to the building surface at the first scalar grid cell next to the building surface, i.e. in the distance d_b, whith its value depending on the grid size. Typical values for d_b are thus several decameters to very few meters. $z_{b,0}$ is the roughness length of the building surface. The scaling value for potential temperature at buildings' surfaces is calculated as

$$\theta_{b^*} = \kappa \frac{(\overline{\theta_{d,b}} - \theta_b)}{ln\left(\frac{d_b}{z_{b,0,\theta}}\right)} \tag{5.3}$$

and thus depends on the difference of the building surface temperature, θ_b, and the air temperature at the first grid cell next to the building, $\theta_{d,b}$. The roughness length for temperature at the building ($z_{b,0,\theta}$) depends on the roughness Reynolds number, *Re*. Following Brutsaert (1975). The roughness length ratio is calculated as:

$$\frac{z_{b,0}}{z_{b,0,\theta}} = exp\left(k\left(7.3Re^{1/4}\sqrt{Pr} - 5\right)\right) \tag{5.4}$$

with the Prandtl number (*Pr*) set to 0.71.

This concept allows considering not only surface-mounted buildings but also overhanging obstacles such as bridges and overpasses or pathways to courtyards. They can all be considered in complex urban geometries.

5.2 Building surface temperature

In order to obtain an accurate surface temperature of the buildings (obstacles), T_b, a number of surface fluxes are considered at the building surfaces in MITRAS, including turbulent and radiative processes (Gierisch 2011). Thus, the physical properties of the façade

and walls' materials are needed in the model, including reflectivity, emissivity, heat transfer coefficient, and specific heat capacity of the walls.

The surface temperature of a building surface, T_b, is calculated from the energy budget assuming an infinitely thin outermost slab of the building façade. The slab is heated or cooled from outside by a heat source, *H,* and supported from inside by the rest of the façade that is connected to the building interior. The latter is assumed to be maintained at a constant temperature, T_{in}. The rate of temperature change of the slab is governed by the imbalance between the forcing term *H* and a restoring term:

$$c_{wall} D \frac{\partial T_b}{\partial t} = H - \frac{\lambda}{D}(T_b - T_{in}). \quad (5.5)$$

The forcing term *H* is calculated from

$$H = R_{SW,abs} + R_{LW,abs} - \varepsilon\sigma T_b^4 + Q_S + Q_L. \quad (5.6)$$

$R_{SW,abs}$ and $R_{LW,abs}$ denote the absorbed incoming short wave and long wave radiation, respectively. Q_S and Q_L are the sensible and latent heat fluxes at the surface, respectively. These are calculated from the local friction velocity and the local scaling values for temperature and humidity using eq. (*5.1*) (Gierisch 2011). λ is the thermal conductivity, *D* is the wall thickness, and c_{wall} is the wall volumetric heat capacity.

The surface energy balance for the inside of the wall surface can be written as

$$Q_C - h_i(T_{in} - T_{room}) = 0. \quad (5.7)$$

h_i is the heat transfer coefficient for the internal wall, and Q_C the heat conduction flux through the wall calculated as $Q_C = \lambda/D\,(T_b - T_{in})$ and T_{room} is the room temperature. Using eq. (*5.7*), the relation between T_{in} and T_b results in

$$T_{in} = \frac{h_i}{h_i + \frac{\lambda}{D}} T_{room} + \frac{\frac{\lambda}{D}}{h_i + \frac{\lambda}{D}} T_b \quad (5.8)$$

Substituting *H* and T_{in} in Eq. (*5.5*) yields,

$$\frac{\partial T_b}{\partial t} = \frac{1}{c_{wall} D}[H - C(T_b - T_{room})] \quad (5.9)$$

The right-hand side of eq. (*5.6*) is a function of T_b. Thus

$$\frac{\partial T_b}{\partial t} = F(T_b) \tag{5.10}$$

Solving eq. (5.10) numerically,

$$F(T_b^{t+\Delta t}) = F(T_b^t) + \left.\frac{\partial F}{\partial T_b}\right|_{T_b^t} (T_b^{t+\Delta t} - T_b^t) \tag{5.11}$$

and rewriting eq. (5.11) for $T_b^{t+\Delta t}$ gives the time dependent equation for the surface temperature:

$$T_b^{t+\Delta t} = T_b^t + \frac{F(T_b^t)}{\frac{1}{\Delta t} - \left.\frac{\partial F}{\partial T_b}\right|_{T_b^t}} \tag{5.12}$$

5.3 Wind turbines

As other solid obstacles the tower and the nacelle of a wind turbine are represented in MITRAS by impermeable grid cells, therby assuring for example a vanishing wind speed and zero turbulent kinetic energy at grid points within the tower and nacelle. The orientation of the nacelle changes time dependent in relation to the incoming wind direction in the model simulation. The wind turbine rotor is parameterized by using the actuator-disk concept (Molly 1978; Mikkelsen 2003; El Kasmi and Masson 2008). In this concept the rotor is replaced by an im aginary permeable disk subjected to a distribution of forces which acts upon the incoming flow at a rate defined by the period-averaged kinetic energy that the rotor extracts from the atmosphere. According to the actuator-disk model, the reduction of the wind speed is caused by the rotor thrust, T, which is formulated as.

$$T = \frac{1}{2} c_T \rho A V_1^2. \tag{5.13}$$

V_1 denotes the speed of the approaching flow at wind turbine level, A is the rotor area, ρ is the air density, and c_T is the non-dimensional thrust coefficient for the corresponding wind speed. The energy removal is limited to those cells located at the actual rotor position. The speed of the approaching flow is calculated with respect to the orientation of the rotor which depends on wind direction and changes direction during the simulation. The thrust coefficient T depends on wind speed and therefore wind turbines in MITRAS automatically switches on at the cut-in and automatically off at the cut-off wind speed.

The wind turbine rotor blade creates wake vortices of the wind turbines, which are associated with increased turbulence intensity. The turbulence generation in the wake is parameterized in MITRAS by adding an additional term, Q_{wt}, to the turbulence mechanical production, P_M, in the turbulent kinetic energy equation to account for the turbulence generation at the rotor position. This term is formulated in dependence of the scale velocity u_{wt} used to characterize the turbulence as:

$$Q_{wt}=\frac{1}{2}c_{wt}u_{wt}^{2} \qquad (5.14)$$

The factor c_{wt} [s^{-1}] includes the wind turbine characteristics that govern the amount of produced turbulence, namely the rotor size, the number of blades and the rotational speed

The rotation of the rotor induces a tangential velocity, v_θ. In MITRAS we use the scale velocity that is typically used to parameterise a vortex developing behind an aircraft. The Rankine vortex model (Gerz et al. 2001) is applied here to calculate v_θ:

$$v_\theta=\frac{\Gamma_O}{2\pi r_c} \qquad (5.15)$$

r_c is the vortex core radius and Γ_O is the rotor circulation, which is related to the rotor rotational speed, lift coefficient, and aspect ratio. More details about modelling the wind turbines in MITRAS are given in Linde (2011).

5.4 Vegetation

Two modes of vegetation treatment are used in MITRAS. In the implicit mode, the effect of the vegetation (grass, bushes, trees, etc.) is implicitly considered in the surface parameterization, using the roughness length. This is done in the same way as in the mesoscale model METRAS (Section 3.3) by allocating the vegetation surface cover class for the corresponding surface grid cells and using the corresponding input parameters (e.g. roughness length, soil water content etc.; Section 3.2.6 of Schlünzen et al., 2018).

In the explicit mode, the vegetation effects are explicitly resolved. These effects include the wind speed reduction (Schlüter 2006), turbulence dissipation due to drag forces from plant foliage-atmosphere interaction (Salim et al. 2015), and radiation absorption and shading.

The wind speed reduction is parameterized by introducing a local three-dimensional sink term, S_{u_i} with *i=1, 2, 3* for the *u-, v, w-* component. S_{u_i} is added to the momentum equations (*2.23*). Following Liu (1996), the sink term is calculated as:

$$S_{u_i} = - c_d \, LAD(\dot{x}^3) \cdot U \cdot u_i \qquad (5.16)$$

Here c_d is a drag coefficient, U is the mean wind speed at height $\dot{x}^3$, and $LAD(\dot{x}^3)$ is the equivalent leaf area density of the plant at height $\dot{x}^3$. The value of c_d = 0.2 determined by Katul (1998) is chosen here. S_{u_i} represents a source of turbulence resulting from the extraction of mean kinetic energy, E, from the flow. However, the typical effect of vegetation is to reduce the overall turbulence by enhancing the dissipation of turbulence. To parameterize the additional turbulence creation and dissipation, additional source terms are added to the turbulent kinetic energy and dissipation equations. Following Wilson (1988) and Liu et al. (1996) these terms read:

$$Q_{veg,E} = c_d LAD(\dot{x}^3) \cdot U^3 - 4 c_d LAD(\dot{x}^3) \cdot |U| \cdot E \qquad (5.17)$$

$$Q_{veg,\epsilon} = 1.5 c_d LAD(\dot{x}^3) \cdot U^3 - 6 c_d LAD(\dot{x}^3) \cdot |U| \cdot \epsilon \qquad (5.18)$$

The reduction of the shortwave radiation flux is considered by including a hight dependent local reduction coefficients (ranging from 1 to 0. The reduction coefficients depend on the height dependent leaf area index, *LAI*, of the plant (see Section 3.5.3 of Schlünzen et al. (2018))

$$\sigma_{SW}(\dot{x}^3) = exp\left(F \cdot LAI(\dot{x}^3)\right) \qquad (5.19)$$

6 Numerical treatment

In this chapter the numerical schemes used for solving the discretized model equations as well as the used grid and the initialization of the model are presented. The discretized model equations are summarized in Appendix B.

6.1 Non-uniform grid

The model equations are spatially discretized on an ARAKAWA-C-grid, which represents gravity waves better than other grids (Mesinger and Arakawa, 1976).

From Figure 5.1 it can be seen that the components of the velocity vector are defined at grid points which are separated in all directions from the grid points for scalar variables. This increases the accuracy of the used numerical methods for the computation of divergences. Some of the transformation coefficients A to G, used to discretize the equations (Appendix A), are defined at scalar grid points, others are defined at vectorial grid points.

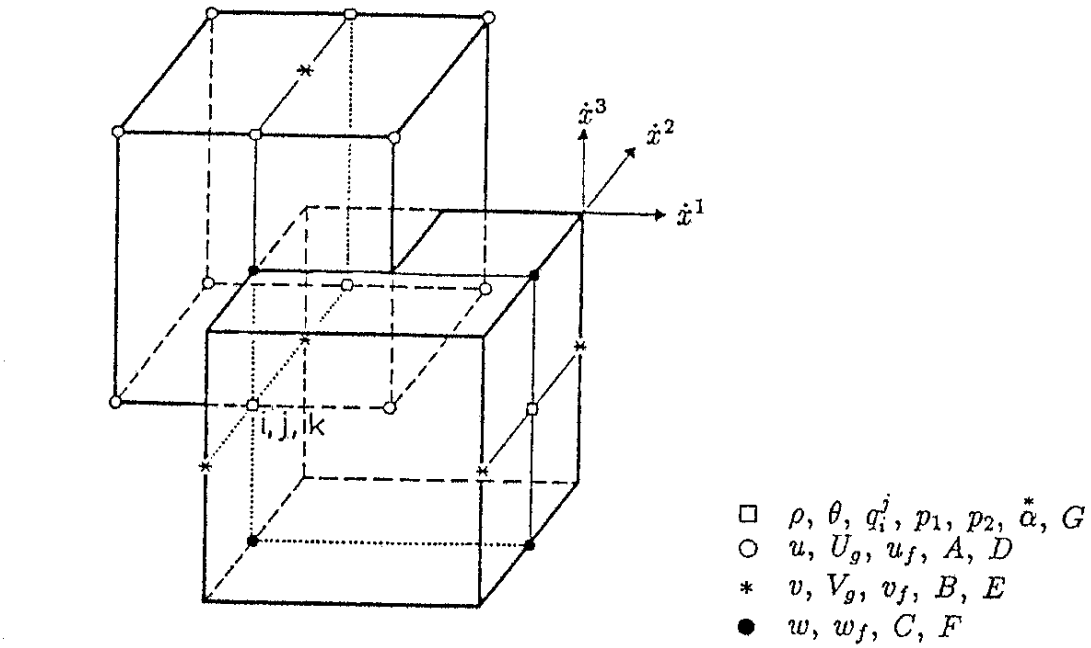

Figure 6.1: Three-dimensional grid representation in METRAS/MITRAS (ARAKAWA - C)

Figure 5.2 shows a projection of scalar and vectorial grid points to the horizontal $\dot{x}^1, \dot{x}^2$ plane (left) and the vertical $\dot{x}^1, \dot{x}^3$ plane (right). The lateral boundaries of the model area are defined at $i = j = 0.5$, corresponding to the index 0 of the vector field, and $i = NX1 + 0.5$, $j = NX2 + 0.5$, corresponding to the index NX1 and NX2 of the vector field. The surface lies at $k = 0.5$ and the top boundary at $k = NX3 + 0.5$ The velocity components are defined

at the boundaries with respect to the direction they represent (U at $\dot{x}^1$-boundaries, V at $\dot{x}^2$-boundaries, W at $\dot{x}^3$-boundaries), whereas the boundary values of scalar variables are defined at half a grid width outside of the model area. The same holds for velocity components in those directions, where they are defined at scalar grid points. This grid representation enables the coupling of velocity and pressure arrays at the boundaries (Section 7.3). Figure 5.3 shows the grid representation for a non-uniform grid.

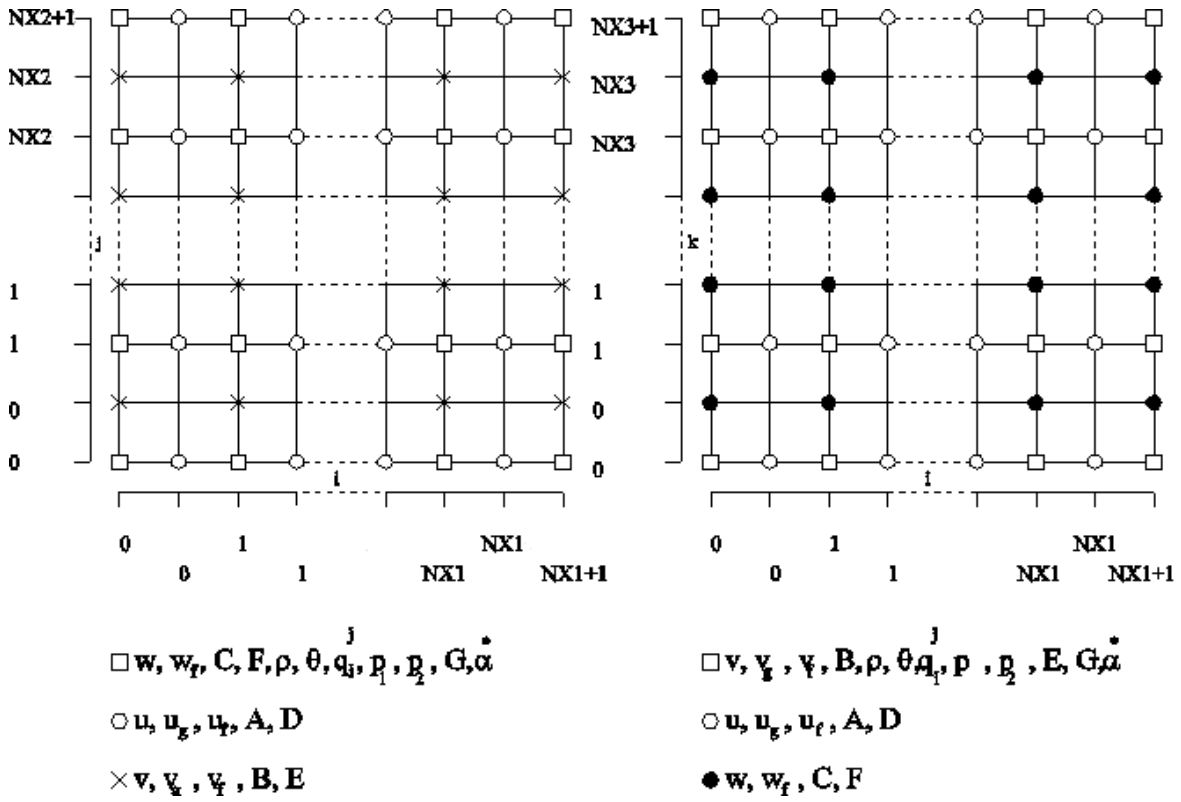

Figure 6.2: Grid representation in a $\dot{x}^1, \dot{x}^2$ plane (left) and $\dot{x}^1, \dot{x}^3$ plane (right)

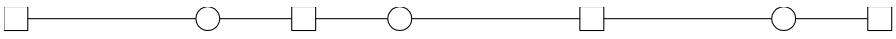

□ $v, v_g, v_f, B, w, w_f, C, F, \rho, \theta, q_i, p_1, p_2, E, G, \alpha^*$

○ u, u_g, u_f, A, D

Figure 6.3: Grid representation in $\dot{x}^1$-direction displaying the position of different grid points in a nonuniform grid

The model equations are solved in a uniform grid (Appendix A.2) with uniform grid increments $\Delta\dot{x}^1 = \Delta\dot{x}^2 = \Delta\dot{x}^3 = 1$ ($\Delta\dot{x}^1, \Delta\dot{x}^2, \Delta\dot{x}^3$ without unit). The coordinates of scalar grid points in the coordinate system $\dot{X}$ are defined as follows:

$\dot{x}^1 = i$ with $i = 0,1,\ldots$ NX1 + 1, resulting in NX1+2 grid points

$\dot{x}^2 = j$ with $j = 0,1,\ldots$ NX2 + 1, resulting in NX1+2 grid points

$\dot{x}^3 = k$ with $k = 0,1,\ldots$ NX3 + 1, resulting in NX1+2 grid points

The vectorial grid points are defined in a similar way. It follows that there are $NX1+1$ vectorial u-points in direction $\dot{x}^1$, $NX2+1$ vectorial v-points in direction $\dot{x}^2$ and $NX3+1$ vectorial w-points in direction $\dot{x}^3$.

6.2 Temporal integration scheme of the model

The solving of the model equations follows the temporal integration scheme given in Table 2. Details of the integration are given in Chapter 8 of Schlünzen et al. (2018).

Model Initialization	
Time Integration Loop	
	Calculation of Corresponding Time
	If specified: Topography 'Diastrophy'
	Calculation of exchange coefficients and surface characteristics
	Calculation of Wind Field, Pressure p_2
	If specified: Calculation of Scalar Quantities ($\tilde{\theta}, \tilde{q}_1^2, \tilde{C}_j$)
	Calculation of Density $\tilde{\rho}$
	Calculation of Pressure p_1
	If Specified: OUTPUT of Selected Values
End of Simulation	

Table 2: Integration scheme of model METRAS

After specifying initial values for all variables the integration within the time loop starts with the computation of new surface heights, if necessary (diastrophism). As a next step the friction velocity u_*, flux temperature θ_* and flux humidity q_* are determined by iteration. Now the exchange coefficients can be derived and the wind components and pressure p_2 are computed for the new time step. With the new dynamic fields the equations for the scalar variables temperature, humidity, liquid water and pollutants can be solved in a semi-implicit manner. Finally the density $\tilde{\rho}$ and pressure p_1 are derived from diagnostic equations.

Without using the new dynamic fields for solving the equations of temperature and humidity it would be necessary to adapt the time step to the velocity of gravity waves which can reach 300 m s^{-1}. The use of huge amounts of computation time can be avoided by using the semi-implicit integration scheme (Pielke, 1984). The balance equations of liquid water and pollutants are also solved semi-implicit, which is not necessary but reduces memory resources because no additional auxiliary arrays for preliminary velocity fields are required.

6.3 Numerical schemes

The numerical schemes implemented in METRAS have been chosen with regard to the requirements that they

- require a minimum of computer memory
- can easily be vectorized for optimization
- supply convergent and stable solutions and
- have low numerical diffusion.

Due to nonlinear instability of the model equations the solutions can be disturbed by the formation of $2\Delta x$-waves (Haltiner and Williams, 1980). To avoid such instabilities, three kinds of filters are implemented in METRAS to damp $2\Delta x$-waves (Shapiro, 1971).

Level 1 (3 point):

$$\ddot{\psi}_i = \frac{1}{4} \cdot \left(\psi_{i+1} + 2 \cdot \psi_i + \psi_{i-1}\right) \tag{6.1}$$

Level 2 (5 point):

$$\ddot{\psi}_i = \frac{1}{16}\left(-\psi_{1+2} + 4\psi_{i+1} + 10\psi_i + 4\psi_{i-1} - \psi_{i-2}\right) \tag{6.2}$$

Level 3 (7 point):

$$\ddot{\psi}_i = \frac{1}{64}\left(\psi_{i+3} - 6\psi_{i+2} + 15\psi_{i+1} + 44\psi_i + 15\psi_{i-1} - 6\psi_{i-2} + \psi_{i-3}\right) \tag{6.3}$$

ψ represents unfiltered values and $\ddot{\psi}$ filtered values. Boundary values remain unfiltered. In most model runs the 7 point filter (6.3) is applied, resulting in low damping.

When using higher level filters the values close to boundaries are calculated with the lower level filters. The filters are only used in horizontal direction, at first in x- and at second in y-direction. For radiational heating and cooling, calculated as described in Section 3.6, the

filter (6.1) is used in vertical direction. This considers implicitly intense vertical mixing processes occurring in clouds.

6.3.1 Solution of the equation of motion

The discretized equations for momentum are listed in Appendix B.1.1. For the temporal integration of the advection terms the Adam-Bashforth scheme is used, with the spatial derivatives approximated by centered differences. This scheme is slightly instable, but the typical computational mode of 3-level-schemes is damped (Mesinger and Arakawa, 1976). Following Schumann (1983), this scheme is stable for solving the equations of motion, if, as it is done in METRAS, the diffusion terms are also calculated with this scheme. To increase the time step for vertical exchange processes an implicit scheme (Crank Nicholson) is implemented to derive vertical diffusion terms.

The Coriolis and gravity terms of the equation of motion are discretized forward-in-time and centered-in-space. Although forward-in-time differences of the Coriolis terms may lead to instabilities (e.g. Kapitza, 1987), this method can be used due to the very small amplifying of the solution, when time steps shorter than 100 s are used (Pielke, 1984). In METRAS time steps are limited to 60 s.

The gradients of the pressure p_2 are solved implicit with backward differences. By doing so the anelastic assumption (2.15) is achieved at every time. The pressure gradients are discretized centered-in-space, as is done with all other gradients not mentioned here. All variables which are not defined at the grid points where they are used, are taken as an average from the neighboring grid points.

6.3.2 Solution of scalar equations

The discretized balance equations for scalar quantities are given in Appendix B.1.2. The advection terms are discretized by the well known upstream scheme. The exchange processes can be solved forward-in-time and centered-in-space or, alternatively, for the vertical direction with the Crank-Nicholson-scheme.

6.3.3 Solution of the Poisson equation

The pressure p_1 can be subsequently computed by numerical integration of (2.19) from the upper model boundary to the ground. The density deviation $\tilde{\rho}$ is derived from the diagnostic equations (2.20) as a function of the temperature deviation $\tilde{\theta}$ and the pressure $\tilde{p} = p_1 + p_2$. Since the pressure p_1 at time step $n+1$ is unknown (Table 2), the known value at time step n is used. However, for the temperature and pressure p_2 the values at time step $n+1$ are used. The density $\tilde{\rho}(k,j,i)$, therefore, is derived semi-implicit. Addition-

al boundary values are only necessary for p_1 at the upper boundary, where $p_1 = 0$ is assumed and all pressure deviations are summarized in the pressure p_2

Equation (2.25) for the pressure p_2 is an elliptic differential equation (Posson equation), with Neumann boundary conditions. Since Neumann boundary conditions imply a singular discretization matrix (constant pressure functions are contained in the kernel of the Laplace-operator), the solution is scaled by the mean pressure at the top of simulation domain.

Furthermore, the discretized system needs to be solved by an iterative procedure - for the reason of singularity and its size. Within the model METRAS the iterative IGCG-scheme (Idealized Generalized Conjugate Gradient; Kapitza and Eppel, 1987) and the preconditioned BiCGStab-method (BiConjugate Gradient Stabilized; Van der Vorst, 1992) are implemented. More details about the solution procedure for the poisson equation can be found in Schröder (2007). An OpenMP based parallelization of the BiCGstab solver (and also an additional GMRES solver) with block preconditioners or multicoloring decomposition are currently under development.

6.3.4 Numerical solution of gas-phase reactions

The temporal change of a concentration is the sum of the sources and sinks,

$$\frac{dC_i(t)}{dt} = R_i(c,t) + Q_i(t) \quad i = 1,..N \tag{6.4}$$

which depends on the chemical reactions (R_i), emission and deposition (Q_i). Including only the chemical reactions, equation (6.4) changes to

$$\frac{dC_i(t)}{dt} = P_i(C(t)) + L_i(C(t)) \tag{6.5}$$

with P_i = production rate and L_i = lost rate of the species i. Assuming that P_i and L_i are constant during the time interval $(t_n, t_n + \Delta t_n)$, the solution of equation (6.5) is

$$C_i(t_n + \Delta t_n) = \frac{P_i(C(t_n))}{L_i(C(t_n))} + (C_i(t_n) - \frac{P_i(C(t_n))}{L_i(C(t_n))} \cdot e^{-\Delta t_n L_i(C(t_n))} \tag{6.6}$$

A chemical gas phase system is a nonlinear, stiff differential system. The large differences in the eigenvalues due to large differences in the lifetime of species cause the stiffness of the system. To solve a stiff ordinary differential equation system, special numerical algorithms have to be chosen. In METRAS an explicit algorithm is included based on QSSA. This algorithm chooses different equations for species with different lifetime, which makes the algorithm very time consuming. To improve the algorithm, Knoth and Wolke (1993) replaced the exponential term of equation (6.6) by the Padé-approximation

$$-\Delta t \cdot L_i(c(t_n)) = \frac{1}{1+\Delta t \cdot L_i(C(t)) + \frac{1}{2}(\Delta t \cdot L_i(C(t)))^2} \tag{6.7}$$

Substituting equation (6.7) in equation (6.6) results in

$$C_i(t_n + \Delta t_n) = \frac{\Delta t_n P_i^n (1+\frac{1}{2}\Delta t \cdot L_i^n) + C_i^n}{1+\Delta t_n \cdot L_i^n + \frac{1}{2}(\Delta t \cdot L_i^n)^2} \tag{6.8}$$

7 Boundary conditions

The model area is limited in vertical and horizontal directions. Over land the surface height z_s and over water the water surface coincides with the lower model boundary. The remaining five boundaries are artificial in the sense that they do not correspond to natural boundaries between two media. Since they are artificial, the corresponding boundary conditions have to be formulated in such a way that waves can pass these boundaries without reflections.

In METRAS/MITRAS several boundary conditions are implemented at each boundary, because different applications require different boundary conditions. They can be selected by control variables in the model input and are based on the following assumptions:

- Lateral boundaries can be inflow and outflow boundaries at the same time.
- Boundary values of the wind components $\overline{\dot{u}^1}$, $\overline{\dot{u}^2}$, $\overline{\dot{u}^3}$ normal to the boundary are coupled to the pressure deviation p_2. The derivation of the boundary conditions takes this relation into account, as is done in other mesoscale models (Clark, 1977; Schumann and Volkert, 1984).
- The increments Δx, Δy remain constant at the first three scalar grid points, including the scalar grid points outside the lateral boundaries. Thus the derivatives $\partial \dot{x}^1/\partial x$ at the west/east boundaries and $\partial \dot{x}^2/\partial y$ at the south/north boundaries remain constant at two grid points.
- The increment Δz remains constant at the lowest and highest three scalar grid points, including the scalar grid point below the surface and above the model top. Thus the derivative $\partial \dot{x}^3/\partial z$ remains constant at two vector grid points.
- The surface heights z_s remain constant normal to the boundaries for three scalar grid points, which yields $\partial \dot{x}^3/\partial x = 0$ and $\partial \dot{x}^3/\partial y = 0$ at the corresponding boundaries.

These five assumptions do not limit the range of applicability of the model. Within checked limits (Schlünzen (1988), Section 5.1) the grid increments can be chosen without declining the solvability of the equation system. The grid increments can be chosen depending on the requirements of the application. The constant surface heights prescribed at the lateral boundaries differ form reality. However, the prognostic variables should never be interpreted near the boundaries due to their artificial character. In case of complex terrain (due

to land-use or topography), reliable values of the prognostic variables can be assumed some grid points from the boundaries.

The following boundary conditions are derived with respect to the assumptions mentioned above.

7.1 Lower boundary

Usually the surface is not a flat and homogenous plane, but rough, covered with vegetation (forest, grass, fields) or built-up (houses). From this the question arises, how to determine the height z_s of the lower model boundary. In METRAS/MITRAS it is considered as topography height, corresponding to the sum of surface height $h(x,y)$ and roughness length $z_o(x,y)$:

$$z_s(x,y) = h(x,y) + z_o(x,y) \tag{7.1}$$

However, since the roughness lengths within the considered areas are mostly very small, especially over water, z_0 is neglected when calculating the topographic height. Therefore, the lower model boundary corresponds to the orography height ($z_s(x,y) = h(x,y)$). The physical meaning of the lower boundary in the model, however, remains that of the topography height.

The discretized form of the lower boundary conditions used in METRAS/MITRAS are described in Appendix B.2.1.

7.1.1 Wind

The wind velocity at the surface usually follows a no-slip condition, thus the horizontal and vertical wind components are zero at the ground:

$$\begin{aligned} \bar{u}|_{z_s} &= 0 \quad \text{(a)} \\ \bar{v}|_{z_s} &= 0 \quad \text{(b)} \\ \bar{w}|_{z_s} &= 0 \quad \text{(c)} \end{aligned} \tag{7.2}$$

Corresponding to equation (2.24) the boundary condition for the pressure p_2 can be formulated with regard to equation (7.2):

$$\frac{\partial \dot{x}^1}{\partial x}\frac{\partial \dot{x}^3}{\partial x}\frac{\partial \hat{p}_2}{\partial \dot{x}^1} + \frac{\partial \dot{x}^2}{\partial y}\frac{\partial \dot{x}^3}{\partial y}\frac{\partial \hat{p}_2}{\partial \dot{x}^2} + \left(\left(\frac{\partial \dot{x}^3}{\partial x}\right)^2 + \left(\frac{\partial \dot{x}^3}{\partial y}\right)^2 + \left(\frac{\partial \dot{x}^3}{\partial z}\right)^2\right)\frac{\partial \hat{p}_2}{\partial \dot{x}^3} = 0 \tag{7.3}$$

7.1.2 Temperature

The temperature at the surface can be calculated from a surface energy budget equation:

$$(1-\alpha)(I+D)+L\downarrow -L\uparrow +Q_H+Q_E+Q_S+Q_F=0 \qquad (7.4)$$

Here $(1-A_0)(I+D)$ characterizes the direct and diffusive short wave radiation budget and can be calculated from the radiation scheme given in Section 3.6, or for more simple purposes, from $\mu I_\infty cosZ(t)$. The parameter μ depends on the albedo A_0, the amount of clouds, the turbidity of the air and the elevation of the sun. For a cloud free sky, μ can be estimated to $0.75\ (1\text{-}A_0)$ for Northern Germany (Golchert, 1981). With a typical value for the albedo A_0 over land, μ results in $0.75(1-0.2)=0.6$. The zenith angle $Z(t)$ is calculated in the model dependent on the terrain slope, time, latitude, etc. (Appendix A.5).

The incoming and outgoing long wave radiation L can also be calculated with respect to the radiation budget in the atmosphere or, more simple (e.g. for cloudfree skies), from $\hat{\varepsilon}\sigma T_s^4$ dependent on the surface temperature T_s, the Stefan-Bolzmann-constant $\sigma=5.67\cdot10^{-8}\ \mathrm{Wm^{-2}K^{-4}}$ and the parameter $\hat{\varepsilon}$. The last depends on the amount of clouds and the water content in the atmosphere. Following de Jong (1973) $\hat{\varepsilon}=0.22$ is used for a cloudfree sky.

The fourth and fifth terms in equation (7.4) characterize the sensible and latent heat fluxes. They are calculated dependent on the friction velocity u_* (equation (3.12)) and the scaling values for temperature θ_* (equation (3.20)**Fehler! Verweisquelle konnte nicht gefunden werden.**) and humidity q_*.

Q_s characterizes the heat flux and heat exchange with the ground and can be calculated from $Q_s=\nu_s(\partial\overline{T}/\partial z)_s$. Within the soil the conduction of heat can be calculated with a one-dimensional diffusion equation:

$$\frac{\partial\overline{T}_s}{\partial t}=\frac{\partial}{\partial z}\left(k_s\frac{\partial\overline{T}}{\partial z}\right) \qquad (7.5)$$

The last term in (7.4) denotes the anthropogenic heat emission.

Following Tiedtke and Geleyn (1975) and Deardorff (1978), equation (7.4) is solved by use of the force-restore method, resulting in:

$$\frac{\partial T_s}{\partial t}=\frac{2\sqrt{\pi}k_s}{\nu_s\cdot h_\theta}\left\{\mu\cdot I_\infty\cos(Z(t))-\hat{\varepsilon}\overline{T_s^4}+c_p\rho_0u_*\theta_*+l_{21}\rho_0q_*u_*-\sqrt{\pi}\nu_s\frac{\overline{T}_s-\overline{T}_s(-h_\theta)}{h_\theta}\right\} \qquad (7.6)$$

Here k_s is the thermal diffusivity and ν_s the thermal conductivity of the soil. The values used in the model for the different vegetation types are given in Table 3-2 of Schlünzen et al. (2018). The depth h_θ of the daily temperature wave can be calculated following Deardorff (1978) from k_s with $\tau_1=86400$ s.

$$h_\theta=\sqrt{k_s\cdot\tau_1} \qquad (7.7)$$

The temperature $\overline{T}(-h_\theta)$ may be kept constant for short range forecasts (e.g. a few days) or calculated from a prognostic equation (Deardorff, 1978):

$$\frac{\partial \overline{T}(-h_\theta)}{\partial t} = \frac{k_s}{\nu_s h_\theta \sqrt{365}} \left\{ \mu I_\infty \cos Z(t) - \hat{\varepsilon}\sigma \overline{T}_s^4 + c_p \rho_o \theta_* u_* + l_{21} \rho_o q_* u_* \right\} \tag{7.8}$$

The real temperature calculated from equation (7.6) is converted into potential temperature. The boundary value θ (lowest level) is calculated from $\theta(z_s)$ and $\theta(\text{first level})$ with the assumption of constant gradients:

$$\overline{\theta}\ (\text{lowest level}) = 2 \cdot \overline{\theta}(z_s) - \overline{\theta}\ (\text{first level}) \tag{7.9}$$

Thus, the surface temperature $\theta(z_s)$ is the mean of the values above and "below" the surface.

7.1.3 Humidity

The humidity at the surface is calculated from a budget equation following Deardorff (1978):

$$\begin{aligned} &\overline{q}^1_{1s} = \alpha_q \overline{q}^1_{1sat}(\overline{T}_s) + (1-\alpha_q)\overline{q}^1_1 \quad (\textit{first level}) \\ &\overline{q}^1_{1s} \le q^1_{1sat}(\overline{T}_s) \end{aligned} \tag{7.10}$$

The bulk soil water availability α_q can lie between W_s/W_k and 1 ($\alpha_q = \min(1, W_s/W_k)$) denotes the bulk soil moisture content (depth of liquid water) within the depth d_2 and W_k is the field capacity or saturated value of W_s given for each surface characteristic (values are provided in Table 3-2 of Schlünzen et al. (2018)). For α_q a prognostic equation can be derived:

$$\frac{\partial \alpha_q}{\partial t} = \frac{Q_E l_{21} + P}{\rho_w W_k} \tag{7.11}$$

Q_E is calculated from the turbulent humidity flux $Q_E = l_{21}\rho_s q_* u_*$, P denotes the precipitation and ρ_w the density of water (assumed to be 1000 kg m^{-3}). Similar to equation (7.9), the humidity 'below' the surface is calculated from $\overline{q}^1_{1s}$ and $\overline{q}^1_1$ (first level).

7.1.4 Liquid Water

Liquid Water is assumed to be deposed at the ground only in form of rain. From this assumption a zero flux boundary condition for the cloud water content arises, resulting in:

$$\overline{q}^{2c}_{1s} = \overline{q}^{2c}_1 \quad (\textit{first level}) \tag{7.12}$$

The flux of rain water to the ground is equal to the flux at the first grid level:

$$\left.\overline{w' q'^{2r}_1}\right|_{z_s} = -V_{TR}\ \overline{q}^{2r}_1(z_1) \tag{7.13}$$

7.1.5 Pollutants

Pollutants are partly absorbed at the surface and over water, e.g. at the topography height it can be written:

$$\frac{\partial \widetilde{C}_j(z_s)}{\partial z} \neq 0 \quad \textit{and} \quad \widetilde{C}_j(z_s) \neq 0 \tag{7.14}$$

The partial absorption results from the concentration flux to the surface and depends on the deposition velocity v_d and the concentration $\overline{C}_j$ at the first grid level with the height z_1:

$$\overline{w'C_j'} = -v_d\, \overline{C}_j(z_1) \tag{7.15}$$

The deposition velocity v_d depends on the turbulence in the atmosphere, chemical properties of the species, surface characteristics, and vegetation. Thus, no fixed value of v_d for all species and meteorological conditions can be given. In METRAS the deposition velocity can be calculated for 19 species (Section 4.2).

7.1.6 Sub-grid scale fluxes

The turbulent momentum fluxes at the ground follow the boundary condition (Clark, 1977):

$$\tau_{11} = \tau_{22} = \tau_{33} = \tau_{12} = 0 \tag{7.16}$$

The stress tensor components $\tau_{13} = -\rho_o \overline{u'w'}$ and $\tau_{23} = -\rho_o \overline{v'w'}$ are derived from similarity theory. If the wind direction is given by $\alpha_d = \arctan(\overline{u}/\overline{v})^1$, τ_{13} and τ_{23} can be written

$$\begin{aligned} \tau_{13} &= \rho_0 u_*^2 \sin\alpha_d \qquad (a) \\ \tau_{23} &= \rho_0 u_*^2 \cos\alpha_d \qquad (b) \end{aligned} \tag{7.17}$$

With (3.13) and (3.14) the momentum exchange between surface and atmosphere is completely described.

For test purposes a free-slip condition at the ground can be used. In this case the friction velocity u_* is set zero, neglecting friction effects at the ground.

The horizontal turbulent fluxes of scalar variables at the ground follow the boundary condition (Clark, 1977):

$$\rho_0 \overline{u'\chi'} = \rho_0 \overline{v'\chi'} = 0 \quad ; \quad \chi = \theta, q, C_j \tag{7.18}$$

The vertical fluxes of scalar variables at the ground are derived from

$$\rho_0 \overline{w'\chi'} = -\rho_0 u_* \chi_* \quad ; \quad \chi = \theta, q, C_j \tag{7.19}$$

where the scaling variable χ_* is calculated from profiles of the temperature $\bar{\theta}$ and humidity $\overline{q}_1^1$ corresponding to **Fehler! Verweisquelle konnte nicht gefunden werden.**

7.2 Upper Boundary

The upper model boundary is located at a height z_t (Figure 2.1). Since no physical boundary exists in the atmosphere, the boundary conditions of the model must permit vertical propagating waves to leave the model area without reflections. Several boundary conditions for wind, pressure and scalars are implemented in METRAS/MITRAS. In Appendix B.2.2 they are described in detail. Usually it is assumed that the gradients of the horizontal wind components normal to the boundary vanish:

$$\left.\frac{\partial \overline{u}}{\partial z}\right|_{z_t} = 0 \qquad \left.\frac{\partial \overline{v}}{\partial z}\right|_{z_t} = 0 \tag{7.20}$$

The vertical wind component also vanishes at the upper boundary:

$$\overline{w}\,|_{z_t} = 0 \tag{7.21}$$

From these assumptions it follows that the normal pressure gradient is also zero, $\partial \hat{p}_2 / \partial \dot{x}^3 = 0$. To avoid reflections of vertical propagating waves at this rigid upper boundary, absorbing layers are introduced. They are realized by adding so-called Rayleigh damping terms to the balance equations (2.23) and (2.27) to (2.29) (Clark, 1977; Durran, 1981). These additional terms cause an increasing adaption of the prognostic variables to their corresponding and prescribed synoptic values with increasing height. In the equations of motion the damping terms are written:

$$\begin{aligned} R_1 &= -\rho_0 \alpha^* (\overline{u} - U_g)\, \nu_R \qquad (a) \\ R_2 &= -\rho_0 \alpha^* (\overline{v} - V_g)\, \nu_R \qquad (b) \\ R_3 &= -\rho_0 \alpha^* \overline{w} \nu_R \qquad (c) \end{aligned} \tag{7.22}$$

The relaxation coefficient $\nu_R [s^{-1}]$ increases with height

$$\nu_R = \begin{cases} 0 & \text{for } k < k_D \\ \delta^{(k_t - k)} & \text{for } k \geq k_D \end{cases} \tag{7.23}$$

In (7.23) k denotes the vertical grid point index, k_t the index of the highest grid point at the upper boundary and k_D the index of the first absorbing layer. From several tests $\delta [s^{-1}] = 0.2$ seems to be a good choice.

The absorbing layers damp vertical propagating waves and prevent their reflection at the upper boundary. To preserve the height of the physical model area the absorbing layers have to be added at the upper boundary. Alternative boundary conditions, e.g. to obtain the pressure field from a Fourier transformation of the vertical wind field (Klemp and Dur-

ran, 1983; Bougeault, 1983) are not implemented due to the minimum additional memory resources (about 20 % for five absorbing layers) necessary for the absorbing layers.

The temperature gradient at the upper boundary results from the assumption $\overline{w'\theta'}|_{z_t} = 0$:

$$\left.\frac{\partial\bar{\theta}}{\partial z}\right|_{z_t} = 0 \tag{7.24}$$

The humidity and concentration values are calculated from analogous boundary conditions.

Corresponding to the boundary conditions for velocities (7.16), the turbulent momentum fluxes and their gradients at the upper boundary are zero:

$$\begin{aligned} \tau_{13} &= \tau_{23} = \tau_{33} = 0 \qquad \text{(a)} \\ \frac{\partial\tau_{11}}{\partial\dot{x}^3} &= \frac{\partial\tau_{22}}{\partial\dot{x}^3} = \frac{\partial\tau_{12}}{\partial\dot{x}^3} = 0 \qquad \text{(b)} \end{aligned} \tag{7.25}$$

7.3 Lateral Boundaries

As the upper boundary the lateral boundaries are artificial. On one hand the lateral boundary conditions have to permit waves to leave the model area without reflections, on the other hand the synoptic values should influence the prognostic model variables at the inflow boundaries.

7.3.1 Wind

The most robust form is a non-reflecting boundary condition, implemented in METRAS/MITRAS by directly calculating the boundary normal wind components as far as possible from the prognostic equations. The boundary normal advection is treated by the use of the Orlanski condition at inflow boundaries and of the upstream scheme at outflow boundaries. For the boundary parallel components of the velocity a zero-flux condition is assumed.

As a further option three-dimensional radiative boundary conditions may be used. The radiative boundary conditions introduced by Orlanski (1976) for one-dimensional applications and extended by Raymond and Kuo (1984) to two-dimensional phenomena are implemented in METRAS in a three-dimensional form. The derivation of radiative boundary conditions of Raymond and Kuo (1984) is only valid for horizontally oriented phenomena. In this form they are often used in mesoscale models. If vertical propagating waves exist at lateral boundaries, they must fail. Several tests gave evidence that reflections at the lateral boundaries are reduced when using the three-dimensional formulation instead of the two-dimensional one. To reduce errors from reflections the three-dimensional form is

implemented in METRAS (Schlünzen, 1988) and derived below. For clarity it is assumed that no slopes exist parallel to the boundary. However, within the model these terrain inhomogeneities are taken into account.

The advection equation, expanded three-dimensional from equation (7.26) in Raymond and Kuo (1984), can be written in the coordinate system $\dot{x}$:

$$\frac{\partial \psi}{\partial t} = -\left[c_1 \frac{\partial^1}{\partial x} \frac{\partial \psi}{\partial \dot{x}^1} + c_2 \frac{\partial \dot{x}^2}{\partial y} \frac{\partial \psi}{\partial \dot{x}^2} + c_3 \frac{\partial \dot{x}^3}{\partial z} \frac{\partial \psi}{\partial \dot{x}^3} \right] \tag{7.26}$$

Here ψ characterizes a meteorological field (e.g. $\rho_o \dot{\alpha} \bar{u}$) and c_1, c_2, c_3 the projection of the phase velocity c on $\dot{x}^1$–, $\dot{x}^2$–, $\dot{x}^3$-direction, respectively. The c_i are defined as follows:

$$\begin{aligned} c_1 &= F_1 \frac{\partial \dot{x}^1}{\partial x} \frac{\partial \psi}{\partial \dot{x}^1} \frac{1}{F_2} \qquad (a) \\ c_2 &= F_1 \frac{\partial \dot{x}^2}{\partial y} \frac{\partial \psi}{\partial \dot{x}^2} \frac{1}{F_2} \qquad (b) \\ c_3 &= F_1 \frac{\partial \dot{x}^3}{\partial z} \frac{\partial \psi}{\partial \dot{x}^3} \frac{1}{F_2} \qquad (c) \end{aligned} \tag{7.27}$$

With

$$\begin{aligned} F_1 &= -\frac{\partial \psi}{\partial t} \qquad (a) \\ F_2 &= \left(\frac{\partial \dot{x}^1}{\partial x} \frac{\partial \psi}{\partial \dot{x}^1}\right)^2 + \left(\frac{\partial \dot{x}^2}{\partial y} \frac{\partial \psi}{\partial \dot{x}^2}\right)^2 + \left(\frac{\partial \dot{x}^3}{\partial z} \frac{\partial \psi}{\partial \dot{x}^3}\right)^2 \qquad (b) \end{aligned} \tag{7.28}$$

(7.26) is discretized with respect to the numerical schemes in METRAS. The components $\rho_o \alpha^* \bar{u}, \rho_o \alpha^* \bar{v}, \rho_o \alpha^* \bar{w} = \psi$ of the momentum vector are discretized centered-in-space using the Adams-Bashforth scheme. The gradients normal to the boundaries are calculated from differences on the inner side of the boundary. The phase velocities c_i are limited in accordance to the stability criteria of the used numerical schemes. These coupled boundary conditions allow waves to leave the model area without reflections.

Somewhat different lateral boundary values result for a nesting of METRAS in METRAS or in other model results (Chapter 8). However, for nested runs in principle the same boundary conditions are used.

7.3.2 Pressure and thermodynamic quantities

The boundary conditions used for momentum have to be considered in the formulation of the pressure boundary condition. For the pressure p_2 it follows that its gradient normal to the boundary vanishes. The normal gradients of temperature, humidity and concentrations usually are also set zero (Appendix B.2.3.2).

As the velocity components the scalar quantities may also be nested (Chapter 8).

7.3.3 Pollutants

For concentrations a time dependent boundary condition is implemented at the inflow boundary (Niemeier, 1997) in addition to the boundary conditions of Section 6.3.2. With that, transport of pollutants across the boundaries can be calculated close to reality, as emissions in the upwind area determine the advected air masses and the diurnal changes of the concentrations are included. This boundary condition needs more computation time as before, and a simulation in a larger area is necessary to get the values at the boundaries. The results of the first simulation are interpolated to the higher resolving grid of the second simulation. This is done once for the three dimensional area to get start values. In addition at each hour the values are interpolated to receive data at the boundaries. Inbetween, the boundary data are interpolated linear in time. For the outflow boundaries a zero gradient condition is used.

8 Nesting of METRAS

METRAS runs may be nested in results of other models or in METRAS results that were created with a coarser grid. The basic ideas for the nesting are described in this chapter. Details on the available programs can be found in Chapter 1 of Schlünzen et al. (2018). It has to be noted that the nesting is not fully tested yet. Therefore, the user must carefully check the results of nested METRAS runs.

8.1 Basic Ideas of the model nesting

Two conceptionally different methods are implemented in METRAS. The scale separation concept forces large-scale values only, while the nudging concept forces the prognostic variables.

8.1.1 Scale separation concept

The METRAS model may be forced by continuously changing the large-scale values (θ_0, p_0, q_0, etc.). This scheme corresponds to a scale separation concept in the way that the large-scale values are interpreted as results given by a coarse resolving model and the calculated values of $\overline{u}$, $\overline{v}$, $\overline{w}$, $\overline{\theta}$, $\overline{\chi}$ are the resulting total values, with $\widetilde{u}$, $\widetilde{v}$, $\widetilde{w}$, $\widetilde{\theta}$, $\widetilde{\chi}$ corresponding to the disturbances from the large-scale values (compare Section 2.3). To include this forcing no changes of the original METRAS equations are needed, since all large-scale values are already implemented in such a manner that they can be considered as dependent of time and space. However, the actual large scale data are calculated by linear interpolation in time from the forcing data set. Therefore two additional large scale fields for each forced variable are needed.

The coarse grid data are interpolated in the preprocessors on the fine grid used in the nested model (Section 8.2). The preprocessors have to ensure that the large-scale equations are fulfilled, namely the hydrostatic approximation (2.17) and the ideal gas law ($p_0 = \rho_0 R T_0$). It has to be kept in mind that the large-scale wind has not to be in geostrophic balance. Equation (2.18) and thus U_g, V_g are only introduced to simplify the equations slightly and to reduce numerical inaccuracies in the large-scale pressure gradients introduced by the interpolation of pressure from a coarse to a fine mesh.

8.1.2 Nudging concept

The basic idea of the nudging concept is to replace the boundary values of the prognostic variables in METRAS at the lateral and/or upper boundaries of the model domain by values calculated by a model with a coarser grid. The advantage of this nesting concept is its

applicability for a one-way as well as a two-way nesting of METRAS in a model that uses a coarse grid. In addition, a nudging to measurements might be performed. At present, only the one-way nesting is implemented in METRAS and the corresponding preprocessors.

To nudge METRAS, an additional forcing term has to be included in the equations. The term is added so that the values at each time step are calculated as weighted means of the data from the METRAS original equations (ψ_u) and the coarse mesh forcing data set (ψ_c):

$$\psi_f = (1-\delta_1)\psi_u + \delta_1\psi_c \tag{8.1}$$

δ_1 denotes a weighting factor. If its value is 1, only the large-scale forcing data remain. If its value is zero, only the unforced model results remain. The value of δ can be defined quite differently (e.g. Perkey and Kreitzberg, 1976; Davies, 1976; Källberg, 1977; Lehmann, 1993).

Instead of a weighting factor δ_1 a nudging coefficient is used in METRAS. It is calculated from

$$\delta = \delta_0\left(1-\tanh\left(\frac{a_f}{N-3}i\right)\right). \tag{8.2}$$

The values $\delta_0 = 0.001\ s^{-1}$, $a_f = 0.4$ and $N = 4$ are used for a standard nudging (characteristic time $1/\delta_0$ about 30 minutes at the boundaries). With an intensified nudging $\delta_0 = 0.01\ s^{-1}$ is used (Ries et al., 2010), resulting in a characteristic time of about 3 minutes at the boundaries.

For including obstacles like buildings $\delta = \delta_0 = 0.99999\ s^{-1}$ may also be applied at all grid points within the obstacles. In this case the momentum fluxes around the buildings or the surface energy budget might not be very realistic, but the dynamic effect is well reflected.

Index i in equation (8.2) is the number of grid points counted from the boundary into the inner model domain. The nudging coefficient δ increases towards the lateral and upper boundaries. Forcing is applied to all prognostic calculated variables.

Equation (8.1) can be rewritten to show that the forcing corresponds to a diffusion term.

$$\psi_f{}^{n+1} = \psi_f{}^{n} + \Delta t\frac{\partial\psi_u}{\partial t} + \delta\Delta t(\psi_c{}^{n+1} - \psi_u{}^{n+1}) \tag{8.3}$$

In this equation $\psi_f{}^{n}$ denotes the model results at time step n. The second term contains the temporal change of ψ_f resulting from the original METRAS equations alone (denoted

here as $\partial\psi_u/\partial t$. Both terms summed up correspond to the model results at time step ψ_u^{n+1}, when nesting is neglected. The last term in equation (8.3) describes the forcing due to the imbalance between the integrated METRAS results (ψ_u^{n+1}) and the prescribed large-scale value ψ_c^{n+1}. To derive equation (8.3) forward differences are assumed for the time integration.

Summarizing and reordering the first two terms, equation (8.3) can be written as

$$\psi_f^{n+1} = \psi_u^{n+1} + \delta\Delta t\left(\psi_c^{n+1} - \psi_u^{n+1}\right) \tag{8.4}$$

or

$$\psi_f^{n+1} = \delta\Delta t\,\psi_c^{n+1} + (1-\delta\Delta t)\psi_u^{n+1} \tag{8.5}$$

which corresponds to equation (8.3) for $\delta_1 = \delta\Delta t$.

As for the Coriolis force, the deviation between north direction and the grid's y-direction ξ must be considered when nudging wind velocity components (Spensberger, 2010):

$$\begin{pmatrix} u_c \\ v_c \end{pmatrix} = \begin{pmatrix} \cos\xi & -\sin\xi \\ \sin\xi & \cos\xi \end{pmatrix} \cdot \begin{pmatrix} u_{east} \\ v_{north} \end{pmatrix} \tag{8.6}$$

The angle ξ is an intrinsic property of the model grid and varies with each grid point.

Equation (8.3) cannot be directly used in the model for the wind components, because this equation does not necessarily fulfill the anelastic approximation, which is only guaranteed for $\psi_{u_i}^{n+1} = \overline{u}_i^{n+1}$ at the end of the time step $n+1$. The reason for this is the invalidity of the anelastic approximation of the wind forcing field $\overline{u}_{ic}^{n+1}$due to the interpolation in time. To avoid this problem, the field of the dynamic pressure part p_2 is calculated in such a manner that the gradient of the dynamic pressure in the momentum equations guarantees the anelastic approximation for $\overline{u}_f^{n+1}$. To ensure this the 'preliminary' velocities needed in equation (2.24) contain the forcing term of equation (8.3). This integration method is only possible due to the knowledge of the forcing field $\overline{u}_{ic}$ for the time step $n+1$.

Equation (8.3) is directly used to force the scalar quantities.

8.2 Interpolation of forcing data

Independent of the model which is used to force METRAS, the results have to be interpolated on the METRAS grid. Therefore different preprocessors exists (Chapter 1 of Schlünzen et al., 2018). The interpolation algorithm used in the different preprocessors is always the same. The values given on the coarse grid of the forcing model are linearly interpolated to METRAS-grid.

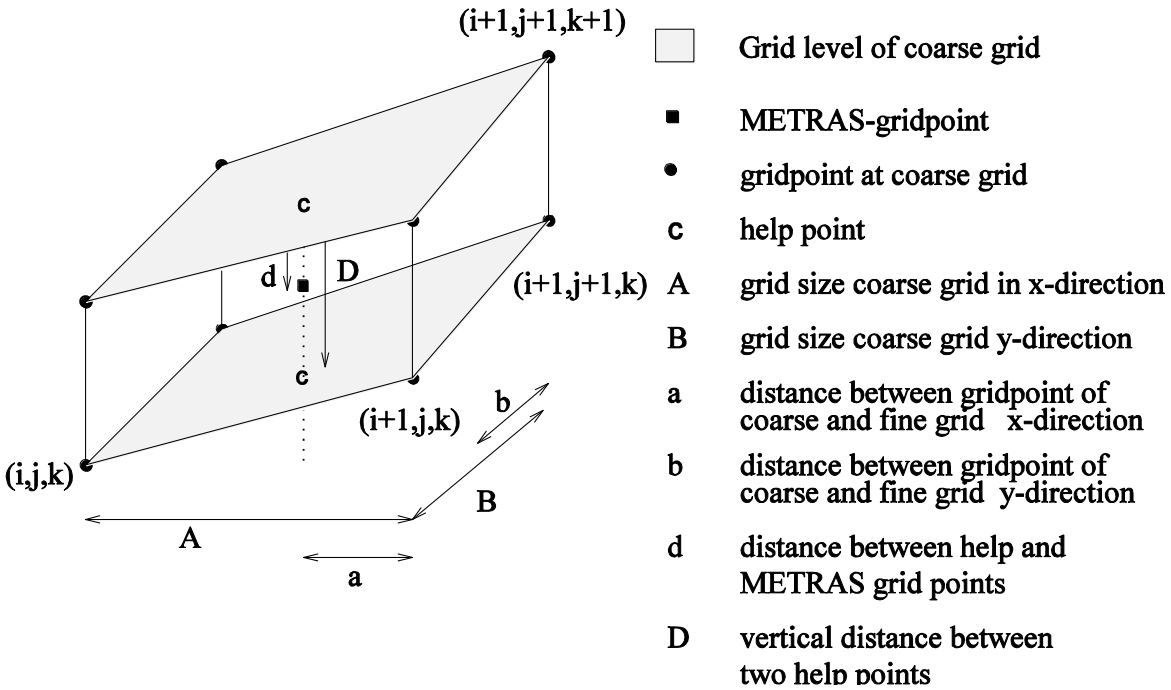

Figure 8.1: Interpolation points

Figure 8.1 shows the necessary grid points and distances needed for the interpolation. First the values of the coarse grid are interpolated within their corresponding grid level to the METRAS grid point, projected at that level (named 'help point' in Figure 8.1). The grid points on the coarse grid that surround the projected METRAS grid point are needed for this purpose. The four grid points of one grid level of the coarse grid are also used to calculate the height of the 'help point'. For the interpolation the distances between the grid points of the coarse grid (A and B) and between the 'help point' and coarse grid points (a and b) are necessary.

The heights of the help points are used to determine the vertical distance D between the two grid levels of the coarse grid. In addition the distance between the higher grid level and the METRAS grid point is needed. With these data the three-dimensional interpolation of the values from the coarse grid to the fine METRAS-grid can be done following Press et al. (1989)

$$
\begin{aligned}
C(finegrid) = {} & (a & b & d & C(i,j,k) \\
+ {} & (A-a) & b & d & C(i+1,j,k) \\
+ {} & a & (B-b) & d & C(i,j+1,k) \\
+ {} & (A-a) & (B-b) & d & C(i+1,j+1,k) \\
+ {} & a & b & (D-d) & C(i,j,k+1) \\
+ {} & (A-a) & b & (D-d) & C(i+1,j,k+1) \\
+ {} & a & (B-b) & (D-d) & C(i,j+1,k+1) \\
+ {} & (A-a) & (B-b) & (D-d) & C(i+1,j+1,k+1) \\
/ {} & (ABD) & & &
\end{aligned}
\qquad (8.7)
$$

If a surface METRAS grid point is below the lowest 'help point', the height of the lowest 'help point' is used for the interpolation of the data to the METRAS surface grid point. The values are interpolated from the four grid points at the lowest coarse grid level and used as surface data in the METRAS fine mesh.

9 Initialization of the Model

The initialization of the three-dimensional model is done in three steps (Table 3). First, the spatial resolution of the model area and the location of the grid points have to be determined and the characteristic parameters of topography and land-use have to be interpolated to the grid points. In a second step by using the one-dimensional model version a stationary data set for initialization of the three-dimensional model is calculated. As an alternative the preprocessors as described in Section 7 might be used. In the third step the data set of step two is used for initializing the three-dimensional model. During the initialization phase of the three-dimensional model the orography grows slowly (diastrophism) until the real orography heights have been established. The initialization phase takes 2 to 8 hours, dependent on the stratification.

Task to be solved	**Solved by**
Determination of model area characteristics	modelling expert
Determination of grid	modelling expert, grid generation program
Interpolation of orography and land-use characteristics to grid points	grid generation program
Output of model area characteristics	
Calculation of initial data sets (one-dimensional model or three-dimensional preprocessor - Chapter 7)	1D model or 3D preprocessor
Input of model area characteristics	1D model
Calculation of coefficients A to G (defined by (A.*11*))	
Input and calculation of consistent large-scale values	
Input and calculation of consistent deviations for initialization	
Calculation of a stationary solution by numerical integration of the one-dimensional model equations	
Input of model area characteristics	3D model
Calculation of coefficients A to G (defined by (A.*11*))	
Calculation of initial data sets (three-dimensional model)	
Input of the one-dimensional stationary solution for initialization	
Diastrophism and calculation of adapted large-scale and deviation values	
Calculation of stationary or instationary solutions by numerical integration of the three- dimensional model equations	

Table 3: Initialization of the three-dimensional model (schematic description.)

9.1 Initialization of orography and land-use characteristics

The characteristic parameters orography, roughness, albedo etc. are interpolated to the 'locations' of the horizontal grid points by use of the preprocessor GRITOP. This preprocessor uses an area-weighting interpolation procedure and supplies the mesoscale model

with information on the partial land-use and the corresponding characteristic parameters within each grid volume. For details on this preprocessor and the interpolation procedure refer to Wosik et al. (1994b). An analogous interpolation procedure (preprocessor EMIINI) is applied to the initialization of emission inventories (Wosik et al., 1994a).

After determining the topographic heights z_s at each grid point and the height of grid levels above flat terrain, the height of each grid point above the topography can be calculated from equation (A.8).

9.2 Initialization of 1-d Model

From the area characteristic parameters the coefficients A to G at each grid point are calculated according to (A.11) and Figure 6.1. Afterwards the large-scale and meso-scale values are read and derived from the input values, respectively. Finally the one-dimensional model equations are integrated until the calculated meteorological profiles become stationary.

9.2.1 Large-scale values

For determining the geostrophic wind V_g, potential temperature θ_0, specific humidity q^1_{1o} and liquid water content q^2_{1o}, following values have to be predefined:

- pressure p_0 at sea level
- geostrophic wind V_g at sea level or a profile of V_g
- temperature T_o at sea level and a temperature gradient $\gamma = \partial T_o / \partial z$ or
- temperature profile T_o
- profile of the relative humidity
- profile of liquid water content q^2_{1o}

These data sets are given in accordance to the application under consideration. They are taken from observations, weather charts or analysis (e.g. Luthardt, 1987). For the calculation of consistent large-scale values the hydrostatic (2.17) and geostrophic approximation (2.18) are presumed. Assuming a constant temperature gradient within each grid layer the temperature profile follows from:

$$T_o(z) = T_o(NN) + \gamma \cdot z \tag{9.1}$$

The hydrostatic assumption together with the layer-wise constant temperature gradient γ yields the pressure profile

$$p_o(z) = p_o(NN)\left(\frac{T_o(z)}{T_o(NN)}\right)^{-g/(R\cdot\gamma)} \tag{9.2}$$

The density ρ_0 is calculated by use of the ideal gas law as a function of pressure and temperature:

$$\rho_o = \frac{p_o}{RT_o} \tag{9.3}$$

If not predefined, the potential temperature θ_0 can be derived from the large-scale profiles by use of (2.5).

9.2.2 Mesoscale values

Due to the assumption of horizontal homogeneity no vertical winds can develop in the one-dimensional model version. Thus the preliminary vertical wind and the mesoscale pressure p_2 are zero, resulting in $\tilde{p} = p_1$ for the one-dimensional case. Usually, the initial temperature perturbation $\tilde{T}$ is zero, but it can also be prescribed by a measured temperature profile. The mesoscale density deviation $\tilde{\rho}$ is calculated by (2.20) and the mesoscale pressure p_1 by (2.19). Now the mesoscale density $\tilde{\rho}$ can be calculated again. This iteration procedure is continued until the changes in $\tilde{\rho}$ become very small, namely $|\Delta\tilde{\rho}| < 0.01\cdot|\tilde{\rho}|$. Now the potential temperature $\tilde{\theta}$ can be calculated by:

$$\tilde{\theta} = \tilde{T}\left(\frac{P_r}{p_o+\tilde{p}}\right)^{R/c_p} - \theta_o\left\{1-\left(\frac{p_o}{p_o+\tilde{p}}\right)^{R/c_p}\right\} \tag{9.4}$$

For a shallow model area the horizontal wind components are initialized from the Ekman formulas, but usually their initial values are set equal to the geostrophic components. The Ekman profiles are derived from the simplified boundary layer equations with the assumption $K_{vert} = 10\ \mathrm{m^2 s^{-1}} = const.$ by (e.g. Dutton, 1976):

$$\begin{aligned} \bar{u}_k &= U_{gk}\ \{1-e^{-\lambda z}\cos\lambda z\} - V_{gk}\ e^{-\lambda z}\sin\lambda z \qquad \text{(a)} \\ \bar{v}_k &= U_{gk}\ e^{-\lambda z}\sin\lambda z + V_{gk}\ \{1-e^{-\lambda z}\cos\lambda z\} \qquad \text{(b)} \end{aligned} \tag{9.5}$$

where $\lambda = \sqrt{f/2K_{vert}}$ and z denotes the height of the scalar grid points. At a height π/λ it is assumed that $v = (\bar{u},\bar{v},0) = (U_g,V_g,0)$.

9.2.3 Stationarity

The one-dimensional model equations are integrated starting with the predefined initial profiles and using the same boundary conditions but without diurnal cycles as in the three-dimensional model. When starting the integration the wind profiles are not adapted to the thermodynamic variables and reverse. So the dynamic equations are integrated with a

fixed temperature profile until the wind profiles become stationary. Stationarity is defined by

$$|\Delta\psi| < a \cdot \Delta t \tag{9.6}$$

where ψ stands for the horizontal wind components $\bar{u}$ or $\bar{v}$ and $\Delta\psi$ denotes changes of ψ from one time step to the next. The constant a is derived from a scale analysis of the equation of motion for typical mesoscale phenomena: In the one-dimensional model equations the Coriolis force with an acceleration $f\bar{u}$ is small compared to the other forces. For mean latitudes with $f \cong 10^{-4}\,s^{-1}, |\bar{u}| \cong 10\,ms^{-1}$ the acceleration results in . Stationarity can be assumed, if changes of u and v during one time step are less than 1 % of the maximum Coriolis acceleration. From this a value of $a = 10^{-5}\,ms^{-2}$ can be derived for the one-dimensional model version. For a sufficient damping of inertial oscillations the simulations should be done for several days. Usually a simulation is interrupted after 80.000 time steps even if the profiles are not stationary.

If the wind profiles are stationary, wind and temperature are integrated simultaneously until all profiles are stationary again. These profiles are transferred to the three-dimensional model for initialization.

9.3 Initialization of 3-d model

As in the one-dimensional model the coefficients A to G are derived from the area characteristics. First of all the topographic heights are neglected and the stationary profiles of the one-dimensional model are expanded over the model area under the assumption of horizontal homogeneity or the results of the preprocessor are used. Afterwards the initialization by diastrophism (Groß, 1984) starts. This means that the surface heights grow from time step to time step until the real heights are achieved. During the process of diastrophism the vertical coordinate η (eq. 2.6) changes according to

$$z_{s,p}^{n+1} = z_{s,p}^{n} + A_f \cdot z_s \tag{9.7}$$

z_s denotes the final surface height, A_f the reciprocate of the number of time steps for diastrophism, and $z_{s,p}^{n}$ the temporal surface height at time $n \cdot \Delta t$. $1/A_f$ typically lies between 100 and 1000 and should ensure that vertical winds arising from the topography growing do not exceed 0.1 m/s. Such artificial vertical winds decrease with increasing integration time.

The wind components in the one-dimensional profile may either be seen as wind components in the three-dimensional model grid or as wind components aligned to the East and to the North. In the latter case winds must be turned into the model grid as demonstrated for nudging of wind components in equation (9.6).

The large-scale values are adapted to the actual topographic heights at each time step. They remain horizontal homogenous with respect to the sea level. As an example the adaption of the large-scale temperature follows:

$$T_0^n(x,y,z) = T_0(NN) + \gamma\left(z\frac{z_t - z_{s,p}^n(x,y)}{z_t} + z_{s,p}^n(x,y)\right) \tag{9.8}$$

The large-scale pressure p_0 and density p_0 are calculated from (9.2) and (9.3), respectively, and the potential temperature from (2.5).

In contrast to the large-scale values the mesoscale variables are adapted to the changing coordinate system by integrating the prognostic equations over $1/A_f$ time steps. The integration is continued without interruption as long as specified by the user. It is usually assumed that the meteorological fields are independent from initialization after about three hours of integration time. For unstable stratification the initialization time might take up to 8 hours.

10 Sea ice model MESIM

The mesoscale sea ice model MESIM was developed by Birnbaum (1998). It is based on a large scale model from Fischer (1995) and Harder (1996) who advanced the model developed by Hibler (1979). Further improvements concerning boundary conditions and surface temperature were done by Dierer (2002).

MESIM consists of two parts representing the dynamic and the thermodynamic processes, respectively. It can be run in either of these modes separately or in a combined mode which applies the full dynamic-thermodynamic equations. In the dynamic part, the momentum equation for drifting ice is solved. The internal forces in the ice are treated with the viscous-plastic rheology proposed by Hibler (1979). The equations of the thermodynamic part are based on the one-dimensional multilayer model developed by Maykut and Untersteiner (1971) and allow for non-linear temperature gradients in the ice.

The ice model is fully coupled to the atmosphere model METRAS. Interactions include momentum, heat, humidity and radiation fluxes. For example, the ice drift depends on the wind, the edges of ice floes act as roughness elements influencing the boundary layer, and ice growth is affected by air temperature and solar radiation.

Please note: The nomenclature of variable names in this chapter might overlap with the names in the rest of the document. Sea ice variables keep their meaning only in this chapter. A list of symbols is provided in the beginning of the document.

10.1 General Concept: Ice classes and basic variables

The sea ice in MESIM is distributed into different ice classes which represent different ice thicknesses and, therefore, different ice characteristics. This is especially relevant if an accurate determination of heat fluxes between atmosphere and ice is desired because even small amounts of thin ice affect the total heat flux in a grid cell tremendously (Birnbaum, 1998). The ranges of the four ice classes used in MESIM are shown in Table 4.

The sea ice in each ice class c is characterized by following properties:

- Ice concentration (percentage of grid cell coverage): A_c
- Mean ice thickness: $h_{i,c}$
- Mean snow thickness on top of the ice: $h_{s,c}$
- Mean length of ice floes: $L_{i,c}$
- Mean spacing between ice floes (“length of water surface”): $L_{w.c}$
- Mean temperature profile inside the ice: $T_{i,c}(z)$

Table 4: Ice classes and respective thicknesses used in MESIM.

Number of ice class	Corresponding ice thickness
1	0 cm – 10 cm
2	10 cm – 40 cm
3	40 cm – 1 m
4	> 1 m

Except for the spacing between ice floes, all variables are prognostic. Their determination, using budget equations, is shown in section 10.2. Section 10.3 demonstrates how the temperature profile is calculated by applying the heat transfer equation.

10.2 Dynamic part

The dynamic part of MESIM covers those processes involving mechanical forces which lead to changes in ice concentration and ice thickness. Beside the ice drift, these include the formation of open water due to shearing deformation and the amassment of ice in convergent drift regimes.

10.2.1 Budget equations

The prognostic parameters which characterize the ice change dynamically according to the budget equations:

$$\left(\frac{\partial}{\partial t}\right)_{dyn} A = -\nabla \cdot \left(\vec{v}_i A\right) - S_{A,dyn} \tag{10.1}$$

$$\left(\frac{\partial}{\partial t}\right)_{dyn} A_c = -\nabla \cdot \left(\vec{v}_i A_c\right) - S_{A,dyn,c} \tag{10.2}$$

$$\left(\frac{\partial}{\partial t}\right)_{dyn} \left(A_c h_{i,c}\right) = -\nabla \cdot \left(\vec{v}_i \left(A_c h_{i,c}\right)\right) \tag{10.3}$$

$$\left(\frac{\partial}{\partial t}\right)_{dyn} \left(A_c h_{s,c}\right) = -\nabla \cdot \left(\vec{v}_i \left(A_c h_{s,c}\right)\right) \tag{10.4}$$

$$\left(\frac{\partial}{\partial t}\right)_{dyn} \left(A_c L_{i,c}\right) = -\nabla \cdot \left(\vec{v}_i \left(A_c L_{i,c}\right)\right) \tag{10.5}$$

A represents the total ice concentration in the respective grid cell, A_c the ice concentration in ice class c, $h_{i,c}$ the ice thickness in class c, $h_{s,c}$ the snow thickness in ice class c and $L_{i.c}$

the length of ice floes in ice class c. To determine these values, the ice drift velocity $\vec{v}_i$ and the sink terms $S_{A,dyn}$ and $S_{A,dyn,c}$ need to be known. $S_{A,dyn}$ and $S_{A,dyn,c}$ describe the effect that the formation of open water due to shearing deformation has on the total ice concentration and the ice concentration in the class c, respectively. This process is discussed in section 10.2.5.

10.2.2 Momentum equation

The ice drift velocity $\vec{v}_i$ is calculated from the momentum equation:

$$m_i \frac{d\vec{v}_i}{dt} = -m_i f \vec{k} \times \vec{v}_i + \vec{\tau}_a + \vec{\tau}_w - m_i g \nabla h_{oc} + \vec{F}_\sigma \tag{10.6}$$

It is regulated by the Coriolis force (mass of ice: m_i, Coriolis parameter: f, unity vector in vertical direction: $\vec{k}$), the atmospheric drag force $\vec{\tau}_a$, the oceanic drag force $\vec{\tau}_w$, the force due to the tilt of the sea surface (sea surface height h_{oc}) and the forces due to internal stresses in the ice $\vec{F}_\sigma$. The gradient of the sea surface tilt depends on the velocity of the geostrophic ocean current $\vec{v}_{oc}$ so that:

$$\nabla h_{oc} = -\frac{f}{g}\left(\vec{k} \times \vec{v}_{oc}\right) \tag{10.7}$$

10.2.2.1 Atmospheric drag

The influence of the wind on the ice drift consists of two parts, the surface drag due to roughness elements on the ice, $\vec{\tau}_{a,s}$, and the form drag of the ice floes which jut out of the water surface, $\vec{\tau}_{a,f}$. The surface drag is calculated using the friction velocity $u_{*,i}$ as described in section 3.3.1, with the roughness length set to 1 mm for every ice class:

$$\tau_{a,s} = \rho_0 u_{*,i}^2 \tag{10.8}$$

with the large scale densitiy of air ρ_0. For determining the form drag part, a logarithmic wind profile over the water surface is assumed. This is integrated until the height of freeboard $h_{f,c}$ to estimate the total wind pressure acting on the floe. $h_{f,c}$ can be determined - using Archimedes' law - from the snow thickness h_s, the ice thickness h_i and the densities of ice ρ_i, snow ρ_s, and water ρ_w, respectively:

$$h_{f,c} = h_s + h_i - \left(\frac{\rho_i h_i + \rho_s h_s}{\rho_w}\right) \tag{10.9}$$

With it, the form drag can be calculated from

$$\tau_{a,f} = 0.5\rho_0 \frac{1}{L_{i,c} + L_{w,c}} \left(1 - \exp\left(-0.18 \frac{L_{w,c}}{h_{f,c}}\right)\right)^2 \frac{u_{*,w}^2}{\kappa^2} \int_{z_{o,w}}^{h_{f,c}} \left[\ln\left(\frac{z}{z_{0,w}}\right) - \psi_{m,w}\right]^2 dz \qquad (10.10)$$

where the shadowing effect from neighbouring ice floes is allowed for by the *exp*-expression. Required quantities are the length of ice floes $L_{i,c}$, the spacing between the floes $L_{w,c}$, the friction velocity over water surfaces $u_{*,w}$, the roughness length of water surfaces respective to wind $z_{0,w}$, the von-Karman constant κ and the stability function for momentum over water surfaces $\psi_{m,w}$. The latter is calculated according to equation 3.13.

To combine the effects from surface drag and form drag, a weightning function is applied by which the impact of surface drag is reduced in conditions with little ice cover.

$$\tau_a = \tau_{a,s} + \frac{1}{1 - A_w} \tau_{a,f} \qquad (10.11)$$

10.2.2.2 Oceanic drag

For the oceanic drag, contributions from surface drag and form drag are considered separately. In contrast to the atmospheric drag, the integral for the form drag can be solved analytically due to the lack of a stability function. The complete derivation can be found in Birnbaum (1998). The total oceanic drag τ_w results in

$$\tau_w = \rho_w c_{sd,oc} \left[1 + 0.5 \frac{h_{d,c}}{L_{i,c} + L_{w,c}} \left(\frac{1}{\kappa}\left(\ln \frac{h_{d,c}/\exp(1)}{z_{0,oc}}\right)\left(1 - \exp\left(-0.18 \frac{L_{w,c}}{h_{d,c}}\right)\right)\right)^2\right] \cdot \left|\vec{v}_{oc} - \vec{v}_i\right| \cdot \left[(\vec{v}_{oc} - \vec{v}_i)\cos(\varphi_{oc}) + \vec{k} \times (\vec{v}_{oc} - \vec{v}_i)\sin(\varphi_{oc})\right] \qquad (10.12)$$

where ρ_w represents the density of water, $c_{sd,oc} = 4 \cdot 10^{-3}$ the (surface) drag coefficient between ice and ocean, $h_{d,c}$ the draft of the ice floes, $\kappa = 0.4$ the von-Karman constant, $z_{0,oc} = 0.1$ mm the roughness length of the water surface with respect to the ocean current (similar to $z_{0,w}$ but "seen" from underwater), $\vec{v}_{oc}$ the velocity of the geostrophic ocean current, $\vec{v}_i$ the velocity of drifting ice and $\phi_{oc} = 25°$ the deviation angle between geostrophic ocean current and oceanic drag force.

10.2.2.3 Internal forces

The last term in the momentum equation denotes the internal forces in the ice, which are calculated as the divergence of the stress tensor $\vec{\vec{\sigma}}$

$$\vec{F}_\sigma = \vec{\nabla} \cdot \vec{\vec{\sigma}} \qquad (10.13)$$

Or in component notation as:

$$F_{\sigma,(j)} = \sum_i \frac{\partial}{\partial x_i} \sigma_{ij} \tag{10.14}$$

σ_{ij} represents the stress acting on a plane perpendicular to the x_i-direction towards the x_j-direction (with $x_1 = x$ and $x_2 = y$). A certain rheology is necessary to determine the components of σ_{ij}. In general, the stresses could depend on the strain, the strain rate and the overall state of the ice (e.g. ice concentration, ice strength, …). In MESIM, the viscous-plastic rheology proposed by Hibler (1979) is applied:

$$\sigma_{ij} = 2\eta\dot{\varepsilon}_{ij} + \delta_{ij}\left\{(\zeta - \eta)(\dot{\varepsilon}_{xx} + \dot{\varepsilon}_{yy}) - \frac{P}{2}\right\} \tag{10.15}$$

Here, σ_{ij} is only a function of the strain rate $\dot{\varepsilon}_{ij}$, the bulk viscosity ζ, the shear viscosity η and the hydrostatic ice pressure P. δ_{ij} is the Kronecker symbol. The strain rates are linked to the ice drift velocity components as follows:

$$\dot{\varepsilon}_{ij} = \frac{1}{2}\left(\frac{\partial u_i}{\partial x_j} + \frac{\partial u_j}{\partial x_i}\right) \tag{10.16}$$

Thus, using equation (10.16) in (10.15) and further in (10.14) and (10.6*)* shows that the momentum equation is highly non-linear and can only be solved iteratively.

The bulk and shear viscosities change with the hydrostatic ice pressure and with the total deformation of the ice:

$$\zeta = \frac{P}{2\Delta} \quad \text{and} \quad \eta = \frac{\zeta}{e^2} \tag{10.17}$$

where

$$\Delta = \sqrt{(\dot{\varepsilon}_{11}^2 + \dot{\varepsilon}_{22}^2)(1 + e^{-2}) + 4\dot{\varepsilon}_{12}^2 e^{-2} + 2\dot{\varepsilon}_{11}\dot{\varepsilon}_{22}(1 - e^{-2})} \tag{10.18}$$

The eccentricity of the elliptic yield curve is called e and is set to 2. A yield curve describes a region in the space of the stress invariants $\sigma_I = 0.5(\sigma_{xx} + \sigma_{yy})$ and $\sigma_{II} = ((\sigma_{xx} - \sigma_{yy})^2 + 4\sigma_{xy}^2)^{1/2}$ in which the combination of compressive and shear stress is subcritical so that the flow is viscous. If the stresses are strong enough to reach to the yield curve, the flow becomes plastic. Then, the strain rates decrease to zero resulting in infinite values for the viscosities.

For this transition between viscous and plastic flow, a regime function is introduced that sets an upper bound for the viscosities:

$$r_p(\Delta) = \frac{\Delta}{\Delta + \Delta_{min}} \quad \text{with } \Delta_{min} = 2 \cdot 10^{-9}\ s^{-1} \tag{10.19}$$

This regime function alters the pressure term and therefore also ζ and η such that:

$$P = P_p \cdot r_p \tag{10.20}$$

The ice strength under ideal-plastic conditions is given as

$$P_p = P^* h_i\, C(A) \quad \text{with} \tag{10.21}$$

$$C(A) = \exp\left(-C^*(1-A)\right) \tag{10.22}$$

with the mean ice thickness for all ice classes h_i and the mean ice concentration over all ice classes A. $P^* = 20000\ \mathrm{Nm}^{-2}$ is the compressive strength of compact ice of unit thickness and $C^* = 20$ a constant rating the dependence of the ice strength on the ice concentration. With this approach, the ice strength decreases linearly with decreasing ice thickness whereas a sparser ice concentration weakens the ice more considerably.

10.2.3 Numerical scheme for advection terms

With the ice drift velocity calculated from the momentum equation (10.6) the advection in the balance equations (10.1) - (10.5) can be determined. In order to keep numerical diffusion effects as small as possible, the NIC_E-scheme from Emde (1992) is used, which is described in detail in Birnbaum (1998).

10.2.4 Handling of very small ice concentrations and of convergent drift in fully ice covered cells

On one hand, the advection processes for the ice can lead to very small amounts of ice present in a certain grid cell. In MESIM sea ice concentrations below 0.01% are treated in a way that the ice coverage is set to 0 % instead and the mass of the reducted ice is conserved by increasing the ice thickness in all other grid cells in the domain.

On the other hand, advection of ice into cells which are already fully covered with ice would lead to concentrations above 100 %. In this case the ice is thought to break resulting in ridging or rafting. Therefore, the ice thickness is increased instead of the ice concentration. It is assumed that the thinner the ice, the easier it is piled up. Hence, only the thinnest ice – in ice class 1 – is assumed to undergo a rafting process, where its thickness is increased according to the law of mass conservation.

10.2.5 Formation of open water due to shear deformation

The balance equations for ice concentration (10.1) and (10.2) contain the sink terms S_{dyn} and $S_{dyn,c}$. because the ice concentration decreases if shear stresses act on the ice field resulting in the opening of leads.. This process in parameterized as the product of the total shear deformation Ψ_s with *C(A)* which is known from equation (10.22):

$$S_{dyn} = \Psi_s \cdot C(A) \tag{10.23}$$

with

$$\Psi_s = 0.5 \cdot \left(\Delta - \left|\dot{\varepsilon}_{11} + \dot{\varepsilon}_{22}\right|\right) = 0.5 \cdot \left(\Delta - \left|\nabla \cdot \vec{v}_i\right|\right) \tag{10.24}$$

This means that the reduction of the ice coverage depends on the magnitude of shear deformation acting on the ice. The factor *C(A),* however, diminishes this impact in conditions of reduced ice concentration. If the concentration drops below 75 %, the value of *C(A)* is less than 0.007. This is considered to be negligible; therefore, only concentrations above 75 % are treated in MESIM.

10.3 Thermodynamic part

The thermodynamic part of MESIM is based on the model of Maykut and Untersteiner (1971). The simplified approach of Semtner (1976), which was used by many subsequent modelers, is not applied here because it does not account for the temperature profile within the ice. This leads to inaccuracies in the surface temperature and fluxes which become relevant at the mesoscale (Birnbaum, 1998).

Using the approach of Maykut and Untersteiner (1971), storage of heat within the ice can be simulated. For this purpose, several layers in the ice are resolved and, thus, a nonlinear temperature profile can evolve. However, a transfer of heat in the horizontal direction is not considered.

In the following sections, the thermodynamic processes included in MESIM are presented. These cover the vertical growth of ice floes by freezing or their shrinkage by melting (section 10.3.1), flooding events (section 10.3.2), formation of new ice in areas of open water (section 10.3.3) and lateral melting at the edges of the ice floes (section 10.3.4).

10.3.1 Ice thickness changes due to vertical growth or shrinkage

Thickness of sea ice can change due to thermodynamic processes that only act in the vertical direction: Sea water can freeze at the bottom of the ice floe thereby increasing the ice thickness. An excess of energy at the top of the ice floe can lead to its decrease by way of

melting. The rates of freezing and melting at both the top and bottom of the ice floe are governed by the local energy balance. In order to determine the energy available for freezing or melting, the conductive heat flux into the ice has to be calculated. This flux, in turn, depends on the heat distribution in the ice which will be discussed in the following section.

10.3.1.1 Temperature profile in the ice

MESIM calculates a temperature profile at each grid cell and for each ice class employing the heat conduction equation:

$$\rho_i c_i \frac{\partial T_i}{\partial t} = \frac{\partial}{\partial z}\left(k_i \frac{\partial T_i}{\partial z} \right) + K_i I_0 \exp(-K_i z) \tag{10.25}$$

In this section, the c-index representing the ice class is ignored. Thus, T_i is the abbreviation for $T_{i,c}(z)$ which means the temperature of the ice in class c in z meter depth in the ice. The vertical coordinate z is pointing downwards with z=0 at the top of the ice. $\rho_i c_i$ stands for the volumetric heat capacity of ice, k_i for the thermal conductivity of ice, I_0 for the short wave radiation entering the top layer of the ice and $K_i = 1.5\,\mathrm{m}^{-1}$ for the absorption coefficient of short wave radiation in the ice. This equation represents the common 1-dimensional heat diffusion except for the second term on the right hand side. This describes the energy input by absorption of short wave radiation that penetrates into the ice.

In case of a snow cover on top of the ice, no short wave radiation reaches into the ice but is, instead, completely absorbed in the snow layer. The heat conduction equation for snow-covered ice therefore is simplified to

$$\rho_i c_i \frac{\partial T_i}{\partial t} = \frac{\partial}{\partial z}\left(k_i \frac{\partial T_i}{\partial z} \right) \tag{10.26}$$

Inside the snow layer, the evolution of the temperature profile $T_s(z)$ follows the equation

$$\rho_s c_s \frac{\partial T_s}{\partial t} = \frac{\partial}{\partial z}\left(k_s \frac{\partial T_s}{\partial z} \right) \tag{10.27}$$

with the volumetric heat capacity of snow $\rho_s c_s$ and the thermal conductivity of snow k_s. z in snow covered conditions is set to zero at the top of the snow layer so that the ice is located at $h_s \le z \le h_s + h_i$.

At the interface between snow and ice, two conditions have to be fulfilled: The temperatures and heat fluxes in the snow and the ice have to be equal

$$T_s(h_s) = T_i(h_s) \tag{10.28}$$

as heat cannot be stored at the interface.

$$k_s \left.\frac{\partial T_s}{\partial z}\right|_{h_s} = k_i \left.\frac{\partial T_i}{\partial z}\right|_{h_s} \tag{10.29}$$

Salinity and temperature dependend parameters

Most of the physical parameters needed in the heat conduction equations (10.25) - (10.27) are not constants but depend on the salinity of the sea ice and/or its temperature at the respective depth. In MESIM, two different salinity profiles are assumed: For first year ice (i.e. ice in classes 1 and 2), the so called “C-profile” by Eicken (1992) is applied which reads

$$S(Z) = \left(11.63 - 18.46\,Z - 1.53\,Z^2 + 18.78\,Z^3\right)\ [\text{ppt}] \tag{10.30}$$

with S as salinity of sea ice in any ice class c (index omitted in this section) and Z as the relative depth in the ice ranging from 0 at the top to 1 at the bottom. For ice thicker than 40 cm (classes 3 and 4) the profile is assumed to follow the one proposed by Jin et al. (1994) for multiyear ice:

$$S(Z) = \left(2.785\,Z + 1.984\,Z^4\right)\ [\text{ppt}] \tag{10.31}$$

These salinity profiles are converted from relative to absolute depth values. Afterwards, they can be used to calculate profiles of the volumetric heat capacity $\rho_i c_i$ and the thermal conductivity k_i following Maykut and Untersteiner (1971):

$$(\rho_i c_i)(z) = (\rho_i c_i)_f + \frac{\gamma\, S(z)}{\left(T_i(z) - T_{melt,i}\right)^2} \tag{10.32}$$

$$k_i(z) = k_{i,f} + \frac{\beta\, S(z)}{T_i(z) - T_{melt,i}} \tag{10.33}$$

S(z) and $T_i(z)$ denote the salinity and the ice temperature at the depth z. All other parameters are constants and are given in Table 5. In order to avoid singularities due to a denominator close to zero, $T_{melt,i}$ is set to $T_i(z)+0.1$ K in case $T_i(z)$ exceeds 272.95 K.

Table 5: Constants used in calculation of salinity dependend parameters.

Variable	Value	Meaning
$(\rho_i c_i)_f$	$1.884 \cdot 10^6$ Jm^{-3} K^{-1}	Volumetric heat capacity of fresh ice
γ	$1.716 \cdot 10^7$ Jm^{-3} K^{+1} ppt^{-1}	–
$k_{i,f}$	2.035 W m^{-1} K^{-1}	Thermal conductivity of fresh ice
β	0.1172 W m^{-1} ppt^{-1}	–
$T_{melt,i}$	273.05 K	Melting point of sea ice
$T_{melt,s}$	273.15 K	Melting point of snow

The thermal properties of snow do not depend on salinity but only on the temperature of the snow T_s. They are calculated following Ebert and Curry (1993) as

$$(\rho_s c_s)(z) = \rho_s(z) \cdot (92.88 + 7.364\ T_s(z)) \tag{10.34}$$

$$k_s(z) = 2.845 \cdot 10^{-6} \cdot \rho_s^2(z) + 2.7 \cdot 10^{-4} \cdot 2^{(T_s(z)-233)/5} \tag{10.35}$$

The density of snow ρ_s is also temperature dependent. MESIM uses following assumption:

$$\rho_s = \begin{cases} 330 \ \text{kg m}^{-3} & \text{if} \quad T_s < T_{melt,s} \\ 450 \ \text{kg m}^{-3} & \text{if} \quad T_s = T_{melt,s} \end{cases} \tag{10.36}$$

with the melting temperature of snow $T_{melt,s}$=*273.15* K. Once all of these thermal parameters are determined for each discrete depth, the heat conduction equation can be solved

Boundary conditions for the heat transfer equation

In order to solve the heat conduction equations in snow and ice (10.25) - (10.27), boundary conditions along the snow-ice interface (10.28), (10.29) and the collective upper and lower boundaries are needed. At the bottom – the interface between ice and sea water – the Dirichlet boundary condition (constant values) is applied such that the temperature of the ice has to meet the freezing point of sea water T_f, which is constantly set to

$$T_{i,bot} = T_f = 271.35 \ \text{K} \tag{10.37}$$

At the top of the snow (if present) or the ice layer the boundary condition is of the Neumann type (constant gradients) and states that the temperature gradient at the top is set to the conductive heat flux into the ice Q_c divided by the thermal conductivity.

$$\left.\frac{\partial T_{s/i}}{\partial z}\right|_{z=0} = \frac{Q_c}{k_{s/i}} \tag{10.38}$$

This conductive heat flux is calculated as residuum of all energy fluxes at the snow/ice surface, namely the net short wave radiation SW_{net}, the net long wave radiation LW_{net}, the sensible heat flux Q_s and the latent heat flux Q_l.

$$Q_c = -\left(SW_{net} + LW_{net} - Q_s - Q_l\right) \tag{10.39}$$

With these boundary conditions, the temperature profile in the ice can be determined using the Crank-Nicholson scheme.

10.3.1.2 Energy budget at the top of the ice - melting

If the resulting temperature at the uppermost ice level increases above the melting point of sea ice $T_{melt,i}$, the ice thickness must change due to melting. However, prior to this, a new temperature profile has to be computed because the temperature at the air–ice/snow interface can not exceed the melting point before the ice has melted completely. This means that $T_i(z=0)=T_{sur}$ is set to $T_{melt,i}$ as a Dirichlet boundary condition and the heat conduction equation is solved anew. If snow lies on top of the ice, the temperature profile is newly calculated again with the old Neumann condition. From the resulting temperature gradient between the first and the second level, the conductive heat flux into the ice is recalculated:

$$Q_c = k_{s/i}\,\frac{T_1 - T_{sur}}{\Delta z} \tag{10.40}$$

Q_c is needed to determine the thickness change of the ice which is done utilizing the energy balance equation at the ice or snow surface.

$$-L_{fus,s/i}\,\frac{\partial\left(h_i + h_s\right)}{\partial t} = SW_{net} + LW_{net} - Q_s - Q_l + Q_c \qquad \text{if} \quad T_{sur} = T_{melt,i} \tag{10.41}$$

Thus, any residual flux will lead to a melting, firstly of the snow cover and subsequently of the ice. For snow melt, a value of $1.097 \cdot 10^8$ $\mathrm{Jm^{-3}}$ for the volumetric heat of fusion $L_{fus,s}$ is chosen while for ice $L_{fus,i} = 3.014 \cdot 10^8$ $\mathrm{Jm^{-3}}$ is used. By integrating equation (10.41) in time the snow and ice thickness changes can be predicted once the fluxes at the right hand side are known. Their determination will be covered in the next subsections. Please

note that the radiation fluxes are recalculated with different parameterizations in the ice model even if they were already computed by the atmospheric METRAS module before.

Short wave radiation

The amount of short wave radiation absorbed by the surface depends on the surface characteristics, namely the albedo α_i for ice surfaces, α_s for snow surfaces and α_w for water surfaces. Due to the translucency of ice the net short wave radiation over ice is further deceased by the factor $(1-i_0)$ where i_0 specifies the amount of sun light which is penetrating into the ice. Summarized, the net short wave radiation at the surface can be written as

$$SW_{net} = \begin{cases} (1-\alpha_s) SW_{\downarrow} & \text{for snow covered surfaces} \\ (1-\alpha_i)(1-i_0) SW_{\downarrow} & \text{for ice covered surfaces} \\ (1-\alpha_w) SW_{\downarrow} & \text{for water surfaces} \end{cases} \tag{10.42}$$

The albedo in MESIM may depend on ice and snow thicknesses as well as on the incidence angle of the sun light and the cloud cover. Its values in the different cases are outlined in Table 5.2 in Birnbaum (1998).

The fraction of penetrating radiation i_0 is parameterized as

$$i_0 = 0.18(1-C) + 0.35 \cdot C \tag{10.43}$$

with *C* being the cloud cover fraction. To determine *C*, the model examines the air column above the particular ice/snow/water cell. If the water vapour pressure exceeds the saturation pressure at any height clouds are assumed to be present and *C* is set to 1. Otherwise, *C* is assigned the value 0.

Also, the parameterization of the incoming short wave radiation relies on *C*.

$$SW_{\downarrow} = \begin{cases} \dfrac{1368 \cdot (\cos(\theta))^2}{1.2 \cdot \cos(\theta) + (1+\cos(\theta)) \cdot e_{2m} \cdot 10^{-5} + 0.0455} & \text{if } C = 0 \\ \dfrac{(53.5 + 1274.5 \cdot \cos(\theta)) \sqrt{\cos(\theta)}}{1 + 0.139 \cdot (1 - 0.9435 \cdot \alpha_{s/i/w}) \cdot \tau_c} & \text{if } C = 1 \end{cases} \tag{10.44}$$

In cloud free conditions $SW_{\downarrow}$ only depends on the incidence angle Θ of the sun light and on the water vapour pressure in 2 m height e_{2m}. If, however, the sky is overcast, knowledge about the surface albedo and the optical thickness τ_c is additionally required.

τ_c is governed by the vertical thickness H_c of all clouds in the air column. By employing the extinction coefficient $K_c = 42\ \mathrm{km}^{-1}$ this can be converted into optical thickness:

$$\tau_c = K_c \cdot H_c \tag{10.45}$$

Once all of these parameters are plugged into equation (10.42), the net shortwave radiation absorbed at the surface can be determined.

Long wave radiation

The net long wave radiation is the sum of the incoming and outgoing parts.

$$LW_{net} = LW_{\downarrow} + LW_{\uparrow} \tag{10.46}$$

The incoming long wave radiation emitted by the atmosphere is calculated from the air temperature in 2 m height $T_{a,2m}$ for clear sky conditions and from the cloud-base temperature T_c otherwise.

$$LW_{\downarrow} = \begin{cases} \varepsilon_a\ \sigma T_{a,2m}^4 & \text{if } C = 0 \\ \varepsilon_c\ \sigma T_c^4 & \text{if } C = 1 \end{cases} \tag{10.47}$$

The respective emissivities of air and clouds are given as

$$\varepsilon_a = 0.67 + 0.05\sqrt{e_{2m} \cdot 10^{-2}} \qquad \text{and} \qquad \varepsilon_c = 1 \tag{10.48}$$

with the water vapour pressure at 2 m height e_{2m}.

The outgoing long wave radiation follows the Stefan-Boltzmann law stating that

$$LW_{\uparrow} = -\varepsilon_{sur}\sigma T_{sur}^4 \tag{10.49}$$

where T_{sur} respresents the surface temperature of snow, ice or water. The respective emissivity ε_{sur} is set to 0.99 for snow and to 0.97 for ice and water.

Sensible heat flux between atmosphere and ice

The third flux involved in the surface energy balance is the sensible heat flux between ice and atmosphere. It is calculated analogously to that on land surfaces from the friction velocity $u_{*,i}$ and the scaling temperature $\theta_{*,i}$ over the ice.

$$Q_s = -\rho_0 c_p u_{*,i} \theta_{*,i} \tag{10.50}$$

Here ρ_0 denotes the mesoscale density of the air and c_p the specific heat capacity under constant pressure. $u_{*,i}$ and $\theta_{*,i}$ are determined as shown in Section 3.3 assuming a constant roughness length over ice of 1 mm.

Latent heat flux between atmosphere and ice

The flux of latent heat from the ice into the atmosphere reads:

$$Q_l = -\rho_0 l_{21} u_{*,i} q_{*,i} \tag{10.51}$$

As with the sensible heat flux, $u_{*,i}$ represents the friction velocity over ice and $q_{*,i}$ the scaling value for the specific humidity over the ice, both calculated as described in section 3.3.1. The parameter $l_{21} = 2.5 \cdot 10^6 \ \mathrm{J \cdot kg^{-1}}$ gives the specific latent heat of vaporisation.

10.3.1.3 Energy budget at the bottom of the ice – freezing or melting

While the energy budget at the top of the ice (Section 10.3.1.2) is crucial for top-ice melting events, the energy budget at the bottom of the ice controls freezing or melting at the ice-floe base. It is determined by the sensible heat flux from the ocean to the ice–sea interface $Q_{s,bot}$ and the conductive heat flux from the surface into the ice $Q_{c,bot}$. Their difference controls the changes in snow and ice thickness as follows:

$$-L_{fus,s/i} \left. \frac{\partial (h_s + h_i)}{\partial t} \right|_{z=h_s+h_i} = Q_{s,bot} - Q_{c,bot} \tag{10.52}$$

Any residual flux is converted into a thickness change via the volumetric heat of fusion. If the right hand side of equation (10.52) is negative, the ice grows, thereby releasing $L_{fus,i} = 3.014 \cdot 10^8 \ \mathrm{Jm^{-3}}$. If, in contrast, more energy is transported towards the interface than conducted away, the excess energy melts the ice. Only in cases where the whole ice floe deliquesces, does the snow cover begin to melt, consuming $L_{fus,s} = 1.097 \cdot 10^8 \ \mathrm{Jm^{-3}}$.

The sensible heat flux from the ocean to the ice is calculated from the friction velocity between ice and ocean $u_{*,oc}$ and the temperature difference between water and the ice base:

$$Q_{s,bot} = \rho_w c_{p,w} \cdot C_{h,w} \cdot u_{*,oc} \cdot (T_w - T_{i,bot}) \tag{10.53}$$

T_w gives the temperature of the surface water layer and $T_{i,bot}$ the temperature at the ice–ocean interface, which is constrained to the freezing point of sea water T_f. The constants are the density of sea water $\rho_w = 1026 \ \mathrm{kg\,m^{-3}}$, the specific heat capacity of sea water $c_{p,w} = 3980 \ \mathrm{J\,kg^{-1}\,K^{-1}}$ and a transfer coefficient for sensible heat $C_{h,w} = 6 \cdot 10^{-3}$. $u_{*,oc}$. has to be determined by an iterative process from

$$\left|\vec{v}_i - \vec{v}_{oc}\right| = \left|\frac{u_{*,oc}}{\kappa}\left[\ln\left(\frac{u_{*,oc}}{f \cdot z_{0,bot}}\right) - B_1 - i \cdot B_2\right]\right| \tag{10.54}$$

where $\vec{v}_i$ stands for the ice drift velocity, $\vec{v}_{oc}$ for the velocity of the geostrophic ocean current, κ for the von-Karman constant, f for the Coriolis parameter and $z_{0,bot} = 0.1\text{m}$ for the roughness length at the bottom side of the ice floe respective to sea water. The constants B_1 and B_2 are set to 2.0 and i represents the imaginary unit. In order to receive $u_{*,oc}$ equation (10.54) is squared yielding a polynomial equation in $u_{*,oc}$ and $\ln(u_{*,oc})$, which is numerically solved using Newton's method. The number of iterations carried out is fixed to three.

The conductive heat flux from the ice–ocean interface into the ice is determined from the ice temperature gradient at the bottom of the floe:

$$Q_{c,bot} = k_i \left.\frac{\partial T_i}{\partial z}\right|_{h_s + h_i} \tag{10.55}$$

10.3.2 Changes in thickness of snow and ice due to flooding

Besides the vertical growing or melting of the ice due to energy deficits or surpluses, the ice and snow thicknesses may also change in flooding events. If there is more snow load on top of the ice than the ice floe can bear with its buoyancy, the snow–ice interface is pushed below the water surface and sea water will seep into the snow. In this case, the model assumes – currently regardless of conservation of energy – that the snow–water mixture freezes instantaneously to sea ice. The changes in ice thickness h_i and snow thickness h_s can be determined from Archimedes' principle to be

$$\Delta h_s = -\Delta h_i = h_i - \left(\frac{\rho_i h_i + \rho_s h_s}{\rho_w}\right) \tag{10.56}$$

The effect is driven by differences in the respective densities of sea water $\rho_w = 1026\ \text{kg m}^{-3}$, sea ice $\rho_i = 900\ \text{kg m}^{-3}$ and snow $\rho_s = 330\ \text{kg m}^{-3}$.

10.3.3 Changes in ice cover due to new ice formation

New ice can grow at all water surfaces in the model area. These include cells which consist only of water as well as the open-water part of cells with a partly ice cover. In this case, the new ice formation is calculated separately for each ice class.

First, the total heat flux into the surface water layer is calculated as a residuum of shortwave incoming radiation $SW_{\downarrow}$, net longwave radiation LW_{net}, the sensible heat flux Q_s and the latent heat flux Q_l.

$$Q_{w,l} = (1-i_w)(1-\alpha_w)\,SW_{\downarrow} + LW_{net} - Q_s - Q_l \tag{10.57}$$

α_w is the albedo of the water surface and $(1-i_w)$ gives the fraction of the shortwave radiation that is absorbed by the surface water layer. This layer is defined as the water mass reaching to the depth of the ice-floe draft $h_{d,c}$. i_w can be estimated by an empirical formula of Maykut and Perovich (1987):

$$(1-i_w)(1-\alpha_w) = a_1 + a_2 \cdot h_{d,c} \tag{10.58}$$

The values of a_1 and a_2 depend on the cloudiness. So, a_1=0.5676 and a_2=0.1046 m^{-1} for a cloud free sky, and a_1=0.3938 and a_2=0.1208 m^{-1} in overcast conditions.

If the resulting flux $Q_{w,l}$ is negative, energy is extracted from the water. The cooling of the surface water layer can be determined as

$$T'_{w,l} = T_w^{n-1} + \left(\frac{Q_{w,l}\,\Delta t}{\rho_w c_w\, h_{d,c}} \right) \tag{10.59}$$

with the volumetric heat capacity of sea water $\rho_w c_w = 4.19 \cdot 10^6$ J m^{-3} K^{-1}, the depth of ice-floe draft $h_{d,c}$ and the water temperature at the previous time step T_w^{n-1}. $T'_{w,l}$ is only a temporary variable and the value of the new temperature is not stored for the next time step.

New ice can form for surface layer temperatures $T'_{w,l}$ below the freezing point T_f = 271.35 K. The energy deficit available for freezing water $Q_{w,l}$ is reduced when the water temperature at the previous time step was above the freezing point. In this case, the water mass firstly has to be cooled down to T_f before ice can begin to grow. $Q_{w,l}$ is updated as follows:

$$Q'_{w,l} = Q_{w,l} + \rho_w c_w\, h_{d,c}\, \frac{T_w^{n-1} - T_f}{\Delta t} \tag{10.60}$$

With this remaining energy deficit, the thickness of the new-ice layer covering the complete water surface dedicated to surfrathil(c) is determined as

$$h'_{ni,c} = -\frac{Q'_{w,l}\,\Delta t}{L_{fus,i}} \tag{10.61}$$

where $L_{fus,I}$ = 3.014·10^8 J m^{-3} is the latent heat of fusion per unit volume.

In a wavy ocean, the growing ice is subjected to wind. Hence, a uniform ice layer is unlikely to occur. Rather, small ice crystals form which float in the upper layer of the ocean (e.g. frazil ice) until they become numerous enough to conglomerate to pieces of ice (e.g. pancake ice). To simulate this process, the newly formed layered ice is being drifted and compressed instantaneously at the same time step. The speed of the new ice $\left|\vec{v}_i^{icl=1}\right|$ drifting relatively to the "old" ice with its speed $\left|\vec{v}_i\right|$ is calculated as:

$$\left|\vec{v}_i^{icl=1}\right| = \sqrt{\frac{\rho_0 u_{*,w}^2}{\rho_w c_{sd,oc}}} - \left|\vec{v}_i\right| \tag{10.62}$$

where $u_{*,w}$ is the friction velocity for water surfaces, ρ_0 the density of air, ρ_w the density of water, $c_{sd,oc} = 4 \cdot 10^{-3}$ the surface drag coefficient between ice and ocean and $\left|\vec{v}_i\right|$ the ice drift speed which is the same for all ice classes. Within one timestep Δt, the ice can drift the distance

$$\Delta x = \left|\vec{v}_i^{icl=1}\right| \cdot \Delta t \tag{10.63}$$

If Δx is less than the distance between the ice floes $L_{w,c}$ the ice is only able to free a part of the water surface and will be pushed together in the left over area $L_{w,c} - \Delta x$. The thickness of this accumulated ice $h_{ni,c}$ is determined for each ice class using the mass conservation law while redistributing the ice, so that

$$h_{ni,c} = h'_{ni,c} \frac{L_{w,c}}{L_{w,c} - \Delta x} \tag{10.64}$$

For values of $h_{ni,c}$ exceeding the upper bound of ice in class 1 (10 cm) a restriction for Δx is applied as follows: The new ice thickness $h_{ni,c}$ is fixed to 10.01 cm and the model calculates in reverse the drifting distance Δx necessary to yield this thickness:

$$\Delta x = L_{w,c} - \frac{h'_{ni,c} \cdot L_{w,c}}{0.1001 \ \text{m}} \tag{10.65}$$

After this procedure is done for all 4 ice classes if present, the new-ice surfaces that grew between the ice floes are mapped into ice class 1. All thicknesses of the new-ice areas and that of the previous class 1 area are averaged to build the new value for $h_{i,1}$.

For the case that $\Delta x > L_{w,c}$, which means that the new ice would drift further than there is space between the ice floes, the action of the model depends on the ice class in which this circumstance occurs. If it happens for the ice class 1 (ice below 10 cm thickness), the

newly formed ice is completely removed from the water surface and stacked on top of the already existing ice. The new ice thickness of class 1 results as

$$h_{i,1} = h_{i,1}^{n-1} + h'_{ni,1} \frac{L_{w,1}}{L_{i,1}} \tag{10.66}$$

If the drift distance Δx exceeds the floe spacing in any class other than c=1, the model applies the same scheme as used for new ice thicker than 10 cm: The value of $h_{ni,c}$ is set to 10.01 cm and Δx is recalculated to match with it.

For cells in which there is only water and no ice, the procedure for determining the new-ice formation differs slightly from the one shown above: Mainly, the depth of the surface water layer is not dependent on the ice-floe draft, but is instead fixed to 30 m, the assumed depth of the mixing layer. Thus, the calculation of i_w can be omitted because it is assumed that all shortwave radiation is absorbed by the 30 m thick water column. The heat flux from the deeper ocean to the surface layer could be taken into account in equation (10.56) but it is set to 0 in the current model version. Furthermore, the drift of the newly formed ice is only evaluated if the model is run in the thermodynamic-only mode.

Consequently, for only-water cells and simulations including dynamic processes, the new ice, firstly, covers the whole grid cell with a thin ice layer of thickness. $h'_{ni,c}$. Drift of this ice is then applied in the next time step. The last difference to the case with ice—water-mixed cells is that the water temperature is actually able to decrease because the new temperature calculated with equation (10.59) is stored and used at the next time step.

10.3.4 Changes in ice cover due to lateral melting

The second thermodynamic process which changes the ice coverage is triggered if the energy budget is positive. In cases where both ice and water are present in a grid cell, the possibly warm water can lead to melting at the flanks of the ice floes. To calculate the resulting change in the lengths of the floes, MESIM applies the parameterisation by Josberger (1979). He proposed that the reduction of the ice floe length depends on the temperature difference between the ocean T_w and the freezing point T_f as follows

$$\left.\frac{\partial L_{i,c}}{\partial t}\right|_{lat\_melt} = -2m_1 \left(T_w - T_f\right)^{m_2} \tag{10.67}$$

The constants are chosen to be $m_1 = 2.85 \cdot 10^{-7}\ \mathrm{m\,s^{-1}}$ and $m_2 = 1.36$. The spacing between the floes increases according to the decrease of floe length, given by

$$\left.\frac{\partial L_{w,c}}{\partial t}\right|_{lat\_melt} = -\left.\frac{\partial L_{i,c}}{\partial t}\right|_{lat\_melt} = 2m_1\left(T_w - T_f\right)^{m_2} \tag{10.68}$$

From the new values of $L_{i,c}$ and $L_{w,c}$ the new ice concentration of the respective ice class c can be calculated:

$$A_c = \frac{L_{i,c}}{L_{i,c} + L_{w,c}} \tag{10.69}$$

10.4 Numerical grids

Horizontal grid

In the horizontal direction, MESIM works on an Arakawa-B grid. Both components of the ice drift velocity, u_i and u_j, are defined at the same location but shifted by half a grid spacing in both the east and north directions compared to the scalar variables.

Vertical grid

In the vertical direction, variables are also defined at different locations as can be seen from Figure 10.1. This figure shows a vertical profile through snow and ice. Every rectangle represents one layer: nx3s+1 layers in the snow and nx3si+1 in total. Most of them have the same thickness $dz_{si}(1)=\ldots=dz_{si}(nx3si-1)$ except for the uppermost snow layer and the lowermost ice layer, which may be arbitrarily thick. The depths at which the layer borders are located are given by z_{si}. Variables like ice and snow temperature, density or heat conductivity, named X in Figure 10.1, are also defined at the layer borders. For some applications, however, values at the middle of the layers, X_m, are required. Their indexing can be seen from the figure.

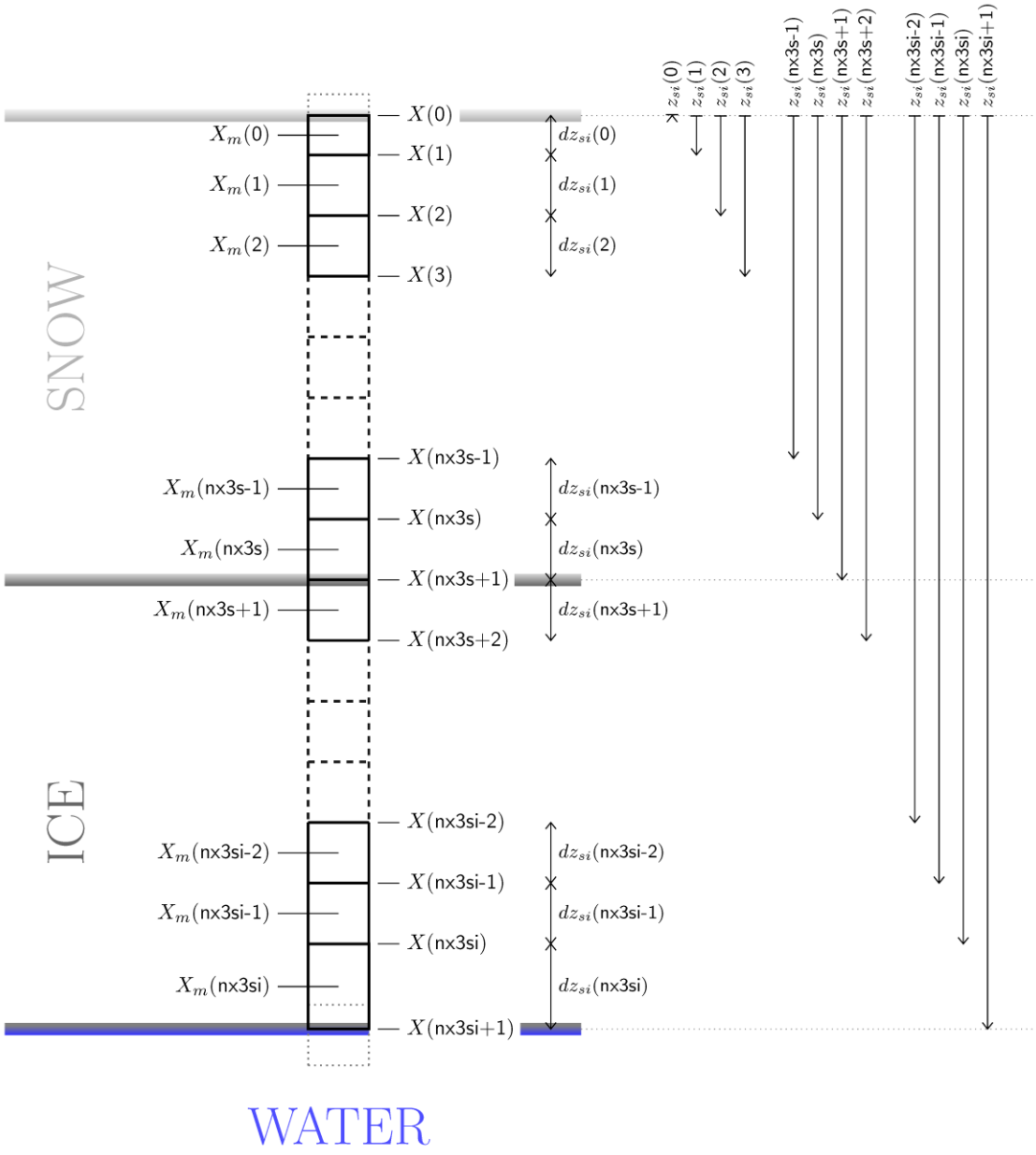

Figure 10.1: Vertical grid in ice and snow: Definition locations of variables X and X_m, the layer thicknesses dz_{si} and the depth of the layer borders z_{si}.

A. Mathematical hints

A.1 Model equations and coordinate transformation

In this appendix the mathematical fundamentals of coordinate transformations are presented and are derived in a non-orthogonal, curvilinear and time independent coordinate system. The fundamentals of coordinate transformation and tensor analysis are described in detail by Dutton (1976), Spiegel (1982) and Wrede (1972). To transform the model equations into a non-orthogonal, curvilinear and time independent coordinate system it is indispensable to previously define the basis vectors of the coordinate system. Two systems of basis vectors, independent from each other, exist. The covariant basis vectors $\dot{q}_i$ are tangent to the coordinate axis $\dot{x}^i$ and can be defined by

$$\dot{q}_i = \frac{\partial r}{\partial \dot{x}^i} \tag{A.1}$$

where r denotes the position vector. The contravariant basis vectors $\dot{q}^i$ are perpendicular to the surfaces $\dot{x}^i = \text{const.}$ and are defined by

$$\dot{q}^i = \nabla \dot{x}^i \tag{A.2}$$

Both systems of basis vectors in a nonorthogonal, curvilinear and time independent coordinate system are not systems of unit vectors. Both direction and magnitude vary in space. The components of the covariant and contravariant metric tensor can be calculated from the products $\dot{q}_i \cdot \dot{q}_j = \dot{g}_{ij}$ and $\dot{q}^i \cdot \dot{q}^j = \dot{g}^{ij}$. In an orthogonal coordinate system both covariant and contravariant basis vectors are identical and, for $i \neq j$, the components $\dot{g}_{ij}$ and $\dot{g}^{ij}$ of the metric tensor become zero. In a nonorthogonal system $\dot{g}_{ij}$ and $\dot{g}^{ij}$ are different from zero. If $i = j$, the product of covariant and contravariant basis vectors $\dot{q}_i \cdot \dot{q}^j$ is 1, otherwise it is zero. Beyond basis vectors and metric tensor the determinant $|\dot{g}_{ij}| := \dot{g}$ of the covariant metric tensor as well as the Christoffel symbol $\dot{\Gamma}^i_{jk}$ are necessary to derive the model equations in any coordinate system. $\dot{\Gamma}^i_{jk}$ is defined by:

$$\begin{aligned} \dot{\Gamma}^i_{j,k} &:= \frac{1}{2}\, \dot{g}^{il} \left\{ \frac{\partial \dot{g}_{jl}}{\partial \dot{x}^k} + \frac{\partial \dot{g}_{kl}}{\partial \dot{x}^j} - \frac{\partial \dot{g}_{jk}}{\partial \dot{x}^l} \right\} \\ &= \frac{\partial \dot{x}^i}{\partial x^l} \frac{\partial^2 x^l}{\partial \dot{x}^j \partial \dot{x}^k} \end{aligned} \tag{A.3}$$

Any vector Ψ in a non-orthogonal curvilinear coordinate system can be expressed by use of the basis vectors $\dot{q}_i$ and $\dot{q}^i$. The covariant vector components (subscript) are defined by $\dot{\Psi}_i = \dot{q}_i \Psi$ and the contravariant components (superscript) by $\dot{\Psi}^i = \dot{q}^i \Psi$

With the relations above all quantities are defined, which are necessary to derive the model equations (2.1) to (2.3) in a non-orthogonal curvilinear and time independent coordinate system. If not explicitly mentioned, the summation convention is used in all following equations. The equations of motion (2.1) are transferred to equations of momentum by use of the continuity equation (2.3). Using this formulation, it is unnecessary to solve the coupled system of differential equations (2.1) and (2.3), because the balance equation of momentum alone guarantees conservation of momentum if suitable numerical schemes are applied (Roache, 1982). The balance equations are derived for the contravariant components $\dot{u}^j$ of the velocity vector:

$$\frac{\partial \rho\sqrt{\dot{g}}\dot{u}^i}{\partial t} + \frac{\partial \rho\sqrt{\dot{g}}\dot{u}^k\dot{u}^i}{\partial \dot{x}^k} + \rho\sqrt{\dot{g}}\dot{u}^k\dot{u}^j\dot{\Gamma}^i_{jk} = -\rho\sqrt{\dot{g}}g^{ij}\frac{\partial p}{\partial \dot{x}^j} - \rho\sqrt{\dot{g}}g^{ij}\frac{\partial \Phi}{\partial \dot{x}^j} - 2\rho\dot{\varepsilon}_{ijk}\dot{\Omega}_j\dot{g}_{kl}\dot{u}^l \qquad \text{(A.4)}$$

$\dot{\Omega}_j$ denotes the contravariant components of the angular velocity of the earth. For cyclic indices $\dot{\varepsilon}_{ijk}$ becomes +1, otherwise -1 and $\dot{\varepsilon}_{ijk} = 0$, if one index appears twice.

The continuity equation can be written in a non-orthogonal curvilinear coordinate system:

$$\frac{\partial \rho\sqrt{\dot{g}}}{\partial t} + \frac{\partial \rho\sqrt{\dot{g}}\dot{u}^i}{\partial \dot{x}^i} = 0 \qquad \text{(A.5)}$$

The balance equation for any scalar variable χ in a non-orthogonal curvilinear coordinate system can be derived to:

$$\frac{\partial \rho\sqrt{\dot{g}}\chi}{\partial t} + \frac{\partial \rho\sqrt{\dot{g}}\dot{u}^i\chi}{\partial \dot{x}^i} = \rho\sqrt{\dot{g}}Q_\chi \qquad \text{(A.6)}$$

A.2 Equations in terrain-following coordinates

The equations (A.4) to (A.6) can be formulated in the coordinate system $\dot{x}$ by use of the components of the metric tensor and the Christoffel symbol. Both can be calculated from the basis vectors following (A.1) and (A.2). The transformation rules between the coordinates $\dot{x}^1, \dot{x}^2, \dot{x}^3$ of the terrain - following coordinate system $\dot{x}$ (Section 2.2) and coordinates x, y, z of the orthogonal Cartesian system X are defined by:

$$\begin{aligned} \dot{x}^1 &= \dot{x}^1(x) && (a)\\ \dot{x}^2 &= \dot{x}^2(y) && (b)\\ \dot{x}^3 &= \dot{x}^3(\eta) = z_t\,\frac{z - z_s(x,y)}{z_t - z_s(x,y)}) && (c) \end{aligned} \qquad \text{(A.7)}$$

The relation between coordinates x,y,z of the coordinate system X and $\dot{x}^1,\dot{x}^2,\dot{x}^3$ of the coordinate system $\dot{X}$ follows:

$$\begin{aligned} x &= x(\dot{x}^1) && \text{(a)} \\ y &= y(\dot{x}^2) && \text{(b)} \\ z &= \eta(\dot{x}^3)\cdot\frac{z_t - z_s(x(\dot{x}^1),y(\dot{x}^2))}{z_t} + z_s(x(\dot{x}^1),y(\dot{x}^2)) && \text{(A.8)} \\ &= z(\dot{x}^1,\dot{x}^2,\dot{x}^3) && \text{(c)} \end{aligned}$$

The covariant basis vectors $\dot{q}_i$, which are tangential to the coordinate axis (Figure 2.1), are derived from equation (A.*1*):

$$\begin{aligned} \dot{q}_1 &= \frac{\partial x}{\partial \dot{x}^1} i + \frac{\partial z}{\partial \dot{x}^1} k = A\,(i + D\,F k) && (a) \\ \dot{q}_2 &= \frac{\partial y}{\partial \dot{x}^2} j + \frac{\partial z}{\partial \dot{x}^2} k = B\,(j + E\,F\,k) && (b) \\ \dot{q}_3 &= \frac{\partial z}{\partial \dot{x}^3} = C\,G k && (c) \end{aligned} \qquad \text{(A.9)}$$

In (A.9) i, j, k denote the basis vectors of the Cartesian system X, tangential to the west-east, south-north and vertical direction, respectively. The contravariant basis vectors are perpendicular to the coordinate surfaces (Figure 2.1) and can be derived from (A.*2*):

$$\begin{aligned} \dot{q}^1 &= \frac{\partial \dot{x}^1}{\partial x} i = \frac{1}{A} i && (a) \\ \dot{q}^2 &= \frac{\partial \dot{x}^2}{\partial y} j = \frac{1}{B} j && (b) \\ \dot{q}^3 &= \frac{\partial \dot{x}^3}{\partial x} i + \frac{\partial \dot{x}^3}{\partial y} j + \frac{\partial \dot{x}^3}{\partial z} k = \frac{1}{C\,G}\{k - F\,(D i + E j)\} && (c) \end{aligned} \qquad \text{(A.10)}$$

The transformation coefficients A to G stand for the spatial derivatives $\partial\dot{x}^i/\partial x^j$, $\partial x^i/\partial\dot{x}^j$ and are defined by (A.11). They are used in the discretized model equations (Appendix B.1).

$$
\begin{aligned}
A(\dot{x}^1) &:= \frac{\partial x}{\partial \dot{x}^1} && \text{(a)}\\
B(\dot{x}^2) &:= \frac{\partial y}{\partial \dot{x}^2} && \text{(b)}\\
C(\dot{x}^3) &:= \frac{\partial \eta}{\partial \dot{x}^3} && \text{(c)}\\
D(\dot{x}^1,\dot{x}^2) &:= \frac{\partial z_s}{\partial x} && \text{(d)}\\
E(\dot{x}^1,\dot{x}^2) &:= \frac{\partial z_s}{\partial y} && \text{(e)}\\
F(\dot{x}^3) &:= 1-\frac{\eta}{z_t} && \text{(f)}\\
G(\dot{x}^1,\dot{x}^2) &:= \frac{z_t - z_s}{z_t} && \text{(g)}\\
\alpha^*(\dot{x}^1,\dot{x}^2,\dot{x}^3) &:= \sqrt{g}\\
&= (\partial x / \partial \dot{x}^1)\cdot(\partial y / \partial \dot{x}^2)\cdot(\partial z / \partial \dot{x}^3) && \text{(h)}\\
&= A\cdot B\cdot C\cdot G
\end{aligned}
\qquad \text{(A.11)}
$$

The balance equations of momentum in the coordinate system $\dot{x}$ are written:

$$
\begin{aligned}
\frac{\partial \rho \alpha^* \dot{u}^1}{\partial t} \quad &+ \quad \frac{\partial \rho \alpha^* \dot{u}^i \dot{u}^1}{\partial \dot{x}^i} + \bar{\rho} \alpha^* (\dot{u}^1)^2 \frac{\partial \dot{x}^1}{\partial x} \frac{\partial^2 x}{(\partial \dot{x}^1)^2} \\
&= \quad -\alpha^* \frac{\partial \dot{x}^1}{\partial x} \left[\frac{\partial \dot{x}^1}{\partial x} \frac{\partial p}{\partial \dot{x}^1} + \frac{\partial \dot{x}^3}{\partial x} \frac{\partial p}{\partial \dot{x}^3} \right] \\
&\quad + f \rho \alpha^* \dot{u}^2 \frac{\partial y}{\partial \dot{x}^2} \frac{\partial \dot{x}^1}{\partial x} - f' \cos\xi \frac{\partial \dot{x}^1}{\partial x} \left\{ \rho \alpha^* \dot{u}^1 \frac{\partial z}{\partial \dot{x}^1} + \rho \alpha^* \dot{u}^2 \frac{\partial z}{\partial \dot{x}^2} + \rho \alpha^* \dot{u}^3 \frac{\partial z}{\partial \dot{x}^3} \right\} \qquad (a) \\
\frac{\partial \rho \overset{*}{\alpha} \dot{u}^2}{\partial t} \quad &+ \quad \frac{\partial \rho \alpha^* \dot{u}^j \dot{u}^2}{\partial \dot{x}^i} + \bar{\rho} \alpha^* (\dot{u}^2)^2 \frac{\partial \dot{x}^2}{\partial y} \frac{\partial^2 y}{(\partial \dot{x}^2)^2} \\
&= \quad -\alpha^* \frac{\partial \dot{x}^2}{\partial y} \left[\frac{\partial \dot{x}^2}{\partial y} \frac{\partial p}{\partial \dot{x}^2} + \frac{\partial \dot{x}^3}{\partial y} \frac{\partial p}{\partial \dot{x}^3} \right] \\
&\quad - f \rho \alpha^* \dot{u}^1 \frac{\partial x}{\partial \dot{x}^1} \frac{\partial \dot{x}^2}{\partial y} \\
&\quad + f' \sin\xi \frac{\partial \dot{x}^2}{\partial y} \left\{ \rho \alpha^* \dot{u}^1 \frac{\partial z}{\partial \dot{x}^1} + \rho \alpha^* \dot{u}^2 \frac{\partial z}{\partial \dot{x}^2} + \rho \alpha^* \dot{u}^3 \frac{\partial z}{\partial \dot{x}^3} \right\} \qquad (b) \\
\frac{\partial \rho \alpha^* \dot{u}^3}{\partial t} \quad &+ \quad \frac{\partial \rho \alpha^* \dot{u}^j \dot{u}^3}{\partial \dot{x}^i} + \frac{\partial \dot{x}^3}{\partial z} \left[\bar{\rho} \alpha^* (\dot{u}^1)^2 \frac{\partial^2 z}{(\partial \dot{x}^1)^2} \right. \\
&\quad + 2 \rho \alpha^* \dot{u}^1 \dot{u}^2 \frac{\partial^2 z}{\partial \dot{x}^1 \partial \dot{x}^2} - \bar{\rho} \alpha^* (\dot{u}^2)^2 \frac{\partial^2 z}{(\partial \dot{x}^2)^2} \\
&\quad \left. + 2 \rho \alpha^* \dot{u}^3 \left\{ \frac{\partial^2 z}{\partial \dot{x}^1 \partial \dot{x}^3} \dot{u}^1 + \frac{\partial^2 z}{\partial \dot{x}^2 \partial \dot{x}^3} \dot{u}^2 \right\} + \rho \alpha^* (\dot{u}^3)^2 \frac{\partial^2 z}{\left(\partial \dot{x}^3\right)^2} \right] \qquad (A.12) \\
&= \quad -\alpha^* \left[\frac{\partial \dot{x}^3}{\partial x} \frac{\partial \dot{x}^1}{\partial x} \frac{\partial p}{\partial \dot{x}^1} + \frac{\partial \dot{x}^3}{\partial y} \frac{\partial \dot{x}^2}{\partial y} \frac{\partial p}{\partial \dot{x}^2} \right] \\
&\quad + \left[\left(\frac{\partial \dot{x}^3}{\partial x} \right)^2 + \left(\frac{\partial \dot{x}^3}{\partial y} \right)^2 + \left(\frac{\partial \dot{x}^3}{\partial z} \right)^2 \right) \frac{\partial p}{\partial \dot{x}^3} \Bigg] \\
&\quad - \rho \alpha^* g \frac{\partial \dot{x}^3}{\partial z} - f \frac{\partial \dot{x}^3}{\partial z} \left\{ \rho \alpha^* \dot{u}^2 \frac{\partial \dot{x}^1}{\partial x} \frac{\partial y}{\partial \dot{x}^2} \frac{\partial z}{\partial \dot{x}^1} - \rho \alpha^* \dot{u}^1 \frac{\partial \dot{x}^2}{\partial y} \frac{\partial x}{\partial \dot{x}^1} \frac{\partial z}{\partial \dot{x}^2} \right\} \\
&\quad + f' \cos\xi \left\{ \rho \alpha^* \dot{u}^1 \frac{\partial \dot{x}^3}{\partial z} \left(\frac{\partial x}{\partial \dot{x}^1} + \frac{\partial \dot{x}^1}{\partial x} \left(\frac{\partial z}{\partial \dot{x}^1} \right)^2 \right) + \rho \alpha^* \dot{u}^2 \frac{\partial \dot{x}^1}{\partial x} \frac{\partial z}{\partial \dot{x}^1} \frac{\partial z}{\partial \dot{x}^2} \frac{\partial \dot{x}^3}{\partial z} \right\} \\
&\quad + \rho \alpha^* \dot{u}^3 \frac{\partial \dot{x}^1}{\partial x} \frac{\partial z}{\partial \dot{x}^1} \Bigg\} \\
&\quad - f' \sin\xi \left\{ \rho \alpha^* \dot{u}^1 \frac{\partial \dot{x}^2}{\partial y} \frac{\partial z}{\partial \dot{x}^1} \frac{\partial z}{\partial \dot{x}^2} \frac{\partial \dot{x}^3}{\partial z} + \rho \alpha^* \dot{u}^2 \frac{\partial \dot{x}^3}{\partial z} \left(\frac{\partial y}{\partial \dot{x}^2} + \frac{\partial \dot{x}^2}{\partial y} \left(\frac{\partial z}{\partial \dot{x}^2} \right)^2 \right) \right. \\
&\quad \left. + \rho \alpha^* \dot{u}^3 \frac{\partial \dot{x}^2}{\partial y} \frac{\partial z}{\partial \dot{x}^2} \right\} \qquad (c)
\end{aligned}
$$

The Coriolis parameters at latitude φ are defined by $f = 2\Omega \sin\varphi$ and $f' = 2\Omega \cos\varphi$. g denotes the gravitational acceleration. The continuity equation can be written as follows:

$$\frac{\partial \rho \alpha^*}{\partial t} + \frac{\partial \rho \alpha^* \dot{u}^j}{\partial \dot{x}^i} = 0 \tag{A.13}$$

The balance equation of any scalar quantity (e.g. potential temperature θ in the coordinate system $\dot{x}$ is given by:

$$\frac{\partial \rho \alpha^* \chi}{\partial t} + \frac{\partial \rho \alpha^* \chi \dot{u}^j}{\partial \dot{x}^i} = \rho \alpha \overset{*}{Q}_\chi \tag{A.14}$$

The balance equations of momentum have been derived in a form of prognostic equations for the contravariant components $\dot{u}^i$ of the velocity vector in the coordinate system $\dot{x}$. However, one is obviously interested in prognostic equations for the Cartesian velocity vector $v = \{u, v, w,\}$. A relation between the Cartesian components u, v, w and the contravariant components $\dot{u}^i$ in the nonorthogonal coordinate system $\dot{x}$ can be derived from (10):

$$\begin{aligned} \dot{u}^1 &= u \frac{\partial \dot{x}^1}{\partial x} && (a) \\ \dot{u}^2 &= v \frac{\partial \dot{x}^2}{\partial y} && (b) \\ \dot{u}^3 &= u \frac{\partial \dot{x}^3}{\partial x} + v \frac{\partial \dot{x}^3}{\partial y} + w \frac{\partial \dot{x}^3}{\partial z} && (c) \end{aligned} \tag{A.15}$$

The contravariant components in (A.12) to (A.14) are replaced by (A.15) and result in equations (2.7) to (2.9).

A.3 Coriolis force in a rotated coordinate system

In a coordinate system with its x-axis orientated to East and its y-axis orientated to North, the earth's angular velocity is given as follows:

$$\Omega = \begin{pmatrix} 0 \\ 2\Omega \cos\varphi \\ 2\Omega \sin\varphi \end{pmatrix} = \begin{matrix} 0 \\ f' \\ f \end{matrix} \tag{A.16}$$

A rotation of the coordinate system with an angle ξ must maintain the determinant of the matrix. The rotation matrix is given by:

$$D(\dot{e}_i) = \begin{pmatrix} \cos\xi & \sin\xi & 0 \\ -\sin\xi & \cos\xi & 0 \\ 0 & 0 & 1 \end{pmatrix} \tag{A.17}$$

The components of the earth's angular velocity are derived as follows:

$$\dot{\Omega} = \mathrm{D}(\dot{\mathrm{e}}_\mathrm{i}) \cdot \Omega = \begin{pmatrix} \mathrm{f}' sin\xi \\ \mathrm{f}' cos\,\xi \\ \mathrm{f} \end{pmatrix} \tag{A.18}$$

With this equation the Coriolis force in the rotated coordinate system is given:

$$2\dot{\Omega} \times \dot{v} = 2 \begin{vmatrix} \dot{e}_i & \dot{e}_j & \dot{e}_k \\ f'\sin\xi & f'\cos\xi & f \\ u & v & w \end{vmatrix} = 2 \begin{pmatrix} -fv & + & f'w\cos\xi \\ fu & - & f'w\sin\xi \\ f'v\sin\xi & - & f'u\cos\xi \end{pmatrix} \tag{A.19}$$

A.4 Calculation of the local grid rotation angle from an array of latitudes and longitudes

The principal idea in the following formulae is to calculate the angle between a grid points neighbor in y-direction and the north pole using spherical geometry. The first necessary step is to calculate the distance of the two grid points d_j, which should approximately be Δy_j:

$$\cos \mathrm{d_j} = \sin\varphi_{\mathrm{j+1}} \sin\varphi_\mathrm{j} + \cos\varphi_{\mathrm{j+1}} \cos\varphi_\mathrm{j} \cos(\lambda_{\mathrm{j+1}} - \lambda_\mathrm{j}) \tag{A.20}$$

This distance can now be used to calculate the cosine and the sine of ξ, which can be used to retrieve ξ by using the atan2 function. As d_j is a very small angle (in the same order of magnitude as the grid spacing compared to the circumference of the earth) the required $\sin(\arccos(\mathrm{d_j}))$ won't give accurate results.

$$\begin{aligned} \cos\xi &= \frac{\cos\varphi_{j+1}\sin(\lambda_{j+1} - \lambda_j)}{\sin d_j} \\ \sin\xi &= \frac{\sin\varphi_{j+1} - \sin\varphi_j \cos d_j}{\cos\varphi_j \sin d_j} \\ \xi &= \mathrm{atan2}(\cos\xi, \sin\xi) \end{aligned} \tag{A.21}$$

A.5 Calculation of zenith angle and incoming solar radiation

The incoming solar radiation is calculated with respect to

- geographical position of the model area
- date and time of the model run
- inclined surfaces shading of areas due to neighbouring hills etc
- rotation of the used coordinate system with respect to north.

The following derivation is given by Iqbal (1983). For the meaning of symbols within this section see the symbol table at the end of this appendix.

For a given geographical latitude φ, in the absence of the earth's refractive atmosphere, the trigonometric relation between the sun and a horizontal surface is (Pielke, 1984, p211)

$$\cos Z(t) = \sin\delta \sin\varphi + \cos\delta \cos\varphi \cos w = \sin\alpha \tag{A.22}$$

where the declination δ is given by

$$\begin{aligned}\delta = {} & 0.006918 - 0.399912\, cos(d_o) + 0.070257\, sin(d_o) \\ & - 0.006758\, cos(2d_o) + 0.000907\, sin(2d_o) \\ & - 0.002697\, cos(3d_o) + 0.001480\, sin(3d_o)\end{aligned} \tag{A.23}$$

This equation gives the declination in radians (Pielke, 1984, p. 225). d_0 is the julian day. The hour angle w is defined by

$$w = 180^o - s \cdot \frac{15^o}{3600} \tag{A.24}$$

with s seconds since midnight. $cos\,Z(t)$ has to be restricted to values between 0 and 1.

For inclined surfaces it is necessary to prescribe the slope of the surface with respect to the horizontal position and its orientation in relation to the local meridian. The inclination of a surface from the horizontal position can be caluclated by

$$\beta = \arctan\left(\sqrt{\left(\frac{\Delta z_x}{\Delta x}\right)^2 + \left(\frac{\Delta z_y}{\Delta y}\right)^2}\right) \tag{A.25}$$

where Δz_x is the difference in surface height with respect to the x-direction, Δz_y analogous. From the known values for surface's inclination β, orientation of the slope γ and solar azimuth ψ the angle θ between the normal to the surface and sun-earth vector is given by

$$\cos\theta = \cos\beta \cos Z(t) + \sin\beta \sin z(t) \cos(\psi - \gamma) \tag{A.26}$$

The solar azimuth ψ can be taken from

$$cos\,\psi = \frac{sin(90^o - Z(t))sin\phi - sin\delta}{cos(90^o - Z(t))cos\,\phi} \tag{A.27}$$

and then

$$\psi = arccos(cos\,\psi) \cdot \text{sign}\,(w) \tag{A.28}$$

to ensure the right sign of ψ due to its definition (symbol table). For the determination of γ with respect to south direction a possibly given rotation angle ξ of the used coordinate

system has to be taken into account. γ is calculated by means of the FORTRAN standard function ATAN2:

$$\gamma = -\text{ATAN2}\left(cos\xi \cdot \frac{\Delta z}{\Delta x} - sin\xi \cdot \frac{\Delta z}{\Delta y}, sin\xi \cdot \frac{\Delta z}{\Delta x} + cos\xi \cdot \frac{\Delta z}{\Delta y} \right) \quad \text{(A.29)}$$

Each grid point of the model area can be shadowed by the topography at other grid points, if the solar altitude is lower than the topographic altitude in the direction of the solar azimuth. For taking this shadowing effects into account without wasting computing time there are twelve azimuth sectors defined at each grid point. Sector 1 is defined by $+180^o \geq \psi_m > +165^o$, sector 2 by $+165^o \geq \psi_m > +135^o$ and so on by steps of 30^o where $\pm 180^o$ corresponds to north direction. The sector with $-165^o \geq \psi_m \geq 180^o$ belongs to sector 1 again. With respect to a possibly rotated coordinate system, ψ_m is also calculated by means of the FORTRAN function ATAN2:

$$\psi_m = \text{ATAN2}\ (cos\xi\ \Delta x - sin\xi\ \Delta y, -sin\xi\ \Delta x - cos\xi\ \Delta y) \quad \text{(A.30)}$$

When starting the model run a minimum solar altitude α_m is calculated at each grid point and for each sector by

$$\alpha_m = \max\left(\arctan\left(\frac{\Delta z}{\Delta s} \right), \phi \right) \quad \text{(A.31)}$$

which defines a minimum solar altitude for the corresponding azimuth sector. Δz means the difference in topographic height between this grid point and any other grid point within the selected azimuth sector, Δs is the horizontal distance between both grid points. So if the solar azimuth ψ belongs to an azimuth sector ψ_m a grid point is shadowed as long as the solar altitude α is lower than the corresponding minimum solar altitude $\alpha_m = f(\psi_m, x, y)$. For clarity see Figure A.1.

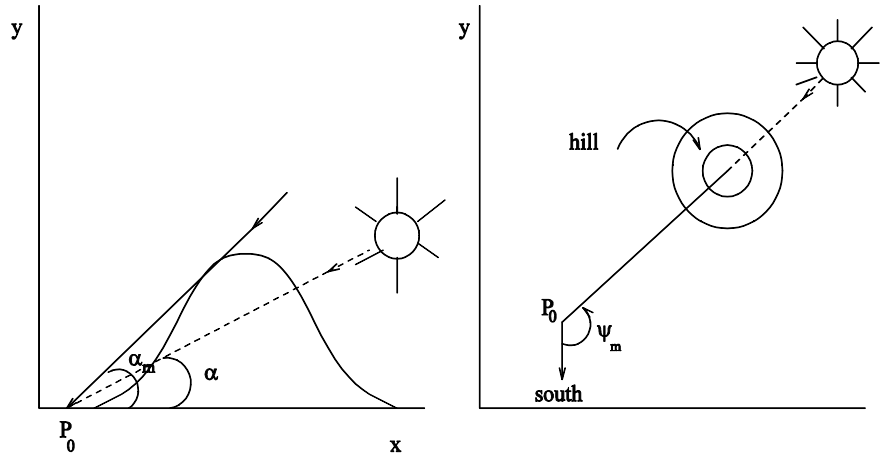

Figure 10.2: Definition of azimuth ψ_m and minimum solar altitude α_m at grid point P_0.

Symbol table

symbol	name	values	meaning/comments
α	solar altitude	$0^o \le \alpha \le 90^o$	angular elevation of the sun above the true horizon (degrees)
β	surface inclination	$0^o \le \beta \le 90^o$	inclination of a surface from the horizontal position (degrees)
γ	surface azimuth	$-180^o \le \gamma \le +180^o$	surface azimuth angle, that is, the deviation of the normal to the surface with respect to the local meridian, south zero, east positive (degrees)
δ	declination	$-23.5^o \le \delta \le +23.5^o$	angular position of the sun at solar noon with respect to the plane of the equator, north positive (degrees)
θ	suns angle to inclinated surface	$0^o \le \theta \le 90^o$	angle of incidence for an arbitrary oriented surface, the angle between normal to the surface and sund-earth vector (degrees)
$Z(t)$	zenith angle	$0^o \le Z(t) \le 90^o$	angular position of sun with respect to the local vertical, $\theta_z = 90^o - \alpha$ (degrees)
ϕ	latitude	$-90^o \le \phi \le +90^o$	geographic latitude, north positive (degrees)
ψ	azimuth	$-180^o \le \psi \le +180^o$	solar azimuth, south zero, east positive (degrees)
w	hour angle	$-180^o \le w \le +180^o$	solar noon zero and morning positive (degrees); changes 15^o every hour (e.g. $w = +15^o$ at 11:00 and $w = -37.5^o$ at 14:30)
ξ	rotation angle	$0^o \le \xi \le 360^o$	rotation of model's coordinate system against north (e.g. $\xi = 0^o$ with x-axis to east, and $\xi = 135^o$ with x-axis to north-west)

B. Model in difference form

B.1 Difference form of the equations

In the following difference forms of the model equations a convention suggested by Shuman (1960) is used:

$$\begin{aligned}
\overline{\psi}^{\dot{x}^i} &= \frac{1}{2} \cdot \left\{ \psi(\dot{x}^i + \frac{\Delta\dot{x}^i}{2}) + \psi(\dot{x}^i - \frac{\Delta\dot{x}^i}{2}) \right\} && (a) \\
\psi^{\dot{x}^i,\dot{x}^j} &= \frac{1}{4} \cdot \left\{ \psi(\dot{x}^i + \frac{\Delta\dot{x}^i}{2}\ \dot{x}^j + \frac{\Delta\dot{x}^j}{2}) + \psi(\dot{x}^i + \frac{\Delta\dot{x}^i}{2}, \dot{x}^j - \frac{\Delta\dot{x}^j}{2}) \right. \\
&\quad \left. + \psi(\dot{x}^i - \frac{\Delta\dot{x}^i}{2}, \dot{x}^j + \frac{\Delta\dot{x}^j}{2}) + \psi(\dot{x}^i - \frac{\Delta\dot{x}^i}{2}, \dot{x}^j - \frac{\Delta\dot{x}^j}{2}) \right\} && (b)
\end{aligned} \tag{B.1}$$

$$\begin{aligned}
\psi^{\dot{x}^i,\dot{x}^j,\dot{x}^k} := \frac{1}{8} \cdot \Big\{ & \psi(\dot{x}^i + \frac{\Delta\dot{x}^i}{2}, \dot{x}^j + \frac{\Delta\dot{x}^j}{2}, \dot{x}^k + \frac{\Delta\dot{x}^k}{2}) \\
& + \psi(\dot{x}^i + \frac{\Delta\dot{x}^i}{2}, \dot{x}^j + \frac{\Delta\dot{x}^j}{2}, \dot{x}^k - \frac{\Delta\dot{x}^k}{2}) \\
& + \psi(\dot{x}^i + \frac{\Delta\dot{x}^i}{2}, \dot{x}^j - \frac{\Delta\dot{x}^j}{2}, \dot{x}^k + \frac{\Delta\dot{x}^k}{2}) \\
& + \psi(\dot{x}^i + \frac{\Delta\dot{x}^i}{2}, \dot{x}^j - \frac{\Delta\dot{x}^j}{2}, \dot{x}^k - \frac{\Delta\dot{x}^k}{2}) \\
& + \psi(\dot{x}^i - \frac{\Delta\dot{x}^i}{2}, \dot{x}^j + \frac{\Delta\dot{x}^j}{2}, \dot{x}^k + \frac{\Delta\dot{x}^k}{2}) \\
& + \psi(\dot{x}^i - \frac{\Delta\dot{x}^i}{2}, \dot{x}^j + \frac{\Delta\dot{x}^j}{2}, \dot{x}^k - \frac{\Delta\dot{x}^k}{2}) \\
& + \psi(\dot{x}^i - \frac{\Delta\dot{x}^i}{2}, \dot{x}^j - \frac{\Delta\dot{x}^j}{2}, \dot{x}^k + \frac{\Delta\dot{x}^k}{2}) \\
& + \psi(\dot{x}^i - \frac{\Delta\dot{x}^i}{2}, \dot{x}^j - \frac{\Delta\dot{x}^j}{2}, \dot{x}^k - \frac{\Delta\dot{x}^k}{2}) \Big\} \quad (c)
\end{aligned} \tag{B.2}$$

For weighted mean values the following abbreviations are used:

$$\overline{\psi}^{\bullet\dot{x}^i} := \psi\ (\dot{x}^i + \frac{\Delta\dot{x}^i}{2}) \cdot F_1 + \psi(\dot{x}^i - \frac{\Delta\dot{x}^i}{2}) \cdot F_2 \tag{B.3}$$

where:

$$
\begin{aligned}
F_1 &= \left\{1+\frac{\Delta\dot{x}_i\left(\dot{x}^i+\frac{\Delta\dot{x}^i}{2}\right)}{\Delta\dot{x}_i\left(\dot{x}^i-\frac{\Delta\dot{x}^i}{2}\right)}\right\}^{-1} \qquad \text{(a)} \\
F_2 &= \left\{1+\frac{\Delta\dot{x}_i\left(\dot{x}^i-\frac{\Delta\dot{x}^i}{2}\right)}{\Delta\dot{x}_i\left(\dot{x}^i+\frac{\Delta\dot{x}^i}{2}\right)}\right\}^{-1} \qquad \text{(b)}
\end{aligned}
\tag{B.4}
$$

The mean values $\overline{\psi}^{\bullet\dot{x}^i,\dot{x}^j}$ and $\overline{\psi}^{\bullet\dot{x}^i,\dot{x}^j,\dot{x}^k}$ are defined analogous to equations (B.1b) and (B.1c).

Gradients $\partial/\partial\dot{x}^i$ of any quantity ψ at a grid point i are discretized centered-in-space and abbreviated by:

$$
\delta_{\dot{x}^i}\psi := \frac{\psi(\dot{x}^i+\frac{\Delta\dot{x}^i}{2})-\psi(\dot{x}^i-\frac{\Delta\dot{x}^i}{2})}{\Delta\dot{x}^i} \tag{B.5}
$$

Mean values of products are usually discretized by seperatly averaging the factors of the product. In general a quantity is not filtered twice in one direction and it is assumed that it changes linear between two grid points. This assumption is also used for all other discretizations.

The transformation coefficients $\partial\dot{x}^i/\partial x^j$, $\partial x^i/\partial\dot{x}^j$ can be directly derived from the coordinates $\dot{x}^i,\dot{x}^j$. For efficiency they are combined from several coefficients, which can be derived following Appendix A.2:

$$
\begin{aligned}
\frac{\partial x}{\partial\dot{x}^1} &= A && (a)\\
\frac{\partial y}{\partial\dot{x}^2} &= B && (b)\\
\frac{\partial z}{\partial\dot{x}^3} &= CG && (c)\\
\frac{\partial z}{\partial\dot{x}^1} &= ADF := AD\overline{F}^{\dot{x}^3} && (d)\\
\frac{\partial z}{\partial\dot{x}^2} &= BEF := BE\overline{F}^{\dot{x}^3} && (e)\\
\frac{\partial\dot{x}^3}{\partial x} &= -\frac{FD}{CG} && (f)\\
\frac{\partial\dot{x}^3}{\partial y} &= -\frac{FE}{CG} && (g)
\end{aligned}
\tag{B.6}
$$

The coefficients (B.6) are often used with operator (B.*1*) leading to $\overline{A}^{\dot{x}^1} = \Delta x$, $\overline{B}^{\dot{x}^2} = \Delta y$ and $\overline{C}^{\dot{x}^3} = \Delta z$.

B.1.1 Difference form of the equations of motion

The advection and diffusion terms in the Reynold equations are integrated in time by means of the Adams-Bashforth-scheme. The Adams-Bashforth-scheme can be expressed by the general formulation (Roache, 1982):

$$\psi^{n+1} = \psi^n - \left\{\frac{3}{2} f^n - \frac{1}{2} f^{n-1}\right\} \cdot \Delta t \tag{B.7}$$

where f denotes the sum of advection terms ADVXI and diffusions terms DIFXI defined in (B.11) and (B.12), which are both discretized centered-in-space. The numerical scheme is stable, if the time step follows the restriction:

$$\Delta t \le 0.9 \cdot \left\{ \frac{|\bar{u}|}{\Delta x} + \frac{|\bar{v}|}{\Delta y} + \frac{1}{\Delta \eta}\left\{|w| + |D||\bar{u}| + |E||\bar{v}|\right\} + \frac{2K_{hor}}{\Delta x^2} + \frac{2K_{hor}}{\Delta y^2} + \frac{2K_{vert}}{\Delta z^2} + \nu_R \right\}^{-1} \tag{B.8}$$

$\Delta x, \Delta y, \Delta z$ characterize the grid increments in $x-, y-$ und $z-$direction. D and E denote the slopes in x- and y- direction at the grid point under consideration. Buoyancy effects are taken into account by the additional restriction:

$$\Delta t < \sqrt{\frac{|\bar{\theta}|}{g}\left(\left|\frac{\partial \bar{\theta}}{\partial z}\right|\right)^{-1}} \tag{B.9}$$

For $|\bar{u}| = |\bar{v}| = 10 m/s$, $|\bar{w}| = 1\ \mathrm{m\,s^{-1}}$, $\Delta x = \Delta y = 1000\ \mathrm{m}$ $\Delta z = 50\ \mathrm{m}$, $K_{vert} = 10\ \mathrm{m^2 s^{-1}}$, $K_{hor} = 50\ \mathrm{m^2 s^{-1}}$, and a flat terrain, $D = E = 0$, the restrictions (B.6) and (B.7) yield $\Delta t \le 18\ \mathrm{s}$. The lowest limit for the time step is 1s. In general the upper limit for the time step in METRAS is set to 60 s and for simulations of cloud and rain formation to 10 s.

The balance equations of momentum (2.23) discretized by the numerical schemes described in Section 4.3 can be written as follows:

$$
\begin{aligned}
\bar{u}^{n+1} &= \bar{u}^{n} - \Delta t\left\{\frac{3}{2}f_1^{n} - \frac{1}{2}f_1^{n-1}\right\} + \Delta t\mathrm{P1FX1}^{n} \\
&+ \Delta t\mathrm{P2FX1}^{n+1} + \Delta t\mathrm{CORX1}^{n} + \Delta t\mathrm{BOUX1}^{n} \qquad (a) \\
\bar{v}^{n+1} &= \bar{v}^{n} - \Delta t\left\{\frac{3}{2}f_2^{n} - \frac{1}{2}f_2^{n-1}\right\} + \Delta t\mathrm{P1FX2}^{n} \\
&+ \Delta t\mathrm{P2FX2}^{n+1} + \Delta t\mathrm{CORX2}^{n} + \Delta t\mathrm{BOUX2}^{n} \qquad (b) \\
\hat{w} &= \bar{w}^{n} - \Delta t\left\{\frac{3}{2}f_3^{n} - \frac{1}{2}f_3^{n-1}\right\} + \Delta t\mathrm{CORX3}^{n} \qquad (c) \\
\hat{u}^{3} &= \{\hat{w} - F(\bar{D}^{\dot{x}^1}\hat{u}^{\dot{x}^3,\dot{x}^1} + \bar{E}^{\dot{x}^2}\hat{v}^{\dot{x}^3,\dot{x}^2})\}/(CG) \qquad (d) \\
\hat{u}^{3\,n+1} &= \hat{u}^{3} + \Delta t\mathrm{P2FX3}^{n+1} \qquad (e) \\
\bar{w}^{n+1} &= \hat{u}^{3\,n+1}\cdot CG + F(\bar{D}^{\dot{x}^1}\overline{u^{n+1}}^{\dot{x}^3,\dot{x}^1} + \bar{E}^{\dot{x}^2}\overline{v^{n+1}}^{\dot{x}^3,\dot{x}^2}) \qquad (f)
\end{aligned}
\tag{B.10}
$$

The sum of the advection term ADVXI and the diffusion term DIFXI is abbreviated by f_i. P1FXI and P2FXI denote pressure gradient forces due to the mesoscale pressures p_1 and p_2. CORXI and BOUXI are the Coriolis and buoyancy terms. These terms are listed in detail in the equations (B.11) to (B.17). The advection terms ADVXI are discretized by:

$$
\begin{aligned}
ADVX1 &= \{\delta_{\dot{x}^1}(\bar{\bar{u}}^{\dot{x}^1}\overline{\overline{\rho_0}^{\dot{x}^1}\bar{G}^{\bullet\dot{x}^1}\bar{u}}^{\dot{x}^1})\}/(A\overline{\rho_0}^{\dot{x}^1}\bar{G}^{\bullet\dot{x}^1}) \\
&+ \{\delta_{\dot{x}^2}(\bar{v}^{\dot{x}^1}\overline{\overline{\rho_0}^{\dot{x}^1}\bar{G}^{\bullet\dot{x}^1}\bar{u}}^{\dot{x}^2})\}/(\bar{B}^{\dot{x}^2}\overline{\rho_0}^{\dot{x}^1}\bar{G}^{\bullet\dot{x}^1}) \\
&+ \{\delta_{\dot{x}^3}(\bar{\bar{\dot{u}}}^{3\,\dot{x}^1}\bar{G}^{\bullet\dot{x}^1}C\overline{\overline{\rho_0}^{\dot{x}^1}\bar{G}^{\bullet\dot{x}^1}\bar{u}}^{\dot{x}^3})\}/(\bar{C}^{\dot{x}^3}\ \bar{G}^{\bullet\dot{x}^1}\ \overline{\rho_0}^{\dot{x}^1}\bar{G}^{\bullet\dot{x}^1}) \qquad (a) \\
ADVX2 &= \{\delta_{\dot{x}^1}(\bar{u}^{\dot{x}^2}\overline{\overline{\rho_0}^{\dot{x}^2}\bar{G}^{\bullet\dot{x}^2}\bar{v}}^{\dot{x}^1})\}/(\bar{A}^{\dot{x}^1}\overline{\rho_0}^{\dot{x}^2}\bar{G}^{\bullet\dot{x}^2}) \\
&+ \{\delta_{\dot{x}^2}(\bar{\bar{v}}^{\dot{x}^1}\overline{\overline{\rho_0}^{\dot{x}^2}\bar{G}^{\bullet\dot{x}^2}v}^{\dot{x}^2})\}/(B\overline{\rho_0}^{\dot{x}^2}\bar{G}^{\bullet\dot{x}^2}) \\
&+ \{\delta_{\dot{x}^3}(\bar{\bar{\dot{u}}}^{3\,\dot{x}^2}\bar{G}^{\bullet\dot{x}^2}C\overline{\overline{\rho_0}^{\dot{x}^2}\bar{G}^{\bullet\dot{x}^2}v}^{\bullet\dot{x}^3})\}/(\bar{C}^{\dot{x}^3}\ \bar{G}^{\bullet\dot{x}^2}\ \overline{\rho_0}^{\dot{x}^2}\bar{G}^{\bullet\dot{x}^2}) \qquad (b) \\
ADVX3 &= \{\delta_{\dot{x}^1}(\bar{\bar{u}}^{\dot{x}^3}\overline{\overline{\rho_0}^{\dot{x}^3}\bar{G}\ \bar{w}}^{\dot{x}^1})\}/(\bar{A}^{\dot{x}^1}\overline{\rho_0}^{\dot{x}^3}G) \\
&+ \{\delta_{\dot{x}2}(\bar{\bar{v}}^{\dot{x}^3}\overline{\rho_0}^{\dot{x}^3}G\bar{w}^{\dot{x}^2})\}/(\bar{B}^{\bullet\dot{x}^2}\overline{\rho_0}^{\dot{x}^3}G) \\
&+ \{\delta_{\dot{x}^3}(\bar{\bar{\dot{u}}}^{3\,\dot{x}^3}G\bar{C}^{\dot{x}^3}\overline{\rho_0}^{\dot{x}^3}Gw^{\dot{x}^3})\}/(CG\overline{\rho_0}^{\dot{x}^3}G) \qquad (c)
\end{aligned}
\tag{B.11}
$$

The diffusion terms DIFXI are discretized by:

$$
\begin{aligned}
DIFX1 &= \{\delta_{\dot{x}^1}(-G\tau_{11}[s,s,s])/(A\overline{\overline{\rho_0}}^{\dot{x}^1}\overline{G}^{\bullet\dot{x}^1})\} \\
&+ \{\delta_{\dot{x}^2}(-\overline{G}^{\bullet\dot{x}^1,\dot{x}^2}\tau_{12}[s,v,v])\}/(\overline{B}^{\dot{x}^2}\overline{\overline{\rho_0}}^{\dot{x}^1}\overline{G}^{\bullet\dot{x}^1}) \\
&+ \{\delta_{\dot{x}^3}(F(D\tau_{11}[v,s,v]+\overline{E}^{\bullet\dot{x}^1\dot{x}^2}\tau_{12}[v,s,v])-\tau_{13}[v,s,v])\}/(C^{\dot{x}^3}\overline{\overline{\rho_0}}^{\dot{x}^1}G^{\bullet\dot{x}^1}) \qquad (a) \\
DIFX2 &= \{\delta_{\dot{x}^1}(-\overline{G}^{\bullet\dot{x}^1,\dot{x}^2}\tau_{12}[s,v,v])\}/(\overline{A}^{\bullet\dot{x}^1}\overline{\overline{\rho_0}}^{\dot{x}^2}\overline{G}^{\bullet\dot{x}^2}) \\
&+ \{\delta_{\dot{x}^2}(-G\tau_{22}[s,s,s])\}/(B\overline{\overline{\rho_0}}^{\dot{x}^2}\overline{G}^{\dot{x}^2}) \\
&+ \{\delta_{\dot{x}^3}(F(\overline{D}^{\bullet\dot{x}^1,\dot{x}^2}\tau_{12}[v,v,s]+E\tau_{22}[v,v,s])-\tau_{23}[v,v,s])\}/(\overline{C}^{\dot{x}^3}\overline{\overline{\rho_0}}^{\dot{x}^2}\overline{G}^{\bullet\dot{x}^2}) \qquad (b) \\
DIFX3 &= \{\delta_{\dot{x}^1}(-\overline{G}^{\bullet\dot{x}^1}\tau_{13}[v,s,v])\}/(\overline{A}^{\dot{x}^1}\overline{\overline{\rho_0}}^{\dot{x}^3}G) \\
&+ \{\delta_{\dot{x}^2}(-\overline{G}^{\bullet\dot{x}^2}\tau_{23}[v,v,s])\}/(\overline{B}^{\dot{x}^2}\overline{\overline{\rho_0}}^{\dot{x}^3}G) \\
&+ \{\delta_{\dot{x}^3}(\overline{F}^{\dot{x}^3}(\overline{D}^{\dot{x}^1}\tau_{13}[s,s,s]+\overline{E}^{\dot{x}^2}\tau_{23}[s,s,s])-\tau_{33}[s,s,s])\}/(C\overline{\rho_0}^{\dot{x}^3}G) \qquad (c)
\end{aligned}
\tag{B.12}
$$

The contravariant vertical velocity component $\dot{u}^3$ is calculated as follows:

$$
\overline{\dot{u}}^3 = \{\overline{w} - F(\overline{D}^{\dot{x}^1}\overline{u}^{\dot{x}^3,\dot{x}^1} + \overline{E}^{\dot{x}^2}\overline{v}^{\dot{x}^3,\dot{x}^2})\}/(C\cdot G) \tag{B.13}
$$

The momentum fluxes $\tau_{ij}[a,b,c]$ are defined by equation (3.2) and calculated by a grid point $[a,b,c]$ (Figures 5.1 and 5.2a,b), where "s" denotes a scalar and "v" a vectorial grid point:

$\tau_{ij}[s,s,s]$: shear stress at a scalar grid point (k, j, i)

$\tau_{ij}[s,s,v]$: shear stress at an u-grid point $(k, j, i+1/2)$

$\tau_{ij}[s,v,s]$: shear stress at a v-grid point $(k, j+1/2, i)$

$\tau_{ij}[v,s,s]$: shear stress at a w-grid point $(k+1/2, j, i)$

$\tau_{ij}[s,v,v]$: shear stress at a grid point of u, v $(k, j+1/2, i+1/2)$

$\tau_{ij}[v,s,v]$: shear stress at a grid point of u, w $(k+1/2, j, i+1/2)$

$\tau_{ij}[v,v,s]$: shear stress at a grid point of v, w $(k+1/2, j+1/2, i)$

The pressure gradient force terms P1FXI due to the mesoscale pressure p_1 are discretized by:

$$
\begin{aligned}
P1FX1 &= -\frac{1}{\overline{\rho_0}^{\dot{x}^1} A}\,\delta_{\dot{x}^1} p_1 \qquad (a)\\
P1FX2 &= -\frac{1}{\overline{\rho_0}^{\dot{x}^2} B}\,\delta_{\dot{x}^2} p_1 \qquad (b)
\end{aligned}
\tag{B.14}
$$

The pressure gradient force terms P2FXI due to the mesoscale pressure $\mathfrak{p}_2$ can be written in difference form as follows:

$$
\begin{aligned}
P2FX1 &= -\frac{1}{\overline{\rho_0}^{\dot{x}^1}}\left\{\frac{1}{A}\delta_{\dot{x}^1} p_2 - \frac{\overline{F}^{\dot{x}^3} D}{\overline{C}^{\dot{x}^3}\overline{G}^{\bullet\dot{x}^1}}\delta_{\dot{x}^3}\overline{p}_2{}^{\dot{x}^1,\dot{x}^3}\right\}\\
P2FX2 &= -\frac{1}{\overline{\rho_0}^{\dot{x}^2}}\left\{\frac{1}{B}\delta_{\dot{x}^2} p_2 - \frac{\overline{F}^{\dot{x}^3} E}{\overline{C}^{\dot{x}^3}\overline{G}^{\bullet\dot{x}^2}}\delta_{\dot{x}^3}\overline{p}_2{}^{\dot{x}^3,\dot{x}^3}\right\}\\
P2FX3 &= -\frac{1}{\overline{\rho_0}^{\dot{x}^3}}\left[\frac{1}{(CG)^2}\left\{1+F^2\left(\overline{D}^{\dot{x}^{1^2}} + \overline{E}^{\dot{x}^{2^2}}\right)\right\}\delta_{\dot{x}^3}\overline{p}_2\right.\\
&\qquad \left. -\frac{F}{CG}\left\{\frac{\overline{D}^{\dot{x}^1}}{\overline{A}^{\dot{x}^1}}\delta_{\dot{x}^1}\overline{p}_2^{\dot{x}^1,\dot{x}^3} + \frac{\overline{E}^{\dot{x}^2}}{\overline{B}^{\dot{x}^2}}\delta_{\dot{x}^2}\overline{p}_2^{\dot{x}^2,\dot{x}^3}\right\}\right]
\end{aligned}
\tag{B.15}
$$

The last equation gives the pressure gradient force term for the vertical velocity $\dot{u}^3$. It is used for the calculation of the pressure $\mathfrak{p}_2$ at time step $\mathfrak{n}$ as well as for the pressure change $\hat{\mathfrak{p}}_2$ (Section 2.5).

The Coriolis terms CORXI are discretized by:

$$
\begin{aligned}
CORX1 &= f\{\overline{v}^{\dot{x}^1,\dot{x}^2} - \overline{V_g}^{\dot{x}^1,\dot{x}^2}\} - fd'\overline{\overline{w}}^{\dot{x}^1,\dot{x}^3} \qquad (a)\\
CORX2 &= -f\{\overline{\overline{u}}^{\dot{x}^1,\dot{x}^2} - \overline{U_g}^{\dot{x}^1,\dot{x}^2}\} + f'd\,\overline{\overline{w}}^{\dot{x}^2,\dot{x}^3} \qquad (b)\\
CORX3 &= -f'\left(d'\,\overline{\overline{u}}^{\dot{x}^1,\dot{x}^3} - d\,\overline{v}^{\dot{x}^2,\dot{x}^3}\right) \qquad (c)
\end{aligned}
\tag{B.16}
$$

The difference form of the bouyancy terms BOUXI is:

$$
\begin{aligned}
BOUX1 &= -g\frac{\overline{\overline{\rho}}^{\dot{x}^1}}{\overline{\rho_0}^{\dot{x}^1}}\overline{F}^{\dot{x}^3} D \qquad (a)\\
BOUX2 &= -g\frac{\overline{\overline{\rho}}^{\dot{x}^2}}{\overline{\rho_0}^{\dot{x}^2}}\overline{F}^{\dot{x}^3} E \qquad (b)
\end{aligned}
\tag{B.17}
$$

B.1.2 Difference form of the budget equations for scalar quantities

The balance equations of scalar quantities are discretized in time by:

$$\chi^{n+1} = \chi^{n} - \Delta t\ \mathrm{ADVPHI} - \Delta t\ \mathrm{DIFPHI} - \Delta t\ \mathrm{QUEPHI} \tag{B.18}$$

Here ADVPHI denotes the advection terms, DIFPHI the diffusion terms and QUEPHI processes due to sources and sinks. The advection terms are formulated by use of the contravariant velocity components $\bar{\dot{u}}^{i}$ as defined by (A.15).

$$\begin{aligned} ADVPHI &= \{\delta_{\dot{x}^1}(\rho_0 \bar{G}^{\bullet \dot{x}^1} \bar{u}\bar{\chi})\}/(\bar{A}^{\dot{x}^1}\rho_0 G) \\ &+ \{\delta_{\dot{x}^2}(\rho_0 \bar{G}^{\bullet \dot{x}^2} \bar{v}\bar{\chi})\}/(\bar{B}^{\dot{x}^1}\rho_0 G) \\ &+ \{\delta_{\dot{x}^3}(\rho_0 \{\bar{w} - F(\bar{D}^{\dot{x}^1}\bar{u}^{\dot{x}^1,\dot{x}^3} + \bar{E}^{\dot{x}^2}\bar{v}^{\dot{x}^2,\dot{x}^3})\}\bar{\chi})\}/(\bar{C}^{\dot{x}^3}\rho_0 G) \end{aligned} \tag{B.19}$$

If the Smolarkiewicz scheme (Smolarkiewicz, 1983,1984; Smolarkiewicz and Clark, 1986) is used, several iterative upstream steps are performed and for the second and each following iteration step "anti-diffusive" velocities $(\hat{u},\hat{v},\hat{w})$ are used instead of the physical velocity components u,v,w. For the one dimensional case in vertical direction the scheme can be written:

1. Advective Step:

$$\psi_k = \psi_k^n - [F(\psi_k^n, \psi_{k+1}^n, \dot{u}_{k+1/2}^3) - F(\psi_{k-1}^n, \psi_k^n, \dot{u}_{k-1/2}^3)] \tag{B.20}$$

2. Antidiffusive step:

$$\psi_k^{n+1} = \psi_k - [F(\psi_k, \psi_{k+1}, \hat{\dot{u}}^3{}_{k-1/2}) - F(\psi_{k-1}, \psi_k, \hat{\dot{u}}^3{}_{k-1/2}] \tag{B.21}$$

F denotes the advective flux of a quantity $\psi = \rho_0\bar{\chi}$, which is defined at the vectorial grid points of the velocity components:

$$F = (\psi_k, \psi_{k+1}, \hat{\dot{u}}^3) = [(\hat{\dot{u}}^3 + |\hat{\dot{u}}^3|)\psi_k + (\hat{\dot{u}}^3 - |\hat{\dot{u}}^3|)\psi_{k+1}]\frac{\Delta t}{2\Delta \dot{x}^3} \tag{B.22}$$

The antidiffusive velocity $\hat{\dot{u}}^3$ is calculated from:

$$\hat{\dot{u}}^3{}_{k+1/2} = [|\hat{\dot{u}}^3{}_{k+1/2}|\,\Delta x_k - \Delta t(\hat{\dot{u}}^3{}_{k+1/2})^2] \cdot \frac{\psi_{k+1} - \psi_k}{(\psi_{k+1} + \psi_k + \varepsilon)\Delta \dot{x}^3} \tag{B.23}$$

$\varepsilon = 10^{-15}$ is added to ensure $\hat{\dot{u}}^3 = 0$ for $\psi_{k+1} = \psi_k = 0$ and to prevent a zero denominator if $\psi_{k+1} = -\psi_k$. The original Smolarkiewicz scheme is derived for positive defined quantities only. To apply the scheme to other quantities it is necessary to add a factor to the data array (Smolarkiewicz and Clark, 1986). In METRAS the lowest value of an array is determined and, if this value is negative, half as much of this value is added to the array to ensure positive values overall.

The diffusion terms F_χ are discrtized by:

$$
\begin{aligned}
DIFPHI = &-\{\delta_{\dot{x}^1}(\overline{\rho_0}^{\dot{x}^1}\overline{G}^{\bullet\dot{x}^1}\overline{\hat{K}_{hor}}^{\dot{x}^1}\delta_{\dot{x}^1}\overline{\chi}[s,v,s]/A)\}/(A^{\dot{x}^1}\rho_0 G)\\
&-\{\delta_{\dot{x}^2}(\overline{\rho_0}^{\dot{x}^2}\overline{G}^{\bullet\dot{x}^2}\overline{\hat{K}_{hor}}^{\dot{x}^2}\delta_{\dot{x}^2}\overline{\chi}[s,v,s]/B)\}/(B^{\dot{x}^2}\rho_0 G)\\
&-\{\delta_{\dot{x}^3}(\overline{\rho_0}^{\dot{x}^3}\overline{\hat{K}_{ver}}^{\dot{x}^3}\delta_{\dot{x}^3}\overline{\chi}[v,s,s]/C)\}/(\overline{C}^{\dot{x}^3}\rho_0 G^2)\\
&+\{\delta_{\dot{x}^1}(\overline{\rho_0}^{\dot{x}^1}\overline{\hat{K}_{hor}}^{\dot{x}^1}D\overline{F}^{\dot{x}^3}\delta_{\dot{x}^3}\overline{\chi}[s,s,v]/C^{\dot{x}1})\}/(\overline{A}^{\dot{x}^1}\rho_0 G)\\
&+\{\delta_{\dot{x}^2}(\overline{\rho_0}^{\dot{x}^2}\overline{\hat{K}_{hor}}^{\dot{x}^2}E\overline{F}^{\dot{x}^3}\delta_{\dot{x}^3}\overline{\chi}[s,v,s]/\overline{C}^{\dot{x}^2})\}/(\overline{B}^{\dot{x}^2}\rho_0 G)\\
&+\{\delta_{\dot{x}^3}(\overline{\rho_0}^{\dot{x}^3}\overline{\hat{K}_{hor}}^{\dot{x}^3}\overline{D}^{\dot{x}^1}F\delta_{\dot{x}^1}\overline{\chi}[v,s,s]/\overline{A}^{\dot{x}^1})\}/(\overline{C}^{\dot{x}^3}\rho_0 G)\\
&+\{\delta_{\dot{x}^3}(\overline{\rho_0}^{\dot{x}^3}\overline{\hat{K}_{hor}}^{\dot{x}^3}\overline{E}^{\dot{x}^2}F\delta_{\dot{x}^2}\overline{\chi}[v,s,s]/\overline{B}^{\dot{x}^2})\}/(\overline{C}^{\dot{x}^3}\rho_0 G)\\
&-\{\delta_{\dot{x}^3}(\overline{\rho_0}^{\dot{x}^3}\overline{\hat{K}_{hor}}^{\dot{x}^3}F^2(\overline{D}^{\dot{x}^{1^2}}+\overline{E}^{\dot{x}^{2^2}})\delta_{\dot{x}^3}\overline{\chi}[v,s,s]/CG)\}/(\overline{C}^{\dot{x}^3}\rho_0 G)
\end{aligned}
\tag{B.24}
$$

Letters in brackets denote the grid points (Figures 5.1 and 5.2a,b) at which the gradients $\delta_{\dot{x}}\overline{\chi}$ are calculated.

B.1.3 Difference form of divergence

Equation (2.25) for the calculation of the pressure change $\hat{p}_2$ can be written in finite difference form in the following way:

$$
\begin{aligned}
\nabla\rho_0\alpha^*\hat{v} = &\overline{B}^{\dot{x}^2}\overline{C}^{\dot{x}^3}\cdot\delta_{\dot{x}^1}\left(\overline{\rho}^{\dot{x}^1}\,\overline{G}^{\bullet\dot{x}^1}\hat{u}\right)\\
&+\overline{A}^{\dot{x}^1}\overline{C}^{\dot{x}^3}\cdot\delta_{\dot{x}^2}\left(\overline{\rho}^{\dot{x}^2}\,\overline{G}^{\bullet\dot{x}^2}\hat{v}\right)\\
&+\overline{A}^{\dot{x}^1}\overline{B}^{\dot{x}^2}G\cdot\delta_{\dot{x}^3}\left(\overline{\rho}^{\dot{x}^3}\,C\cdot\hat{u}^3\right)
\end{aligned}
\tag{B.25}
$$

Here the surface normal velocity component $\hat{u}^3$ is calculated by:

$$
\hat{u}^3 = \frac{1}{CG}\left(\hat{w} - F(\overline{D}^{\dot{x}^1}\hat{u}^{\dot{x}^3,\dot{x}^1} + \overline{E}^{\dot{x}^2}\overline{\hat{v}}^{\dot{x}^3,\dot{x}^2})\right) \tag{B.26}
$$

The poisson-equation in finite-difference form can be derived by use of equations (B.15) and (2.24) in equation (B.25). A matrix of coefficients results for the pressure field $\hat{p}_2$:

$$
\begin{aligned}
\hat{p}_{kji}: \quad B000 \;=\; & -\overline{\overline{G_{ji}}^{\bullet\dot{x}^1}}\,\overline{B_j}^{\dot{x}^2}\,\overline{C_k}^{\dot{x}^3}/A_i - \overline{\overline{G_{ji-1}}^{\bullet\dot{x}^1}}\,\overline{B_j}^{\dot{x}^2}\,\overline{C_k}^{\dot{x}^3}/A_{i-1} \\
& -\overline{\overline{G_{ji}}^{\bullet\dot{x}^2}}\,\overline{A_i}^{\dot{x}^1}\,\overline{C_k}^{\dot{x}^3}/B_j - \overline{\overline{G_{j-1,i}}^{\bullet\dot{x}^2}}\,\overline{A_i}^{\dot{x}^1}\,\overline{C_k}^{\dot{x}^3}/B_{j-1} \\
& -\overline{A_i}^{\dot{x}^1}\,\overline{B_j}^{\dot{x}^2}\,(1+F_k^2(\overline{D_{ji}}^{\dot{x}^1{}^2}+\overline{E_{ji}}^{\dot{x}^2{}^2}))/(C_k G_{ji}) \\
& -\overline{A_i}^{\dot{x}^1}\,\overline{B_j}^{\dot{x}^2}\,(1+F_{k-1}^2(\overline{D_{ji}}^{\dot{x}^1{}^2}+\overline{E_{ji}}^{\dot{x}^2{}^2}))/(C_{k-1} G_{ji}) \qquad (a) \\
\hat{p}_{kji+1}: \quad BP00 \;=\; & \overline{B_j}^{\dot{x}^2}\,\overline{C_k}^{\dot{x}^3}\,\overline{G_{ji}}^{\bullet\dot{x}^1}/A_i \\
& -0.25\,\overline{B_j}^{\dot{x}^2}\,\overline{D_{ji}}^{\dot{x}^1}(F_k - F_{k-1}) \qquad (b) \\
\hat{p}_{kji-1}: \quad BM00 \;=\; & \overline{B_j}^{\dot{x}^2}\,\overline{C_k}^{\dot{x}^3}\,\overline{G_{ji-1}}^{\dot{x}^1}/A_{i-1} \\
& +0.25\,\overline{B_j}^{\dot{x}^2}\,\overline{D_{ji}}^{\dot{x}^1}(F_k - F_{k-1}) \qquad (c) \\
\hat{p}_{kj+1i}: \quad B0P0 \;=\; & \overline{A_i}^{\dot{x}^1}\,\overline{C_k}^{\dot{x}^3}\,\overline{G_{ji}}^{\dot{x}^2}/B_j \\
& -0.25\,\overline{A_i}^{\dot{x}^1}\,\overline{E_{ji}}^{\dot{x}^2}(F_k - F_{k-1}) \qquad (d) \\
\hat{p}_{kj-1i}: \quad B0M0 \;=\; & \overline{A_i}^{\dot{x}^1}\,\overline{C_k}^{\dot{x}^3}\,\overline{G_{j-1i}}^{\dot{x}^2}/B_{j-1} \\
& +0.25\,\overline{A_i}^{\dot{x}^1}\,\overline{E_{ji}}^{\dot{x}^2}(F_k - F_{k-1}) \qquad (e) \\
\hat{p}_{k+1ji}: \quad B00P \;=\; & \overline{A_i}^{\dot{x}^1}\,\overline{B_j}^{\dot{x}^2}\,(1+F_k^{\dot{x}2}(\overline{D_{ji}}^{\dot{x}^1{}^2}+\overline{E_{ji}}^{\dot{x}2^2}))/(C_k G_{ji}) \\
& -0.25\,\overline{B_j}^{\dot{x}^2}\,\overline{F_k}^{\dot{x}^3}(D_{ji} - D_{ji-1}) \\
& -0.25\,\overline{A_i}^{\dot{x}^1}\,\overline{F_k}^{\dot{x}^3}(E_{ji} - E_{j-1i}) \qquad (f) \\
\hat{p}_{k-1ji}: \quad B00M \;=\; & \overline{A_i}^{\dot{x}^1}\,\overline{B_j}^{\dot{x}^2}\,(1+F_{k-1}^2(\overline{D_{ji}}^{\dot{x}^1{}^2}+\overline{E_{ji}}^{\dot{x}^2{}^2}))/(C_{k-1} G_{ji}) \\
& +0.25\,\overline{B_j}^{\dot{x}^2}\,\overline{F_k}^{\dot{x}^3}(D_{ji} - D_{ji-1}) \\
& +0.25\,\overline{A_i}^{\dot{x}^1}\,\overline{F}_k^{\dot{x}^3}(E_{ji} - \overline{E_{j-1i}}) \qquad (g) \\
\hat{p}_{k+1ji+1}: \quad BP0P \;=\; & -0.25\,\overline{B_j}^{\dot{x}^2}\,(\overline{F_k}^{\dot{x}^3}D_{ji} + F_k\overline{D_{ji}}^{\dot{x}^1}) \qquad (h) \\
\hat{p}_{k+1ji-1}: \quad BM0P \;=\; & +0.25\,\overline{B_j}^{\dot{x}^2}\,(\overline{F_k}^{\dot{x}^3}D_{ji-1} + F_k\overline{D_{ji}}^{\dot{x}^1}) \qquad (i) \\
\hat{p}_{k-1ji+1}: \quad BP0M \;=\; & +0.25\,\overline{B_j}^{\dot{x}^2}\,(\overline{F}_k^{\dot{x}^3}D_{ji} + F_{k-1}\overline{D_{ji}}^{\dot{x}^1}) \qquad (j) \\
\hat{p}_{k-1ji-1}: \quad BM0M \;=\; & -0.25\,\overline{B_j}^{\dot{x}^2}\,(\overline{F}_k^{\dot{x}^3}D_{ji-1} + F_{k-1}\overline{D_{ji}}^{\dot{x}^1}) \qquad (k) \\
\hat{p}_{k+1j+1i}: \quad B0PP \;=\; & -0.25\,\overline{A_i}^{\dot{x}^1}\,(\overline{F_k}^{\dot{x}^3}E_{ji} + F_k\overline{E_{ji}}^{\dot{x}^2}) \qquad (l) \\
\hat{p}_{k+1j-1i}: \quad B0MP \;=\; & +0.25\,\overline{A_i}^{\dot{x}^1}\,(\overline{F_k}^{\dot{x}^3}E_{j-1i} + F_k\overline{E_{ji}}^{\dot{x}^2}) \qquad (m) \\
\hat{p}_{k-1j+1i}: \quad B0PM \;=\; & +0.25\,\overline{A_i}^{\dot{x}^1}\,(\overline{F_k}^{\dot{x}^3}E_{ji} + F_{k-1}\overline{E_{ji}}^{\dot{x}^2}) \qquad (n) \\
\hat{p}_{k-1j-1i}: \quad B0MM \;=\; & -0.25\,\overline{A_i}^{\dot{x}^1}\,(\overline{F}_k^{\dot{x}^3}E_{j-1i} + F_{k-1}\overline{E_{ji}}^{\dot{x}^2}) \qquad (o)
\end{aligned}
\qquad (B.27)
$$

The coefficients have to be modified at the model boundaries.

B.1.4 Differential form of hydrostatic assumption

The hydrostatic assumption is solved by use of centered differences:

$$p_{1_{kji}} = p_{1_{k+ji}} + gG_{ji}C_k\overline{\tilde{\rho}}^{\dot{x}^3}_{kji} \tag{B.28}$$

B.1.5 Calculation of density deviations

$$\tilde{\rho}_{kji} = \rho_{o\,kji}\left\{\frac{-\tilde{\theta}_{kji} + \tilde{\theta}_{Mean}}{\theta_{o\,kji}} + \frac{c_v}{c_p}\frac{p_{1\,kji} + p_{2\,kji}}{p_{o\,kji}}\right\} \tag{B.29}$$

B.2 Difference form of boundary conditions

The boundary conditions used in the model are desribed in this Section in difference form.

B.2.1 Lower boundary

B.2.1.1 Wind and Pressure

Wind and pressure boundary conditions are always coupled (Chapter 6) and have thus to be discretized corresponding to each other.

At the lower boundary only the surface normal pressure gradient is effective and correspondingly the surface normal component of the momentum vector. It can allways be calculated from:

$$\overline{\rho_0}^{\dot{x}^3}\overline{\alpha^*}^{\dot{x}^3}\dot{u}^3 = 0 \Rightarrow \overline{\dot{u}^3} = 0 \tag{B.30}$$

Use of equation (2.24) and of preliminary velocities results in:

$$
\begin{aligned}
0 = {} & \overline{\rho_0}^{\dot{x}^3}\,\overline{\alpha^*}^{\dot{x}^3}\,\hat{u}^3 \\
& - \Delta t\,\overline{\alpha^*}^{\dot{x}^3}\left[\frac{\partial \dot{x}^1}{\partial x}\frac{\partial \dot{x}^3}{\partial x}\frac{\partial \hat{p}_2}{\partial \dot{x}^1} + \frac{\partial \dot{x}^2}{\partial y}\frac{\partial \dot{x}^3}{\partial y}\frac{\partial \hat{p}_2}{\partial \dot{x}^2}\right. \\
& \left. + \left(\left(\frac{\partial \dot{x}^3}{\partial x}\right)^2 + \left(\frac{\partial \dot{x}^3}{\partial y}\right)^2 + \left(\frac{\partial \dot{x}^3}{\partial y}\right)^2 \frac{\partial \hat{p}_2}{\partial \dot{x}^3}\right) \right. \\
= {} & \overline{\rho_0}^{\dot{x}^3}\,\overline{\alpha^*}^{\dot{x}^3}\,\overline{\dot{u}^3}
\end{aligned}
\tag{B.31}
$$

NUVWX3(1)=0, Cyclic Boundary Conditions

This boundary condition can only be selected if no pressure perturbation $\mathfrak{p}_2$ is to be calculated. In vertical direction it makes only sense in connection with model tests. The upper boundary condition has also to be cyclic.

$$
\begin{aligned}
\overline{u}(0,j,i) &= \overline{u}(NX3,j,i) \\
\overline{v}(0,j,i) &= \overline{v}(NX3,j,i) \\
\overline{w}(0,j,i) &= \overline{w}(NX3M1,j,i)
\end{aligned}
\tag{B.32}
$$

NUVWX3(1)=3, No Slip Condition

This Boundary condition can be used in connection with boundary condition NP2X3(1) = 1.

For a no slip boundary condition the surface parallel wind velocity is zero at the ground:

$$
\begin{aligned}
\overline{\overline{\dot{u}_1}^{\dot{x}^3}}\Big|_{\eta=0} &= \overline{u}^{\dot{x}^3}\frac{\partial x}{\partial \dot{x}^1}\Big|_{\eta=0} + \overline{w}^{\dot{x}^3}\frac{\partial z^{\dot{x}^3}}{\partial \dot{x}^1}\Big|_{\eta=0} = 0 \\
\overline{\overline{\dot{u}_2}^{\dot{x}^3}}\Big|_{\eta=0} &= \overline{v}^{\dot{x}^3}\frac{\partial y}{\partial \dot{x}^2}\Big|_{\eta=0} + \overline{w}^{\dot{x}^2}\frac{\partial z^{\dot{x}^3}}{\partial \dot{x}^3}\Big|_{\eta=0} = 0
\end{aligned}
\tag{B.33}
$$

From these equations and equation (B.30) a diagnostic equation for $\overline{w}$ can be derived. With the assumption of vanishing vertical velocities at the lateral boundaries of the model the following boundary conditions are derived:

$$
\begin{aligned}
\overline{w}(0,j,i) &= 0 \\
\overline{u}(0,j,i) &= -\overline{u}(1,j,i) \\
\overline{v}(0,j,i) &= -\overline{v}(1,j,i)
\end{aligned}
\tag{B.34}
$$

NUVWX3(1)=27, Free Slip Condition

This Boundary condition can be used in connection with boundary condition NP2X3(1) = 1.

For a free slip boundary condition the vertical gradient of the surface parallel wind velocity is zero at the ground (Clark, 1977):

$$\delta_{\dot{x}^3}\overline{\dot{u}^1}\,|_{\eta=0} = \delta_{\dot{x}^3}\,\overline{u}\,\frac{\partial \dot{x}^1}{\partial x}\bigg|_{\eta=0} = 0$$
$$\delta_{\dot{x}^3}\overline{\dot{u}^2}\,|_{\eta=0} = \delta_{\dot{x}^3}\,\overline{v}\,\frac{\partial \dot{x}^2}{\partial y}\bigg|_{\eta=0} = 0 \qquad \text{(B.35)}$$

From this equations for the components of the horizontal wind vector it can be derived:

$$\overline{u}(0,j,i) = \overline{u}(1,j,i)$$
$$\overline{v}(0,j,i) = \overline{v}(1,j,i) \qquad \text{(B.36)}$$

The vertical wind at the ground is calculated corresponding to equation (B.*10*):

$$\overline{w}(0,j,i) = \overline{D}^{\dot{x}^1}(j,i)\;\overline{u}^{\dot{x}^1}(1,j,i) + \overline{E}^{\dot{x}^2}(j,i)\;\overline{v}^{\dot{x}^2}(1,j,i) \qquad \text{(B.37)}$$

For flat terrain the vertical velocity results to zero.

B.2.1.2 Prognostic Scalar Quantities

The scalar quantities are denoted by $\overline{\chi}$. The values $\overline{\chi}$ are the sum of the large-scale value χ_0 and the mesoscale values $\widetilde{\chi}$. All boundary conditions are formulated for the value $\widetilde{\chi}$ and transformed to formulations for $\widetilde{\chi}$ since these values are calculated prognostically in the model.

NPHI3(1)=0, Cyclic Boundary Conditions

As for the wind, this boundary condition has to be used at the lower and upper boundary both.

$$\overline{w}(0,j,i) = \overline{D}^{\dot{x}^1}(j,i)\;\overline{u}^{\dot{x}^1}(1,j,i) + \overline{E}^{\dot{x}^2}(j,i)\;\overline{v}^{\dot{x}^2}(1,j,i) \qquad \text{(B.38)}$$

This boundary condition is not implemented for liquid water and tracers.

NPHI3(1)=1, Zero Gradient

For tracer transport a zero gradient corresponds to total reflexion. No tracers are absorbed at the ground. This is not realized in METRAS by this boundary condition but by NPIH3(1)=8 together with a deposition velocity $v_d = 0$.

$$\widetilde{\chi}(0,j,i) = \widetilde{\chi}(1,j,i) + \chi_0(1,j,i) - \chi_0(0,j,i) \qquad \text{(B.39)}$$

This boundary condition results in zero fluxes at the ground, e.g. $\chi_* = 0$. It corresponds to boundary condition NPHI3(1)=6 and is implemented for cloud water only.

NPHI3(1)=3, Fixed Values

To keep the values at the surface constant in time, the values at the "old" time step have to be used to calculate the surface values:

$$\tilde{\chi}^n(surface,j,i) = 0.5 \cdot \left(\tilde{\chi}^n(0,j,i) + \chi_0{}^n(0,j,i) + \tilde{\chi}^n(1,j,i) + \chi_0{}^n(1,j,i)\right) \tag{B.40}$$

The values at the boundary are calculated from:

$$\tilde{\chi}^{n+1}(0,j,i) = 2 \cdot \tilde{\chi}^n(surface,j,i) - \tilde{\chi}^{n+1}(1,j,i) - \chi_0{}^{n+1}(1,j,i) - \chi_0{}^{n+1}(0,j,i) \tag{B.41}$$

This boundary condition is not implemented for rain water and tracers.

NPHI3(1)=5, Surface Energy Budget for the Temperature and Budget-Equation for Humidity

The surface values $\bar{\chi}^{n+1}(\text{surface,j,i})$ are derived from prognostic equations. The boundary values are derived in correspondence with equation (VI.12) but by use of the surface values at the new time step $n+1$.

NPHI3(1)=7, Flux at the Boundary equal to Flux in the Model

This boundary condition is not defined at the boundary but between the surface and the next inner grid point. It corresponds to a zero vertical gradient of the fluxes:

$$\overline{\chi' w'}(\text{surface,j,i}) = \overline{\chi' w'}(1,\text{j,i}) \tag{B.42}$$

With respect to Chapter 3 this equation results to:

$$\overline{\chi' w'} = -u_* \chi_* = -K \left.\frac{\partial \bar{\chi}}{\partial z}\right|_{k=1} \tag{B.43}$$

The difference form of the equation is:

$$\tilde{\chi}(0,\text{j,i}) = \tilde{\chi}(2,\text{j,i}) + \chi_0(2,\text{j,i}) - \chi_0(0,\text{j,i}) - \frac{2u_* \chi_* \Delta z(1,\text{j,i})}{\hat{K}(1,\text{j,i})} \tag{B.44}$$

This boundary condition corresponds to a total absorption of cloud water or rain at the ground and is implemented for these two variables only.

NPHI3(1)=8, Flux at the Boundary calculated from Deposition Velocity

This boundary condition can only be used for tracer transport. The derivation is similar to boundary condition 7, but the surface fluxes are calculated from:

$$\overline{C'_i w'}(surface,j,i) = -u_* C_{j*} = -v_D \overline{C}_j(1,j,i) \tag{B.45}$$

For the boundary values a formulation similar to equation (VI.15) results. The fluxes $u_*\chi_*$ are now calculated from $v_D \cdot (\overline{C}_j(1,j,i) + C_{0j}(1,j,i))$.

$$\begin{aligned}\widetilde{C}_j(0,j,i) &= \widetilde{C}_j(2,j,i) + C_{0j}(2,j,i) - C_{0j}(0,j,i) \\ &- \left(\widetilde{C}_j(1,j,i) + C_{0j}(1,j,i)\right) \cdot \frac{2v_D \Delta z(1,j,i)}{\hat{K}(1,j,i)}\end{aligned} \tag{B.46}$$

B.2.2 Upper boundary

B.2.2.1 Wind and Pressure

At the upper boundary the boundary conditions for wind and pressure are coupled in a similar way as at the lower boundary.

NUVWX3(2)=0, Cyclic Boundary Conditions

This boundary condition can only be selected if no pressure perturbation p_2 is to be calculated. In vertical direction it makes only sense in connection with model tests. The lower boundary condition has also to be cyclic (Section B.2.1.).

$$\begin{aligned}\overline{u}(NX3P1,j,i) &= \overline{u}(1,j,i) \\ \overline{v}(NX3P1,j,i) &= \overline{v}(1,j,i) \\ \overline{w}(NX3,j,i) &= \overline{w}(1,j,i)\end{aligned} \tag{B.47}$$

NUVWX3(2)=4, Large-Scale Values Prescribed

This boundary condition can be used in connection with boundary condition NP2X3(2) = 1.

The values of the components of the wind velocity vector are prescribed from the geostrophic values:

$$\begin{aligned}\overline{u}(NX3P1,j,i) &= UG(NX3P1,j,i) + UG(NX3,j,i) - \overline{u}(NX3,j,i) \\ \overline{v}(NX3P1,j,i) &= VG(NX3P1,j,i) + VG(NX3,j,i) - \overline{v}(NX3,j,i) \\ \overline{w}(NX3,j,i) &= W0(NX3,j,i)\end{aligned} \tag{B.48}$$

NUVWX3(2)=23, Boundary Normal Wind Components: Large-Scale Values; Boundary Parallel Wind Components: Zero Gradient

This boundary condition can be used in connection with boundary condition NP2X3(2) = 1.

$$\begin{aligned}\overline{u}(NX3P1,j,i) &= \overline{u}(NX3,j,i) \\ \overline{v}(NX3P1,j,i) &= \overline{v}(NX3,j,i) \\ \overline{w}(NX3,j,i) &= W0(NX3,j,i)\end{aligned} \tag{B.49}$$

NUVWX3(2)=24, Boundary Normal Wind Components: Large-Scale Values; Boundary Parallel Wind Components: Gradient at the Boundary Equal to Gradient in the Model

This boundary condition can be used in connection with boundary condition NP2X3(2) = 1.

$$\begin{aligned}\bar{u}(NX3P1,j,i) &= 2\cdot\bar{u}(NX3,j,i) - \bar{u}(NX3M1,j,i)\\ \bar{v}(NX3P1,j,i) &= 2\cdot\bar{v}(NX3,j,i) - \bar{v}(NX3M1,j,i)\\ \bar{w}(NX3,j,i) &= W0(NX3,j,i)\end{aligned} \tag{B.50}$$

B.2.2.2 Prognostic Scalar Quantities

NPHI3(2)=0, Cyclic Boundary Conditions

As for the wind, this boundary condition has to be used at the lower and upper boundary both.

$$\tilde{\chi}(NX3P1,j,i) = \tilde{\chi}(1,j,i) + \chi_0(1,j,i) - \chi_0(NX3P1,j,i) \tag{B.51}$$

This boundary condition is implemented in METRAS for temperature and humidity only.

NPHI3(2)=1, Zero Gradient

$$\tilde{\chi}(NX3P1,j,i) = \tilde{\chi}(NX3,j,i) + \chi_0(NX3,j,i) - \chi_0(NX3P1,j,i) \tag{B.52}$$

This boundary condition results in zero fluxes at the model top.

NPHI3(2)=2, Gradient at the Boundary Equal to Gradient in the Model

$$\begin{aligned}\tilde{\chi}(NX3P1,j,i) = 2\cdot\big(&\tilde{\chi}(NX3,j,i) + \chi_0(NX3,j,i)\big)\\ &- \tilde{\chi}(NX3M1,j,i) - \chi_0(NX3M1,j,i)\\ &- \chi_0(NX3P1,j,i)\end{aligned} \tag{B.53}$$

This boundary condition is not implemented for liquid waters.

NPHI3(2)=3, Fixed Values

To keep the value at the model top constant in time, the values at the “old” time step have to be used to calculate the values at the model top:

$$\begin{aligned}\bar{\chi}^n(top,j,i) = 0.5\cdot\Big(&\tilde{\chi}^n(NX3P1,j,i) + {\chi_0}^n(NX3P1,j,i)\\ &+ \tilde{\chi}^n(NX3,j,i) + {\chi_0}^n(NX3,j,i)\Big)\end{aligned} \tag{B.54}$$

For the next time step the boundary values are derived from:

$$\tilde{\chi}^{n+1}(NX3P1,j,i) = 2\cdot\bar{\chi}^{n}(top,j,i) - \tilde{\chi}^{n+1}(NX3,j,i) - \chi_0{}^{n+1}(NX3,j,i) - \chi_0{}^{n+1}(NX3P1,j,i) \tag{B.55}$$

B.2.3 Lateral boundaries

All boundary conditions described in this section can be used at all lateral boundaries. They are not given in detail for all boundaries here, only the formulation at the eastern boundary is presented.

B.2.3.1 Wind and Pressure

Wind and pressure boundary conditions are always coupled (Chapter 6) and have thus to be discretized corresponding to each other.

NUVWX1,2(1,2)=0, Cyclic Boundary Conditions

This boundary condition can only be selected if no pressure perturbation p_2 is to be calculated. It has always to be used at both corresponding boundaries, e.g. at the western and eastern boundary:

$$\bar{u}(k,j,0) = \bar{u}(k,j,NX1M1)$$

$$\bar{v}(k,j,0) = \bar{v}(k,j,NX1)$$

$$\bar{w}(k,j,0) = \bar{w}(j,j,NX1)$$

$$\bar{u}(k,j,NX1) = \bar{u}(k,j,1)$$

$$\bar{v}(k,j,NX1P1) = \bar{v}(k,j,1)$$

$$\bar{w}(k,j,NX1P1) = \bar{w}(j,j,1) \tag{B.0}$$

NUVWX1,2(1,2)=9, Radiation Boundary Conditions at the Outermost Grid Point

This boundary condition can be used in connection with boundary condition NP2X1,2(1,2) = 1.

It can be derived as follows:

$$\left.\frac{\partial\psi}{\partial\dot{x}^1}\right|_{k,j,i} = \frac{\psi(k,j,i+0.5)-\psi(k,j,i-0.5)}{\Delta\dot{x}^1(i)}$$
$$\left.\frac{\partial\psi}{\partial\dot{x}^2}\right|_{k,j,i} = \frac{\psi(k,j+0.5,i)-\psi(k,j-0.5,i)}{\Delta\dot{x}^2(j)} \qquad \text{(B.56)}$$
$$\left.\frac{\partial\psi}{\partial\dot{x}^3}\right|_{k,j,i} = \frac{\psi(k+0.5,j,i)-\psi(k-0.5,j,i)}{\Delta\dot{x}^3(k,j,i-0.5)}$$

The phase velocity c_i can be calculated by use of the assumption $c_i^n = c_{i-1}^{n-1}$ as follows:

$$\begin{aligned} c_1^n(k,j,i) &= c_1^{n-1}(k,j,i-1) \\ &= -\frac{\psi^n(k,j,i-1)-\psi^{n-1}(k,j,i-1)}{\Delta t} \\ &\cdot \frac{\psi^{n-1}(k,j,i-1)-\psi^{n-1}(k,j,i-2)}{\Delta\dot{x}^1(i-1.5)} \cdot \frac{1}{F_2^{n-1}(k,j,i-1)} \end{aligned} \qquad \text{(B.57)}$$

$F_2^{n-1}(k,j,i-1)$ is calculated from:

$$\begin{aligned} F_2^{n-1}(k,j,i-1) = &\left(\frac{\psi^{n-1}(k,j,i-0.5)-\psi^{n-1}(k,j,i-1.5)}{\Delta\dot{x}^1(i-1.5)}\right)^2 \\ &+\left(\frac{\psi^{n-1}(k,j+0.5,i-1)-\psi^{n-1}(k,j-0.5,i-1)}{\Delta\dot{x}^2(j)}\right)^2 \\ &+\left(\frac{\psi^{n-1}(k+0.5,j,i-1)-\psi^{n-1}(k-0.5,j,i-1)}{\Delta\dot{x}^3(k,j,i-1)}\right)^2 \end{aligned} \qquad \text{(B.58)}$$

The grid sizes are calculated in the model by: $\Delta\dot{x}^1(i-1.5) = A(i-1.5)$, $\Delta\dot{x}^2(j) = B(j)$, $\Delta\dot{x}^3(k,j,i-1) = C(k)\cdot G(j,i-1)$.

The components c_2 and c_3 of the phase velocity vector are derived correspondingly. Following and extending the limitations given by Orlanski (1976) the phase velocity at the eastern boundary has to be restricted in the following way:

$$c_1^n(k,j,i) = \begin{cases} 0 & c_1^n(k,j,i) < 0 \\ c_1^n(k,j,i) & \text{for} \quad 0 \le c_1^n(k,j,i) \le \Delta\dot{x}^1/\Delta t \\ \Delta\dot{x}^1/\Delta t & \Delta\dot{x}^1/\Delta t \le c_1^n(k,j,i) \end{cases} \qquad \text{(B.59)}$$

With the assumption that the preliminary values $\hat{u},\hat{v},\hat{w}$ are equal to the final values $\bar{u},\bar{v},\bar{w}$ the pressure gradients normal to the boundary are equal to zero.

NUVWX1,2(1,2)=15, At Inflow Boundary: Large-Scale Values Prescribed; At Outflow Boundaries: Zero Gradient

This boundary condition can not be used when calculating the pressure p_2

$$
\begin{array}{lll}
\bar{u}(k,j,NX1) < 0 : & \bar{u}(k,j,NX1) & = U_g(k,j,NX1) \\
& \bar{v}(k,j,NX1P1) & = V_g(k,j,NX1P1) + V_g(k,j,NX1) \\
& & \quad - \bar{v}(k,j,NX1) \\
& \bar{w}(k,j,NX1P1) & = W_o(k,j,NX1P1) + W_o(k,j,NX1) \\
& & \quad - \bar{w}(k,j,NX1)
\end{array}
\qquad \text{(B.60)}
$$

$$
\begin{array}{lll}
0 \le \bar{u}(k,j,NX1) : & \bar{u}(k,j,NX1) & = \bar{u}(k,j,NX1M1) \\
& \bar{v}(k,j,NX1P1) & = \bar{v}(k,j,NX1) \\
& \bar{w}(k,j,NX1P1) & = \bar{w}(k,j,NX1)
\end{array}
$$

NUVWX1,2(1,2)=25, Boundary Normal Wind Components: Radiation Boundary Conditions; Boundary Parallel Wind Components: Zero Gradient

This Boundary condition can be used in connection with boundary condition NP2X1,2(1,2) = 1.

For the boundary normal wind components equations (B.10) to (B.59) are used. The boundary parallel wind components are calculated from:

$$
\begin{aligned}
\bar{v}(k,j,NX1P1) &= \bar{v}(k,j,NX1) \\
\bar{w}(k,j,NX1P1) &= \bar{w}(k,j,NX1)
\end{aligned}
\qquad \text{(B.61)}
$$

NUVWX1,2(1,2)=27, Boundary Normal Wind Components: Direct Calculation as Far as Possible; Boundary Parallel Wind Components: Zero Gradient

This Boundary condition can be used in connection with boundary condition NP2X1,2(1,2) = 1.

The equations for the boundary normal velocity components are discretized following Appendix B.1. This results in zero pressure gradients. The boundary normal advection at the inflow boundary is calculated by use of the phase velocity c_1 (equations (B.56) to (B.59)). At the outflow boundary a constant advection is assumed. The boundary normal diffusion is neglected.

The boundary parallel wind components are calculated following equation (B.61).

B.2.3.2 Prognostic Scalar Quantities

NPHI1,2(1,2)=0, Cyclic Boundary Conditions

This boundary condition has to be used at two corresponding lateral boundaries, e.g. at the east and west boundary.

$$
\begin{aligned}
\tilde{\chi}(k,j,0) &= \tilde{\chi}(k,j,NX1) + \chi_0(k,j,NX1) - \chi_0(k,j,0) \\
\tilde{\chi}(k,j,NX1P1) &= \tilde{\chi}(k,j,1) + \chi_0(k,j,1) - \chi_0(k,j,NX1P1)
\end{aligned}
\qquad \text{(B.62)}
$$

NPHI1,2(1,2)=1, Zero Gradient

$$\tilde{\chi}(k,j,NX1P1) = \tilde{\chi}(k,j,NX1) + \chi_0(k,j,NX1) - \chi_0(k,j,NX1P1) \tag{B.63}$$

This boundary condition results in zero fluxes at the lateral boundary.

NPHI1,2(1,2)=2, Gradient at the Boundary Equal to Gradient in the Model

$$\begin{aligned}\tilde{\chi}(k,j,NX1P1) &= 2\cdot\left(\tilde{\chi}(k,j,NX1) + \chi_0(k,j,NX1)\right)\\ &- \tilde{\chi}(k,j,NX1M1) - \chi_0(k,j,NX1M1)\\ &- \chi_0(k,j,NX1P1)\end{aligned} \tag{B.64}$$

NPHI1,2(1,2)=3, Fixed Values

To keep the value at the lateral boundaries of the model constant in time the values at the “old" time step have to be used:

$$\begin{aligned}\tilde{\chi}^n(k,j,\text{east boundary}) = 0.5\cdot\Big(&\tilde{\chi}^n(k,j,NX1P1) + \chi_0{}^n(k,j,NX1P1)\\ &+ \tilde{\chi}^n(k,j,NX1) + \chi_0{}^n(k,j,NX1)\Big)\end{aligned} \tag{B.65}$$

By use of the old values at the boundary the new ones are calculated:

$$\begin{aligned}\tilde{\chi}^{n+1}(k,j,NX1P1) = 2\cdot\bar{\chi}^n(k,j,\text{east boundary}) &- \tilde{\chi}^{n+1}(k,j,NX1)\\ &- \chi_0{}^{n+1}(k,j,NX1) - \chi_0{}^{n+1}(k,j,NX1P1)\end{aligned} \tag{B.66}$$

NPHI1,2(1,2) = 15, At Inflow Boundary: Large-Scale Values Prescribed; At Outflow Boundary: Zero Gradient

$$\begin{aligned}\bar{u}(k,j,NX1) < 0 : 0.5\cdot(&\chi_o(k,j,NX1)\\ &+ \tilde{\chi}(k,j,NX_1)\\ &+ \chi_o(k,j,NX1P) + \tilde{\chi}(k,j,NX1P1))\\ &= 0.5\cdot(\chi_o(k,j,NX1) + \chi_o(k,j,NX1P1))\end{aligned} \tag{B.67}$$

$$\begin{aligned}&\hat{=}\ \tilde{\chi}(k,j,NX1P1) = -\tilde{\chi}(k,j,NX1)\\ 0 \le \bar{u}(k,j,NX1) : &\tilde{\chi}(k,j,NX1P1) = \tilde{\chi}(k,j,NX1) + \chi_o(k,j,NX1)\\ &- \chi_o(k,j,NX1P1)\\ 0 \le \bar{u}(k,j,NX1) : &\tilde{\chi}(k,j,NX1P1) = \tilde{\chi}(k,j,NX1) + \chi_o(k,j,NX1) - \chi_o(k,j,NX1P1)\end{aligned} \tag{B.68}$$

NPHI1,2(1,2) = 16, At Inflow Boundary: Time dependent Values Prescribed; At Outflow Boundary: Zero Gradient

For this boundary condition a presimulation is necessary to get the values for the species concentrations at the inflow boundary.

$\bar{u}(k,j,NX1) < 0$:

The time dependent values are prescribed at the furthest grid point, not at the boundary on $\tilde{\chi}(k,j,NX1P1)$. The large scale value $\chi_o(k,j,i)$ has to be zero at all grid points.

$$0 \le \bar{u}(k,j,NX1) : \tilde{\chi}(k,j,NX1P1) = \tilde{\chi}(k,j,NX1) + \chi_o(k,j,NX1)$$

$$- \chi_o(k,j,NX1P1)$$

List of Tables

List of Symbols

Symbols for the atmospheric models

A	transformation coefficient for grid increment in west-east direction
A_f	control value for diastrophism
A_0	Albedo
a	stationarity parameter
B	transformation coefficient for grid increment in south-north direction
C	transformation coefficient for vertical grid increments
C_j	pollutant concentration
C_{j^*}	scaling value of concentration
c_p	specific heat of dry air at constant pressure
c_v	specific heat of dry air at constant volume
D	transformation coefficient for terrain slope in west-east direction
E	transformation coefficient for terrain slope in north-south direction
$\vec{F}$	moleculare friction
F	transformation coefficient
f	Coriolis parameter ($2\Omega\sin\varphi$)
f'	Coriolis parameter ($2\Omega\cos\varphi$)
G	transformation coefficient
g	acceleration of gravity
$\dot{g}$	determinant $\lvert \dot{g}_{ij} \rvert$
$\dot{g}_{il}$	covariant metric tensor
$\dot{g}^{il}$	contravariant metric tensor

H_s characteristic vertical scale of a phenomen

h_θ depth of temperature wave

h topography height

$\vec{i}$ unit vector in west-east direction

$\vec{j}$ unit vector in south-north direction

K_{hor} horizontal exchange coefficient for momentum

$K_{hor,\chi}$ horizontal exchange coefficient for scalar quantities

K_{vert} vertical exchange coefficient for momentum

$K_{vert,\chi}$ vertical exchange coefficient for scalar quantities

$\vec{k}$ unit vector in vertical direction

k_s thermal diffusivity in soil

L Monin Obukhov length

L_S characteristical horizontal scale of a phenomen

l_b blending height

l_* scale of horizontal extension of sub-grid scale surface elements

l_{21} latent heat of vaporization of water

p pressure

p_0 large-scale pressure (basic state)

p_1 pressure deviation (“hydrostatic” pressure deviation)

p_2 pressure deviation ("dynamic" pressure deviation, corresponds to rest term in pressure needed to fulfil anelastic approximation)

$\tilde{p}$ pressure devitaion from basic state

$\overline{p}$ mean pressure value

p' pressure fluctuation

Q_χ sources and sinks in the balance equation of scalar quantities χ

$\vec{\dot{q}}_i$ covariant basis vectors in coordinate system $\dot{x}$

$\vec{\dot{q}}^i$ contravariant basis vectors in coordinate system $\dot{x}$

q_1^1 specific humidity

$q_{1^s}^1$ surface humidity

$q_{1^{sat}}^1$ saturation value of surface humidity

$q_{0_i}^1$ large scale part of $q_i^1 (i = 1,2,3)$

$\tilde{q}_i^{\,1}$ humidty deviation from basic state of $q_i^1 (i = 1,2,3)$

$\hat{q}_i^{\,1}$ ' preliminary' value of $q_i^1 (i = 1,2,3)$

q_1^2 liquid water content [kg] per kg humid air (dry air and water)

q_1^3 ice content [kg] per kg air (dry air and ice)

q_* scaling value for specific humidity

$q_{*,j}$ sub-grid scale scaling value for specific humidity

R universal gas constant

R_o gas constant of dry air

R_1^1 gas constant of water vapour

R_i^k individual gas constant

R_i^* modified Richardson number

$\vec{r}$ location vector

r relative humidity

T temperature

T_0 large-scale temperature (Basic state)

T_s surface temperature

t time

U_g geostrophic wind in west-east direction

u velocity in west-east-direction

$\hat{u}$ preliminary velocity in west-east direction

u' velocity fluctuation in west-east direction

u_i velocity components in Cartesian coordinates

$\overline{u}$ mean velocity in west-east direction

$\dot{u}_i$ covariant velocity component

$\dot{u}^i$ contravariant velocity component

$\overline{\dot{u}_i}$ mean contravariant velocity component

$\dot{u}^{i}{}'$ contravariant component of velocity fluctuation

u_* friction velocity

$u_{*,l}$ subgrid scale friction velocity

V magnitude of horizontal wind

$\vec{V}_g$ geostrophic wind vector

V_g geostrophic wind in south-north direction

V_{TR} terminal velocity of rain drops

$\vec{v}$ velocity vector

v	velocity in south-north direction
$\hat{v}$	temporal velocity in south-north direction
v_d	deposition velocity
$\overline{v}$	mean velocity in south-north direction
v^k	specific volume
W_s	bulk moisture content
W_k	saturated value of W_s
w	vertical velocity
$\hat{w}$	temporal vertical velocity
$\overline{w}$	mean vertical velocity
X	Cartesian coordinate system
$\dot{X}$	terrain-following coordinate system
x	horizontal coordinate in west-east direction in coordinate system X
$\dot{x}^i$	coordinate in coordinate system $\dot{X}$
y	horizontal coordinate in south-north direction in coordinate system X
$Z(t)$	zenith angle
$z_{jk=1}$	height of first grid level
z	vertical coordinate in coordinate system X
z_s	topographic height in coordinate system X
z_t	height of model top
z_0	mean roughness length
z_0^j	subgrid-scale roughness length
α	ratio of exchange coefficients for scalar quantities and momentum
α_d	wind direction

$\overset{*}{\alpha}$ grid volume

β function for calculating changes in specific humidity

$\dot{\Gamma}^{i}_{j,j}$ Christoffel symbol

γ temperature gradient

Δt time step

Δx longitudinal grid increment

$\Delta \dot{x}^1$ grid increment in west-east direction in coordinate system $\dot{X}$

$\Delta \dot{x}^2$ grid increment in south-north direction in coordinate system $\dot{X}$

$\Delta \dot{x}^3$ vertical grid increment in coordinate system $\dot{X}$

Δy lateral grid increment

Δz vertical grid increment

ν kinematic viscosity of air

ν_R damping coefficient

ν_s thermal conductivity

η vertical coordinate in coordinate system $\dot{X}$

θ potential temperature

θ_0 large-scale part of potential temperature

$\widetilde{\theta}$ meso-scale part of potential temperature

θ' potential temperature fluctuation

θ_* scaling value of temperature

θ^j_* subgrid-scale scaling value of temperarure

$\widetilde{\theta}_{Mean}$ area mean temperature values

$\hat{\theta}$ 'temporal' value of potential temperature

κ von Karman constant

ρ density of air

ρ_0 large-scale part of density

$\widetilde{\rho}$ meso-scale part of density

$\overline{\rho}$ mean density

ρ' density fluctuation

τ_{ij} component of turbulent stress tensor

Φ geopotential

ϕ geopotenital latitude

χ any scalar quantity

$\widetilde{\chi}$ meso-scale part of scalar quantity χ

$\overline{\chi}$ mean value of scalar quantity χ

$\hat{\chi}$ 'temporal' value of scalar quantity χ

χ' fluctuation of scalar quantity χ

χ_0 large-scale part of scalar quantity χ

ψ any quantity

$\widetilde{\psi}$ meso-scale part of ψ

$\overline{\psi}$ mean value of ψ

ψ' fluctuation of ψ

ψ_0 large-scale part of ψ

ψ_m stability function of momentum

ψ_h stability function of heat

$\vec{\Omega}$ angular velocity vector of the earth

Ω magnitude of

Ω_i covariant component of earth's angular velocity vector

∇ gradient operator

$\Box x$ area size in west-east direction

$\Box y$ area size in south-north direction

Symbols for the sea ice model MESIM

A	Total ice concentration (percentage of coverage) of a grid cell
A_c	Ice concentration (percentage of coverage) of ice class c in a grid cell
A_w	Fraction of water in a grid cell
C	Cloud cover fraction
C^*	Strength reduction constant for lead opening (C^*=20)
$C_{h,w}$	Transfer coefficient for sensible heat from the ocean ($C_{h,w}$ =6·10^{-3})
c_p	Specific heat capacity of air at constant pressure (c_p =1006 J kg^{-1} K^{-1})
$c_{p,w}$	specific heat capacity of sea water ($c_{p,w}$ = 3980 J kg^{-1} K^{-1})
$c_{sd,oc}$	Surface drag coefficient between ice and ocean ($c_{sd,oc}$ = 4·10^{-3})
e	Excentricity of the elliptic yield curve for ice failure (e =2)
e_{2m}	Water vapour pressure at 2 m height
f	Coriolis parameter
$\vec{F}_\sigma$	Forces due to internal stresses in the ice

g	Gravity constant
H_c	Summed up vertical thickness of all clouds in the air column
$h_{d,c}$	Height of draft of ice floes in ice class c
$h_{f,c}$	Height of freeboard of ice in class c
h_i	Mean ice thickness over all ice classes
$h_{i,c}$	Thickness of ice in class c
$h_{ni,c}$	Thickness of new ice grown in leads between ice of class c (after drift)
$h'_{ni,c}$	Thickness of homogenious new-ice layer in leads belonging to ice in class c
h_{oc}	Sea surface height
$h_{s,c}$	Thickness of snow on top of the ice in class c
i	Imaginary unit
I_0	Short wave radiation entering the top layer of ice
i_0	Percentage of net short wave radiation at the ice surface that penetrates further into the ice
i_w	Percentage of net short wave radiation at the sea surface that penetrates further into the ocean
K_c	Extinction coefficient for short wave radiation in clouds (K_c =42 km^{-1})
K_i	Absorption coefficient of short wave radiation inside the ice (K_i =1.5 m^{-1})
k_i	Thermal conductivity of sea ice
$k_{i,f}$	Thermal conductivity of fresh ice ($k_{i,f}$ =2.035 W m^{-1} K^{-1})
k_s	Thermal conductivity of snow
l_{21}	Specific latent heat of vaporisation (l_{21}= $2.5 \cdot 10^6$ J kg^{-1})
$L_{fus,i}$	Volumetric heat of fusion for ice ($L_{fus,i}$ =$3.014 \cdot 10^8$ J m^{-3})
$L_{fus,s}$	Volumetric heat of fusion for snow ($L_{fus,s}$ =$1.097 \cdot 10^8$ J m^{-3})
$L_{i,c}$	Length of ice floes in class c
$L_{w.c}$	Spacing between ice floes (“length of water”) in class c

$LW_{\uparrow}$	Outgoing long wave radiation
$LW_{\downarrow}$	Incoming long wave radiation
LW_{net}	Net long wave radiation at surface
m_i	Mass of ice
P	Hydrostatic ice pressure
P^*	Compressive strength of compact ice of unit thickness (P^*=20 kN m^{-2})
P_p	Ice strength under ideal-plastic conditions
$q_{*,i}$	Scaling value for the specific humidity over ice
Q_c	Conductive heat flux from ice surface into the ice
$Q_{c,bot}$	Conductive heat flux at the bottom of the ice
Q_l	Latent heat flux at surface
Q_s	Sensible heat flux at surface
$Q_{s,bot}$	Sensible heat flux from the ocean to the ice base
$Q_{w,l}$	Total heat flux at the ocean surface
$Q'_{w,l}$	Remaining energy flux at sea surface after cooling of water
r_p	Regime function for the transition zone between viscous and plastic ice flow
$S_c(Z)$ / $S_c(z)$	Salinity of sea ice in relative depth Z or absolute depth z (ice class index omitted in the text)
$SW_{\downarrow}$	Incoming short wave radiation
SW_{net}	Net short wave radiation at surface
T_1	Temperature of ice or snow at the first level into the ice/snow
$T_{a,2m}$	Air temperature in 2 m height above ground
T_c	Temperature of the cloud base
$T_{i,bot}$	Temperature of the ice at the ice–water interface

$T_{i,c}(z)$	Temperature in z meter depth inside the ice of class c (abbreviated as "T_i")
T_f	Freezing point of sea water (T_f =271.35 K)
$T_{melt,I}$	Melting point of sea ice ($T_{melt,i}$ =273.05 K)
$T_{melt,s}$	Melting point of snow ($T_{melt,s}$ =273.15 K)
$T_{s,c}(z)$	Temperature inside the snow on top of ice in class c in z meter depth
T_{sur}	Surface temperature of ice or snow (or water)
T_w	Temperature of the oceanic cover layer
T_w^{n-1}	Water temperature at the previous time step
$T'_{w,I}$	Temporary water temperature
$u_{*,i}$	Friction velocity of surface-dragged ice respective to the atmosphere
$u_{*,oc}$	Friction velocity between ice and ocean
$u_{*,w}$	Friction velocity of water surfaces respective to the atmosphere
u_i	Ice drift speed in x-direction
u_j	Ice drift speed in y-direction
$\vec{v}_i$	Ice drift velocity (identical for all ice classes)
$\left\|\vec{v}_i^{ic=1}\right\|$	Drift speed of new ice relative to that of "old" ice
$\vec{v}_{oc}$	Velocity of the geostrophic ocean current
Z	Relative depth in the ice (0 at top; 1 at bottom)
$z_{0,bot}$	Roughness length at the ice base respective to sea water ($z_{0,bot}$ = 0.1 m)
$z_{0,oc}$	Roughness length of the water surfrace with respect to the ocean current ($z_{0,oc}$ = 0.1 mm)
$z_{0,w}$	Roughness length of water surfaces in respect to wind
α_i	Albedo of ice surfaces
α_s	Albedo of snow surfaces

α_w	Albedo of water surfaces
Δt	Length of time step
Δx	Drift distance of new ice in one timestep
ε_a	Emissivity of the atmosphere
ε_c	Emissivity of clouds (ε_c=1)
$\dot{\varepsilon}_{ij}$	Strain rate of ice deformation
ε_{sur}	Emissivity of the respective surface (ε_{sur} = 0.99 for snow, ε_{sur}=0.97 for ice and water
ζ	Bulk viscosity of ice deformation
η	Shear viscosity of ice deformation
θ	Incidence angle of sun light
$\theta_{*,i}$	Scaling temperature over ice
κ	von Karman constant (κ = 0.4)
ρ_0	Large scale densitiy of air
ρ_i	Density of sea ice (ρ_i=900 kg m^{-3}; sometimes also 910 kg m^{-3} is used.)
$\rho_i c_i$	Volumetric heat capacity of sea ice
$(\rho_i c_i)_f$	Volumetric heat capacity of fresh ice ($(\rho_i c_i)_f$ =1.884·10^6 J m^{-3} K^{-1})
ρ_s	Density of snow (ρ_s=330 kg m^{-3} or 450 kg m^{-3} if at melting point)
$\rho_s c_s$	Volumetric heat capacity of snow
ρ_w	Density of sea water (ρ_w=1026 kg m^{-3})
$\rho_w c_w$	Volumetric heat capacity of sea water ($\rho_w c_w$ = 4.19·10^6 J m^{-3} K^{-1})
σ	Stefan-Bolzmann constant (σ = 5.67·10^{-8} W m^{-2} K^{-4})

$\vec{\vec{\sigma}}$	Tensor of internal stresses in the ice due to floe interaction
σ_{ij}	Component of the tensor of internal stresses in the ice: Stress acting in j-direction on a plane perpendicular to the i-direction
$\vec{\tau}_a$	Atmospheric drag forces
$\vec{\tau}_{a,f}$	Form drag part of the atmospheric drag forces
$\vec{\tau}_{a,s}$	Surface drag part of the atmospheric drag forces
τ_c	Optical thickness of clouds
$\vec{\tau}_w$	Oceanic drag force
ϕ_{oc}	Deviation angle between geostrophic ocean current and oceanic drag force ($\phi_{oc} = 25°$)
$\psi_{m,w}$	Stability function for momentum over water surfaces
Ψ_s	Total shear deformation of ice

References

Arritt, R.W., Pielke, R.A., and Segal, M. (1988): Variations of sulfur dioxide deposition velocity resulting from terrain-forced mesoscale circulations. *Atmos. Environ.*, 22, 715-723. DOI: 10.1016/0004-6981(88)90009-1

Asai T. (1965): A Numerical Study of the Air-Mass Transformation over the Japan Sea in Winter. *Journal of the Meteorological Society of Japan.* 43. (1). 1-15.

Atwater, M.A. and Brown, P.S. (1974): Numerical calculation of the latitudinal variation of solar radiation for an atmosphere of varying opacity. *J. Appl. Meteor.*, 13. (2), 289-297.

Bakan, S. (1994): Eine einfache Strahlungsparametrisierung für ein mesoskaliges Modell. Report, Max-Planck-Institut für Meteorologie, Hamburg, Internal paper.

Birnbaum, G. (1998): Numerische Modellierung der Wechselwirkung zwischen Atmosphäre und Meereis in derarktischen Eisrandzone. Berichte zur Polarforschung, 268, pp 160. Dissertation at University of Bremen,1997.

Bond, T.C., Streets D.G., Yarber K.F., Nelson S.M., Woo J.-H. and Klimont Z. (2004) : A technology-based global inventory of black and organic carbon emissions from combustion. *Journal of Geophysical Research*, Vol. 109, D14203

Bougeault, P. (1983): A non-reflective upper boundary condition for limited-height hydrostatic models. *Mon. Wea. Rev.*, 111, 420-429, DOI: 10.1029/2003JD003697

Briscolini, M., and Santangelo, P. (1989): Development of the mask method for incompressible unsteady glows, *Journal of Computational Physics,* 84 (1), 57–75.

Brutsaert, W. (1975): The roughness length for water vapor, sensible heat and other scalars. *J. Atmos. Sci.*, 32, 2028-2031, DOI: 10.1175/1520-0469(1975)032<2029:TRLFWV>2.0.CO;2

Brutsaert, W. (1982): Evaporation into the Atmosphere. D. Reidel Publishing Company, Dordrecht.

Businger, J.A. (1982)::Equations and concepts. in: F.T.M. Nieuwstadt, H. van Dop (ed.): "Atmospheric turbulence and air pollution modelling", D. Reidl Publishing Company, Dordrecht.

Buykov, M.V. and Khvorostyanov, V, I. (1977): Formation and evolution of radiation fog and stratus clouds in the atmospheric boundary layer. IZV. Atm. Oz. Phys. (engl. ed.), 13, 251-260.

Chamberlain, A.C. (1975): The movement of particles in plant communities. In: Vegetation and Atmosphere (ed. by Monteith, J.L.), Vol. 1, pp. 155-203. Academic Press, London.

Chang, J.S., Brost, R.A., Isaksen, I.S.A., Madronich, S., Middleton, P., Stockwell, W.R. and Walcek, C.J. (1987): Three-dimensional Eulerian acid deposition model: physical concepts and formulation. *J. Geophys. Res.*, 92, 681-700. DOI: 10.1029/JD092iD12p14681

Clark, T.L. (1977): A small-scale dynamic model using a terrain following coordinate transformation. *J. Comput. Phys.*, 24, 186-215, DOI: 10.1016/0021-9991(77)90057-2

Clarke, R.H. (1970): Recommended methods for the treatment of the boundary layer in numerical models. *Australien Meteorol. Mag.*, 18, 51-71.

Claussen, M. (1991): Estimation of areally-averaged surface fluxes. *Boundary-Layer-Met.*, 54, 387-410, DOI: 10.1007/BF00118868

Davies, H.C. (1976): A lateral boundary formulation for multilevel prediction models. *J.Roy.Met.Soc., 102, 405-418,* DOI: 10.1002/qj.49710243210

Dierer, S.C. (2002): Untersuchung von groß- und mesoskaligen Einflüssen auf die Entwicklung polarer Mesozyklonen mit Hilfe des Modells METRAS. Berichte aus dem Zentrum für Meeres- und Klimaforschung, ZMK Universität Hamburg, Meteorologisches Institut, Vol. 35, pp. 106.

De Jong, B. (1973): Net radiation received by a horizontal surface at the earth. Delft University Press, 1973.

Deardorff, J.W. (1978): Efficient prediction of ground surface temperature and moisture, with inclusion of a layer of vegetation. J. Geophys. Res., **83**, 1889-1903.

Deardorff, J. W. (1980): Stratocumulus-capped mixed layers derived from a three-dimensional model. *Boundary-Layer Meteorology*. 18(4). 495-527. DOI: 10.1007/BF00119502.

Detering H.W. (1985): Mischungsweg und turbulenter Diffusionskoeffizient in atmosphärischen Strömungsmodellen. Berichte d. Inst. f. Met. u. Klimat. Uni. Hannover, Nr. 25.

Doms, G. and Herbert, F. (1985): Fluid- und Mikrodynamik in numerischen Modellen konvektiver Wolken. Berichte des Institutes für Meteorologie und Geophysik, Universität Frankfurt/Main, Nr.62.

Dunst, M. (1980): Ergebnisse von Modellrechnungen zur Ausbreitung von Stoffbeimengungen in der planetarischen Grenzschicht. Zeitschrift f. Meteorologie, 30, 47-59.

Dunst, M. (1982): On the vertical structure of the eddy diffusion coefficient in the PBL, *Atm. Envir.*, 16, 2071-2074, DOI: 10.1016/0004-6981(82)90278-5

Dunst, M. and Rhodin, A. (1990): On the influence of frictional effects on surface fronts: *Beitr. Physik Atm.*, 63, 223-242.

Durran, D.R. (1981): The effects of moisture on mountain lee waves. NCAR-CT-65. Massachusetts Inst. of Technology and NCAR. cooperative Thesis Nr.65, pp 142.

Dutton, J.A. (1976): The Ceaseless Wind. Mc Graw Hill, New York.

Dyer, A. J. (1974): A review of flux-profile relationship. *Bound. Lay. Met.*, 7, 362-372, DOI: 10.1007/BF00240838

Ebert, E.E., and Curry, J.A. (1993): An intermediate one-dimensional thermodynamic sea ice model for investigating ice-atmophere interactions, *J. Geophys. Res.*, 98(C6); 10085-10109.

Eiken, H. (1992): Salinity Profiles of Antarctic Sea Ice: Field Data and Model Results. *J. Geophys. Res.*, AGU, 97, 15545-15557.

El Kasmi, A. and Christian M. (2008): An Extended K–ε Model for Turbulent Flow through Horizontal-Axis Wind Turbines, *Journal of Wind Engineering and Industrial Aerodynamics*, 96, 103–22.

Emde von der, K. (1992): Solving conservation laws with parabolic and cubic splines. *Monthly Weather Review*, 120(3), 482-492.
DOI: 10.1175/1520-0493(1992)120<0482:SCLWPA>2.0.CO;2

Etling, D. (1987): The planetary boundary layer PBL. Landlot-Börnstein, Group V, Volume, 4, Meteorology, Subvolume c1, Climatology, part 1, 151-188.

Fischer, H. (1995): Vergleichende Untersuchungen eines optimierten dynamischen-themodynamischen Meereismodells mit Beobachtungen im Weddellmeer, Berichte zur Polarforschung, 166, Alfred Wegener Institut, Bremerhaven

Fock, B.H. (2007): METRAS als Grobstruktursimulationsmodell. Diplomarbeit, Universität Hamburg, 89 pp,http://www.mi.uni-hamburg.de/fileadmin/files/Diplomarbeit_ Fock.pdf

Garrat, J.R. and Hicks, B.B. (1973): Momentum, heat and water vapour transfer to and from natural and artificial surfaces. *Q. J. Roy. Met. Soc.*, 99,680-687, DOI: 10.1002/qj.49709942209

Golchert, H.J. (1981): Mittlere monatliche Globalstrahlungsverteilungen in der Bundesrepublik Deutschland. Meteorol. Rdsch., 34, 143-151.

Groß, G. (1984): Eine Erklärung des Phänomens Maloja-Schlange mittels numerischer Simulation. Dissertation, Fachbereich Mechanik der Technischen Hochschule Darmstadt.

Haltiner, G.J. and Williams, R.T. (1980): Numerical prediction and dynamic meteorology. 2nd ed. Wiley, New York. 477 pp.

Harder, M. (1996): Dynamik, Rauhigkeit und Alter des Meereises in der Arktis – Numerische Untersuchungen mit einem großskaligen.Modell. Techn. Ber. 203, Alfred-Wegener-Institut, Bremerhaven, Berichte zur Polarforschung, pp. 996.

Herbert, F. and Kramm, G. (1985): Trockene Deposition reaktionsträger Substanzen, beschrieben mit einem diagnostischen Modell der bodennahen Luftschicht. Published in: Beder, K.H. and G. Löbel (Eds): Atmosphärische Spurenstoffe und ihr physikalisch-chemisches Verhalten. Springer Verlag, Berlin, 264 pp.

Herrmann, K. (1994): Zum Gültigkeitsbereich des Konzepts der Blendhöhe in einem mesoskaligen Modell - Ein Beitrag zur Parametrisierung bodennaher subskaliger Flüsse. Diplomarbeit, Universität Hamburg, pp 99.

Hibler, W. (1979): A dynamic thermodynamic sea ice model. Journal of Physical Oceanography, 9(4), 815-846.
DOI: 10.1175/1520-0485(1979)009<0815:ADTSIM>2.0.CO;2

Hicks, B.B. (1985) : Application of forest--atmosphere turbulent exchange information. In: Hutchison, B.A.Q., Hicks, B.B. (eds.): The forest atmosphere interaction. pp. 631-644.

Holtslag, A.A.M. and Moeng, C.H. (1991): Eddy Diffusivity and Countergradient Transport in the Convective Atmospheric Boundary Layer, *J. Atmos. Sci.* **48**, pp. 1690-1698, DOI: 10.1175/1520-0469(1991)048<1690:EDACTI>2.0.CO;2

Iqbal, M. (1983): An introduction to solar radiation. Academic Press, Toronto, pp 390.

Josberger, E.G. (1987): Bottom ablation and heat transfer coefficients from the 1983 marginal ice zone experiments. *J. Geophys. Res.*, 92(C7), 7012-7016.

Källberg P. (1977): Test of a lateral boundary relaxation scheme in a barotropic model. *ECMWF, Research Department, Internal Report, Bracknell, 3.*

Kanda, M., Kanega, M., Kawai, T., Moriwaki, R. and Sugawara, H. (2007): Roughness Lengths for Momentum and Heat Derived from Outdoor Urban Scale Models. *J. Appl. Meteorol. Clim.*, 46, 1067-1079, DOI: 10.1175/JAM2500.1

Kapitza, H. (1987): Das dynamische Gerüst eines nicht-hydrostatischen-Mesoskalen Modells der atmosphärischen Zirkulation. Dissertation, Fachbereich Geowissenschaften Universität Hamburg.

Kapitza, H., and Eppel, D. (1987): A 3-D. Poisson solver based on conjugate gradients compared to standard iterative methods and its performance on vector computers. *J. Comp. Phys.*, 68, 474-484, DOI: 10.1016/0021-9991(87)90067-2

Katul, G. (1998): An Investigation of Higher-Order Closure Models for a Forested Canopy, *Boundary-Layer Meteorology*, 89 (1), 47–74**.**

Kessler, E. (1969): On the distribution and continuity of water substance in atmospheric circulations. Meteor. Monogr., No. 32, Amer. Meteor. Soc., Boston, doi: 10.1016/0169-8095(94)00090-Z

Klemp, J.B. and Durran, D.R (1983): An upper boundary condition permitting internal gravity wave radiation in numerical mesoscale models, *Mon. Wea. Rev.* 111, 430-444.

Knoth, O. and Wolke, R. (1993): A comparison of fast chemical kinetic solvers in a simple vertical diffusion model, Internal paper, Institut für Troposphärenforschung, pp. 8.

Köhler, A. (1994): Parameterisierung der Wolkenmikrophysik und der Strahlung in einem mesoskaligen Transport- und Strömungsmodell. Diplomarbeit am Fachbereich Geowissenschaften der Universität Hamburg, pp 96

Lehmann R. (1993): On the choice of relaxation coefficients for Davies' lateral boundary scheme for regional weather prediction models. *Meteorol. Atmos. Phys.,* 52, 1-14, DOI: 10.1007/BF01025749

Linde, M. (2011): Modellierung des Einflusses von Windkraftanlagen auf das umgebende Windfeld. *Master Thesis, University of Hamburg*, Hamburg, Germany**.**

Liu, J., Chen, J.M., Black, T.A. and Novak, M.D. (1996): E-ε Modelling of Turbulent Air Flow Downwind of a Model Forest Edge, Boundary-Layer Meteorology, 77, 21–44.

Lüpkes, C. (1991): Untersuchung zur Parametrisierung der Koagulation niederschlagsbildender Tropfen. Verlag Dr. Kovacs, Hamburg, 156p.

Lüpkes, C. and Schlünzen, K.H. (1996): Modelling the arctic convective boundaryayer with different turbulence parameterizations, *Bound. Lay. Met.*, pp 107-130, DOI: 10.1007/BF00120077

Lurman, F. W., Lloyd, A. C.and Atkinson, R. (1986): A chemical mechanism for use in long range transport/acid deposition computer modeling, *J. Geophys. Res.* 91 D, 10905-10936.

Luthardt, H. (1987): Analyse der wassernahen Druck- und Windfelder über der Nordsee aus Routinebeobachtungen. Hamburger Geophysikalische Einzelschriften, Reihe A, Heft 83, pp 109.

Marshall, G.S. and Palmer, W.M.K. (1948): The distribution of raindrops with size. *J. Meteorol.*, 5, 165-166,
DOI: 10.1175/1520-0469(1948)005<0165:TDORWS>2.0.CO;2

Martin, A. (1984): Estimated washout coefficients for sulphur dioxide, nitric oxide, nitrogen oxide and ozone. *Atmos. Environ*., 18 , 1955-1961.

Martin, C.L. and Pielke, R.A. (1983): The adequacy of the hydrostatic assumption in sea breeze modeling over flat terrain. *Atm. Sci*., 40, 1472-1481.

Maykut, G., and Perovich, D. (1987): The role of shortwave radiation in the summer decay of a sea ice cover, *Journal of Geophysical Research*, AGU, 92, 7032-7044.

Maykut, G., and Untersteiner, N. (1971): Some results from a time-dependent thermodynamic model of sea ice, *Journal of Geophysical Research*, American Geophysical Union, 76, 1550-1575, DOI: 10.1029/JC076i006p01550

Mesinger, F., and Arakawa, A., (1976): Numerical methods used in atmospheric models", *Garp Publications Series*, No. 17, Volume I

Mikkelsen, R. (2003): Actuator Disc Methods Applied to Wind Turbines*, PhD Thesis, Technical University of Denmark*, Copenhagen, Denmark**.**

Mittal, R. and Iaccarino, G. (2005): Immersed Boundary Methods, *Annu. Rev. Fluid Mech*., 37, 239–61, 2005.

Molly, Jens-Peter (1978): Windenergie in Theorie und Praxis: Grundlagen und Einsatz, Müller.

Niemeier, U. (1992): Numerische Simulation von Strömungsfeldern im Bereich der Insel Helgoland, Diplomarbeit, Universität Hamburg, pp 84

Niemeier, U. (1992): Simulation von Strömungsfeldern im Bereich der Insel Helgoland. *Annalen d. Meteorologie*, NF27, 349-350

Niemeier, U. (1997): Modellierung chemischer Umsetzungen in einem hochauflösenden mesoskaligen Modell - Bestimmung realitätsnaher Randwerte. Berichte aus dem Zentrum für Meeres- und Klimaforschung, Universität Hamburg, 28, pp161.

Orlanski, I. (1976): A simple boundary condition for unbounded hyperbolic flows. *J. Comp. Phys.*, 21, 251-269, DOI: 10.1016/0021-9991(76)90023-1

Pahl, S. (1990): Parameterisierung der trockenen Deposition in einem mesoskaligen Transport- und Strömungsmodell. Diplomarbeit, Meteorologisches Institut der Universität Hamburg, pp 98

Pahl, S. and Schlünzen, K.H. (1990): Parameterisierung der trockenen Deposition in einem mesoskaligen Transport- und Strömungsmodell. Bayerisches Landwirtschaftliches Jahrbuch

Perkey D.J. and Kreitzberg C.W. (1976): A time-dependent lateral boundary scheme for limited-area primitive equation model. *Mon. Wea. Rev.,* 104, 744-755.

Pielke R.A. (1984): Mesoscale meterorological modelling. Academic Press, New York, pp 612.

Press, W.H., Flannery, B.P., Teukolsky, S. and Vetterling W.T. (1989): Numerical recipies in C. Cambridge University Press, Cambridge, New York, pp104-106, DOI: 10.1017/S0033583500004285

Raymond, W.H., and Kuo, H.L. (1984): A radiation boundary condition for multi-dimensional flows. *Quart. J. Roy. Met. Soc.*, 110, 535-551, DOI: 10.1002/qj.49711046414

Ries H., Schlünzen K.H., Brümmer B., Claussen M. and Müller G. (2010): Impact of surface parameter uncertainties on the development of a trough in the Fram Strait region. *Tellus A*, DOI: 10.1111/j.1600-0870.2010.00451.x

Roache, P.J. (1982): Computational Fluid Dynamics. Hermosa Publishers, Albuquerque.

Rotta, J.C. (1972): Turbulente Strömungen. B.G. Teubner, Stuttgart.

Salim, M. H., Schlünzen, K. H., and Grawe, D. (2015): Including Trees in the Numerical Simulations of the Wind Flow in Urban Areas: Should We Care? *Journal of Wind Engineering and Industrial Aerodynamics*, 144, 84–95**.**

Salzen von, K., Claussen, M. and Schlünzen, K.H. (1996): Application of the concept of blending height to the calculation of surface fluxes in a mesoscale model, *Meteorol. Zeitschrift*, Vol. 5, pp. 60--66

Sandnes, H. and Styve, H. (1993): Calculated budgets for airborne acidifying components in Europe, 1985, 1987, 1988, 1989, 1990 and 1991, EMEP / MSC-W Report 1/92, pp. 50.

Schlünzen, H., and Schatzmann, M. (1984): Atmosphärische Mesoscale-Modelle - ein Überblick. Hamb. Geophys. Einzelschriften, Reihe B, Heft 3.

Schlünzen, K.H. (1988): Das mesoskalige Transport- und Strömungsmodell 'METRAS' - Grundlagen, Validierung, Anwendung -. Hamb. Geophys. Einzelschriften, A 88, pp 139.

Schlünzen, K.H. (1989a): Die Inlandverlagerung einer Seewindfront an einem tidebeeinflußten Küstenstreifen. *Ann. Meteor.*, nf 26,p235-236.

Schlünzen, K.H. (1990): Numerical studies on the inland penetration of sea breeze fronts at a coastline with tidally flooded mudflats. *Beitr. Physik Atm.*, 63, 243-256

Schlünzen, K.H. (1992): Modellierung des Strömungsfeldes über Norddeutschland für den 23. Mai 1989. *Annalen d. Meteorologie*, NF27, 308-309.

Schlünzen, K.H., Pahl, S. (1992): Modification of dry deposition in a developing sea-breeze circulation - a numerical study. *Atmosph. Envir.*, 26 A, 51-61, DOI: 10.1016/0960-1686(92)90260-R

Schlünzen K.H., Leitl B., Lunkeit F. (2010): Meteorological Modelling (MOD). Vorlesungsskript, Version 1.0, Masterstudiengang Meterologie, University of Hamburg, pp 161.

Schlünzen, K.H., Boettcher, M., Fock, B.H., Gierisch A., Grawe D., Salim M. (2018): Technical Documentation of the Multiscale Model System M-SYS (METRAS, MITRAS, MECTM, MICTM, MESIM) Meteorologisches Institut, Universität Hamburg, MeMi Technical Report, 3, pp. 130.

Schlünzen, K. H., Flagg, D. D., Fock, B. H. Gierisch, A., Lüpkes, C., Reinhardt, V., and Spensberger, C. (2012): Scientific Documentation of the Multiscale Model System M-SYS (METRAS, MITRAS, MECTM, MICTM, MESIM, MEMI), Technical Report 4, Meteorologisches Institut, KlimaCampus Universität Hamburg, 140 P., https://www.mi.uni-hamburg.de/en/arbeitsgruppen/memi/modelle/dokumentation.

Schlünzen K.H., Grawe D., Bohnenstengel S.I., Schlüter I., Koppmann R. (2011): Joint Modelling of Obstacle Induced and Mesoscale Changes – Current Limits and Challenges. In review at INt. J. Wind Eng. Ind. Aerodynamics, DOI: 10.1016/j.jweia.2011.01.009

Schlüter, I. (2006): Simulation des Transports biogener Emissionen in und über einem Waldbestand mit einem mikroskaligen Modellsystem. *PhD Thesis, University of Hamburg, Hamburg, Germany*.

Schröder, F. (1987): Grundlagen des mesoskaligen Transport- und Strömungsmodells 'METRAS' - Thermodynamischer Modellteil und Schadstofftransportmodell -. Anlage zum 2. Zwischenbericht des Teilprojektes M4. Meteorologisches Institut, Universität Hamburg

Schröder, G. (2007): Development and test of a multiple grids option in a mesoscale model. Dissertation. Universität Hamburg. 166 p. URL: http://ediss.sub.uni-hamburg.de/volltexte/2008/3554/

Schumann, U. (1983): Stabilität und Genauigkeit des Leapfrog - und des Adams-Bashforth-Verfahrens und deren Varianten.MESOSCOP-Notiz Nr. 4/83. Institut für Physik d. Atmosphäre, DFVLR Oberpfaffenhofen IB/Nr. 553 83/12.

Schumann, U., and Volkert, H. (1984): Three-dimensional mass- and momentum-consistent Helmholtz-equation in terrain-following coordinates. aus "Efficient Solutions of Elliptic Systems", ed. W. Hackbusch. Vieweg & Sohn, Braunschweig.

Seinfeld, J. H. (1986): Atmospheric chemistry and physics of air pollution, John Wiley & Sons, New York, pp. 737.

Semtner, A.J., Jr. (1976): A model for the thermodynamic growth of sea ice in numerical investigations of climate. *J. Phys. Oceanography*, 6, 379-389.

Shapiro, C. (1971): The use of linear filtering as a parameterization of diffusion. J. Atm. Sci. 28, 523-531, DOI: 10.1175/1520-0469(1971)028<0523:TUOLFA>2.0.CO;2

Sheih, C.M., Wesely, M.L., and Hicks, B.B. (1979): Estimated dry deposition velocities of sulfur over the eastern United States and surrounding regions. *Atmos. Environ.*, 13, 1361-1368, DOI: 10.1016/0004-6981(79)90105-7

Shuman, F.G. (1960): Numerical experiments with the primitive equations. Proceedings of the International Symposium on Numerical Weather Prediction, Tokyo, p85, *Meteor. Soc. of Japan*, Tokyo.

Smolarkiewicz, P.K. (1983): A simple positive definite advection scheme with small implicit diffusion. *Mon. Wea. Rev.*, 111, 479-486, DOI: 10.1175/1520-0493(1983)111%3C0479:ASPDAS%3E2.0.CO;2

Smolarkiewicz, P.K. (1984): A fully multidimensional positive definite advection transport algorithm with small implicit diffusion. *J. Comp. Phys.*, 54, 325-362, DOI: 10.1016/0021-9991(84)90121-9

Smolarkiewicz, P.K., and Clark, T.L. (1986): The multidimensional positive definite advection transport algorithm: further development and applications. *J. Comp. Phys.*, 67, 396-438, DOI: 10.1016/0021-9991(86)90270-6

Spensberger, C. (2010): Albedoänderungen in der Arktis durch Rußemissionen von Schiffen und Flugzeugen. Diplomarbeit, Meteorologisches Institut, Universität Hamburg, p100.

Spiegel, M.R. (1982): Vektoranalysis: Theorie und Anwendung. Mc Graw-Hill Book Company GmbH, Hamburg.

Stephans, G.L., Ackerman, S., and Smith, E.A. (1984): A shortwave parametrization revised to improve cloud absorption. *J. Atm. Sci.*, 41, 687-690, DOI: 10.1175/1520-0469(1984)041%3C0687:ASPRTI%3E2.0.CO;2

Thehos, R. (1991): Numerische Simulation zum interregionalen Spurenstofftransport über Europa, Technische Hochschule Darmstadt, Fachbereich Mechanik, pp. 180.

Tiedtke, M., and Geleyn, J.F. (1975): The DWD general circulation model-description of its main feateres. *Beitr. Phys. Atmosph.*, 48, 255-277.

Tremblay, A. and Leighton, H. (1986): A three-dimensional cloud chemistry model. J. Clim. Appl. Met., 25, 652-671.
DOI: 10.1175/1520-0450(1986)025%3C0652:ATDCCM%3E2.0.CO;2

Troen, I.B. and Mahrt, L. (1986): A Simple Model of the Atmospheric Boundary Layer. Sensitivity to Surface Evaporation, *Boundary-Layer Meteorol.* **37**, pp. 129-148, DOI: 10.1007/BF00122760

Trozzi, C. and Vaccaro R. (1998): Methodologies for Estimating Air Pollutant Emissions from Ships, 22nd CIMAC International Congress on Combustion Engines, Copenhagen 18-21 may 1998.

Uphoff, M. (2008): Parameterisierung flugzeuginduzierter Vermischung in einem mesoskaligen Modell. Diplomarbeit, Meteorologisches Institut, Universität Hamburg.

Van der Vorst, H.A.(1992): Bi-CGSTAB: A Fast and Smoothly Converging Variant of Bi-CG for the Solution of Nonsymmetric Linear Systems, *SIAM J. Sci. and Stat. Comput.* 13, pp. 631-644. DOI: 10.1137/0913035

Voldner, E.C. and Barrie, L.A. and Sirois, A. (1986): A Literatur Review of Dry Deposition of Oxides of Sulphur and Nitrogen with Emphasis on Long--Range Transport Modelling in North America, *Atmos. Environ.*, 20, 2101-2123, DOI: 10.1016/0004-6981(86)90305-7

Walcek, C.J., Brost, R.A. and Chang, J.S. (1986): SO_2, sulfate and HNO_3 deposition velosities computed using regional landuse and meteorological data, *Atmos. Environ.*, 20, 949-964, DOI: 10.1016/0004-6981(86)90279-9

Wesely, M.L. and Hicks (1977): Some factors that affect the deposition rate of sulfur dioxide and similar gases on vegetation. *J. Air Pollut*., 27, 1110-1116.

Wilson, J. D. (1988): A second-order closure model for flow through vegetation." *Boundary-Layer Meteorology* 42: 371–92.

Wippermann, F.K. (1981): The applicability of several approximations in mesoscale modelling - a linear approach. *Beitr. Phys. Atmosph.*, 54, 298 - 308.

Wosik, G. and Schlünzen, K., H. (1996): GRIGAU -- Preprozessor zur Initialisierung idealisierter Topographien für das Modell METRAS. Meteorologisches Institut, Universität Hamburg, METRAS Techn. Rep., 4, pp20.

Wosik, G., Bigalke, K. and Schlünzen, K., H. (1994): GRITOP -- Preprozessor zur Initialisierung von Topographiedaten für das Modell METRAS. Meteorologisches Institut, Universität Hamburg, METRAS Techn. Rep., 3, pp24.

Wosik, G., Bigalke, K. and Schlünzen, K., H. (1994a): EMIINI -- Preprozessor zur Initialisierung von Emissionen für das Modell METRAS. Meteorologisches Institut, Universität Hamburg, METRAS Techn. Rep., 2, pp26.

Wrede, R.C. (1972) : Introduction to vector and tensor analysis. Dover Publications, New York.**Wu, J. (1980):** Wind-stress coeffcients over sea surfaces near neutral conditions - a revisit. J. Phys. Oceanogr. 10, 727-740.